CHALMERS
UNIVERSITY OF TECHNOLOGY

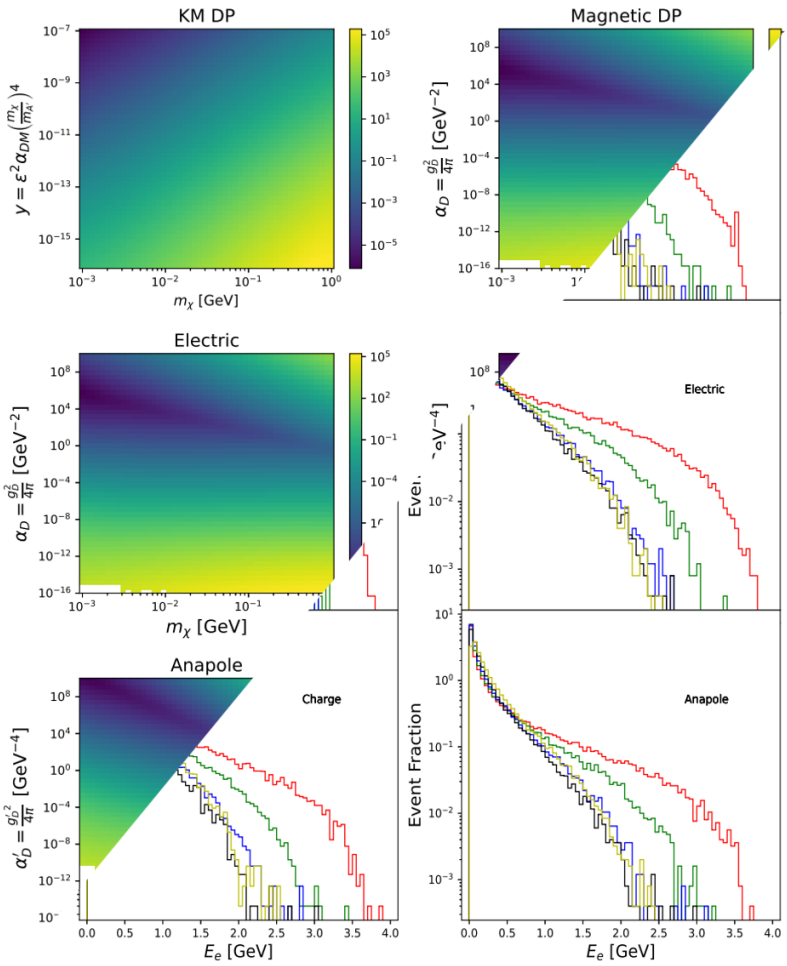

Dipole Dark Photon Emission at LDMX: Theory and Simulation

Master's thesis in Physics

THOMAS JERKVALL

DEPARTMENT OF PHYSICS

CHALMERS UNIVERSITY OF TECHNOLOGY
Gothenburg, Sweden 2024
www.chalmers.se

Master's thesis 2024

Dipole Dark Photon Emission at LDMX: Theory and Simulation

THOMAS JERKVALL

CHALMERS
UNIVERSITY OF TECHNOLOGY

Department of Physics
Division of Subatomic, High Energy and Plasma Physics
Chalmers University of Technology
Gothenburg, Sweden 2024

Dipole Dark Photon Emission at LDMX: Theory and Simulation
THOMAS JERKVALL

Supervisor: Riccardo Catena, Physics
Assistant Supervisor: Taylor Gray, Physics
Examiner: Riccardo Catena, Physics

Master's Thesis 2024
Department of Physics
Division of Subatomic, High Energy and Plasma Physics
Chalmers University of Technology
SE-412 96 Gothenburg
Telephone +46 (0)31 772 1000

Acknowledgements, dedications, and similar personal statements in this thesis, reflect the author's own views.

Cover: Split image of, in the top left, the relic density of dark matter for different interactions of the dark photon coupling to complex scalar dark matter and the Standard Model electron, and, in the bottom right, the simulated energy distributions of recoiling electrons in the creation of dark photons at the LDMX.

Typeset in LaTeX
Printed by Chalmers digitaltryck
Gothenburg, Sweden 2024

Dipole Dark Photon Emission at LDMX: Theory and Simulation
THOMAS JERKVALL
Department of Physics
Chalmers University of Technology

Abstract

The dark photon (DP) is a hypothetical massive mediator particle introduced to explain the present cosmological abundance of dark matter (DM) candidates that are lighter than nucleons, and that can thus be effectively searched for in fixed target experiments such as the Light Dark Matter eXperiment (LDMX). This thesis studies and compares higher order electromagnetic couplings between a DP, A', and the Standard Model (SM) electron. These couplings are expected to have interesting experimental signatures in missing energy and momentum experiments, but have so far only been explored within semi-analytical approaches that are not able to capture the full complexity of DP production at fixed target experiments. Motivated by this, simulations of the energy, E_e, and transverse momentum, p_T^e, distributions of a scattered electron in the production of a DP through a bremsstrahlung process have been performed by using the software MadGraph5 (MG5). These simulations have been made for the different electromagnetic interactions and a customary kinetic mixing (KM) coupling. The DP is added through a new gauge group, $U'(1)$, with mass in the range $m_{A'} = 0.1 - 1\,\text{GeV}$. The results of the different interactions and masses are then compared, and the LDMX potential for differentiating them is discussed. Further, the numerical simulations have been compared with results obtained through the Weizsäcker-Williams (WW) approximation, where agreement was found for the energy but not for the transverse momentum. The reason for this is believed to be that the nucleus p_T, which is neglected in this application of the WW approximation, is non-negligible. Finally, the parameter space of the different DP interactions is examined by calculating the relic abundance, Ωh^2, that can be produced for an example where the DP couples to complex scalar DM and the SM electron. This calculation has been performed using the program micrOMEGAs and validated with semi-analytical calculations.

Keywords: dark matter, dark photon, higher order electromagnetic couplings, LDMX, sub-GeV, astroparticle physics

Acknowledgements

I wish to express my sincerest gratitude to my supervisor Riccardo Catena, without whom this work would have never been possible. I would also like to thank my assistant supervisor Taylor Gray for always having an open door and being willing to discuss both technical issues and physics related ones. To the LDMX research group at Lund, thank you for enlightening discussions and an inviting atmosphere that gave me a fantastic insight of how a high-level research group functions. To the other Master's students at the Division of Subatomic, High Energy and Plasma Physics, that I have shared office space and studied with throughout this process, Gustav Strandlycke, Andreas Lund, Eli Ismailov, Elsa Danielsson, Oscar Muhr and Sixten Furenäs, thank you for the enjoyable conversations and for creating such a welcoming work environment. I want to also thank my family for their continued support throughout all of my studies.

Thomas Jerkvall, Gothenburg, June 2024

List of Acronyms

Below is the list of acronyms that have been used throughout this thesis listed in alphabetical order:

CM	Center-of-Mass
CMB	Cosmic Microwave Background
DM	Dark Matter
DP	Dark Photon
KM	Kinetic Mixing
LDMX	Light Dark Matter eXperiment
MACHO	Massive Astrophysical Compact Halo Object
MG5	MadGraph5
QED	Quantum Electro Dynamics
QFT	Quantum Field Theory
SM	Standard Model
WIMP	Weakly Interacting Massive Particle
WW	Weizsäcker-Williams

Contents

List of Acronyms **ix**

List of Figures **xiii**

List of Tables **xvii**

1 Introduction **1**
1.1 Evidence for Dark Matter . . . 2
1.2 Relic Abundance of Dark Matter . . . 4
1.2.1 Statistical Properties in an Expanding Universe . . . 4
1.2.2 Dark Matter Creation in the Early Universe . . . 6
1.3 Motivation for Sub-GeV Dark Matter Through a New Mediator . . . 7
1.4 Accelerator Searches for Dark Matter . . . 7
1.5 Simulation Software . . . 8

2 Theoretical Background **9**
2.1 The Interaction Lagrangian . . . 9
2.2 Production Processes of the Dark Photon at LDMX . . . 10
2.3 Matrix Elements for Annihilation of Scalar Dark Matter . . . 11
2.4 Relic Abundance from the Boltzmann Equation . . . 15
2.5 The Weizsäcker-Williams Approximation . . . 20

3 Cosmological Constraints **25**
3.1 Relic Density Simulation . . . 25
3.2 Crosscheck of the Simulation Results . . . 32

4 Higher Order Electromagnetic Moments in the LDMX Framework **37**
4.1 Energy and Transverse Momentum Distributions for Different Interactions and Masses . . . 38
4.2 Comparison to the Weizsäcker-Williams Approximation . . . 45

5 Discussion and Outlook for Future Work **51**
5.1 Discussion of the Results . . . 51
5.2 Outlook . . . 53

6 Conclusion **55**

Bibliography **57**

A Derivation of Feynman rules **I**
A.1 Feynman rules for scalar DM I
A.2 Feynman rules for the interaction Lagrangian II

B Derivation of Matrix Elements Assuming Complex Scalar DM **VII**
B.1 Kinetic Mixing VIII
B.2 Magnetic Dipole Moment IX
B.3 Electric Dipole Moment XI
B.4 Charge Moment XI
B.5 Anapole Moment XII

C Matrix Elements for the Decay of the Dark Photon **XIII**
C.1 $A' \to \chi + \chi^*$ XIII
C.2 $A' \to e^- + e^+$ XIV

List of Figures

2.1 Feynman diagrams of the bremsstrahlung process considered for the DP creation at the LDMX. 11

2.2 The s-channel process for complex scalar DM annihilation into SM electrons through a DP mediator. 11

2.3 Schematic picture of the annihilation process of DM into an electron and a positron shown in the CM frame of the interaction. 12

3.1 The line corresponding to the DM relic density of $\Omega h^2 = 0.12$, for the DP coupling to the electron and complex scalar DM. This has been plotted for masses $m_\chi = 1\,\text{MeV}$ to $m_\chi = 1\,\text{GeV}$ and coupling constants in the ranges $y = 10^{-16} - 10^{-7}$, $\alpha_D = 10^{-16} - 10^{10}\,\text{GeV}^{-2}$ and $\alpha'_D = 10^{-16} - 10^{10}\,\text{GeV}^{-4}$. The relation between the DM and the DP mass is $m_{A'} = 3m_\chi$. Also used is $\alpha_{DM} = 0.5$. 28

3.2 Zoomed in version of the line corresponding to the DM relic density of $\Omega h^2 = 0.12$, for the DP coupling to the electron and complex scalar DM, for all couplings but KM. This has been plotted for masses $m_\chi = 1\,\text{MeV}$ to $m_\chi = 1\,\text{GeV}$ and coupling constants in the ranges $\alpha_D = 10^{-9} - 1\,\text{GeV}^{-2}$ and $\alpha'_D = 10^{-9} - 1\,\text{GeV}^{-4}$. The relation between the DM and the DP mass is $m_{A'} = 3m_\chi$. Also used is $\alpha_{DM} = 0.5$. . . 29

3.3 The total relic density for all the possible combinations of coupling constants and masses in the regions $y = 10^{-16} - 10^{-7}$, $\alpha_D = 10^{-16} - 10^{10}\,\text{GeV}^{-2}$, $\alpha'_D = 10^{-16} - 10^{10}\,\text{GeV}^{-4}$ and $m_\chi = 1\,\text{MeV}$ to $m_\chi = 1\,\text{GeV}$. The plots are for the coupling of the DP to the electron and complex scalar DM. The relation between the DM and the DP mass is $m_{A'} = 3m_\chi$. Also used is $\alpha_{DM} = 0.5$. 30

3.4 The thermally averaged cross section times velocity, for a fixed freeze-out mass to temperature ratio of $x_f = \frac{m_\chi}{T_f} = 20$ for all the possible combinations of coupling constants and masses in the region $m_\chi = 1\,\text{MeV}$ to $m_\chi = 1\,\text{GeV}$ and $y = 10^{-16} - 10^{-7}$, $\alpha_D = 10^{-16} - 10^{10}\,\text{GeV}^{-2}$ and $\alpha'_D = 10^{-16} - 10^{10}\,\text{GeV}^{-4}$. The plots are for the coupling of the DP to the electron and complex scalar DM. The relation between the DM and the DP mass is $m_{A'} = 3m_\chi$. Also used is $\alpha_{DM} = 0.5$. 31

3.5 The thermally averaged cross section times velocity from following the theory in the paper by Gondolo and Gelmini [32], GG, for a fixed mass temperature ratio of $x = 20$. The mass and coupling constant ranges are the same as for the micrOMEGAs simulation in section 3.1. Also here the relation between the DM and DP mass is $m_{A'} = 3m_\chi$ and $\alpha_{DM} = 0.5$. 34

4.1 Energy distributions comparing the different interactions against each other for a fixed DP mass, $m_{A'} = 0.1, 0.3, 0.5, 0.7$ or 1 GeV, in each plot. The different interactions are KM, magnetic and electric dipole, charge and anapole. 40

4.2 Transverse momentum distributions comparing the different interactions against each other for a fixed DP mass, $m_{A'} = 0.1, 0.3, 0.5, 0.7$ or 1 GeV, in each plot. The different interactions are KM, magnetic and electric dipole, charge and anapole. 41

4.3 Energy distributions comparing different DP masses for each interaction, KM, magnetic or electric dipole, charge or anapole, separately. The different masses are $m_{A'} = 0.1, 0.3, 0.5, 0.7$ and 1 GeV. 42

4.4 Transverse momentum distributions comparing different DP masses for each interaction, KM, magnetic or electric dipole, charge or anapole, separately. The different masses are $m_{A'} = 0.1, 0.3, 0.5, 0.7$ and 1 GeV. 43

4.5 Ratio comparison of the energy distribution and transverse momentum of the scattering electron. Comparing KM interaction with $m_{A'} = 1$ GeV to magnetic dipole interaction with $m_{A'} = 0.7$ GeV. . . . 44

4.6 Ratio comparison of the energy distribution and transverse momentum of the scattering electron. Comparing charge interaction with $m_{A'} = 0.5$ GeV to anapole interaction with $m_{A'} = 0.5$ GeV. 44

4.7 Ratio comparison of the energy distribution and transverse momentum of the scattering electron. Comparing magnetic dipole interaction with $m_{A'} = 0.3$ GeV to charge interaction with $m_{A'} = 0.1$ GeV. . 45

4.8 The energy distribution of the recoiling electron in the WW approximation plotted against the MG5 simulations for the KM and magnetic dipole interactions and a DP mass of $m_{A'} = 0.1$ GeV. In the figure different maximum angles, θ_M, are shown. They are plotted in bins of 50 MeV from a cutoff at $E_e = 50$ MeV to a maximally possible $E_e = E_0 - m_{A'}$, i.e. a DP without any three-momentum. 48

4.9 The transverse momentum distribution of the recoiling electron in the WW approximation plotted against the MG5 simulation for the KM and magnetic dipole interactions and a DP mass of $m_{A'} = 0.1$ GeV. The transverse momentum is plotted in bins of 10 MeV for $p_T^e = 0 - 1.2$ GeV. 49

4.10 Energy and transverse momentum distributions of the final state nucleus for both KM and magnetic dipole interactions. The mass of the DP for these plots is $m_{A'} = 0.1$ GeV. 49

4.11 Energy and transverse momentum distributions for the DP for both KM and magnetic dipole interactions. The mass of the DP for these plots is $m_{A'} = 0.1\,\mathrm{GeV}$. 50

B.1 The s-channel process for complex scalar DM annihilation into SM electrons through a DP mediator. VII
B.2 Schematic picture of the annihilation process of DM into an electron and a positron shown in the CM frame of the interaction. IX

List of Tables

3.1 Comparison of $\frac{1}{2}\langle\sigma_{\chi+\bar{\chi}\to\psi+\bar{\psi}}v\rangle$ between the micrOMEGAs values, MO, and the method following Gondolo and Gelmini [32], GG, to cross-check. Values calculated with coupling constants $y = 10^{-15}$, $\alpha_D = 10^{-15}\,\mathrm{GeV}^{-2}$ and $\alpha'_D = 10^{-15}\,\mathrm{GeV}^{-4}$. 35
3.2 Comparison of $\frac{1}{2}\langle\sigma_{\chi+\bar{\chi}\to\psi+\bar{\psi}}v\rangle$ between the micrOMEGAs values, MO, and the method following Gondolo and Gelmini [32], GG, to cross-check. Values calculated with coupling constants $y = 10^{-11}$, $\alpha_D = 10^{-8}\,\mathrm{GeV}^{-2}$ and $\alpha'_D = 10^{-8}\,\mathrm{GeV}^{-4}$. 35
3.3 Comparison of $\frac{1}{2}\langle\sigma_{\chi+\bar{\chi}\to\psi+\bar{\psi}}v\rangle$ between the micrOMEGAs values, MO, and the method following Gondolo and Gelmini [32], GG, to cross-check. Values calculated with coupling constants $y = 10^{-8}$, $\alpha_D = 1\,\mathrm{GeV}^{-2}$ and $\alpha'_D = 1\,\mathrm{GeV}^{-4}$. 36

1

Introduction

In modern day cosmology dark matter (DM) in some form is a vital part of the model used to describe the universe [1]. This thesis will take the approach that DM is made of particles that extend the existing Standard Model (SM) of particle physics, which, in present day, is the model that has been the most successful in describing fundamental particles and forces. In particular, the focus of the thesis will be on sub-GeV DM, meaning DM with masses less than or equal to 1 GeV, that interact with the SM through a new mediator called the dark photon (DP). The DP is introduced via the addition of a new $U(1)$ gauge group, called $U'(1)$, where the DP, A', is the gauge boson related to this group. The DP is, as the SM photon, a spin-1 mediator, but unlike the regular photon the DP is massive. A natural way to introduce the coupling between the fermions of the SM and the DP is through what is called kinetic mixing (KM) [2–4] which generates a coupling that is very similar to that of the SM photon and the interaction, or Feynman rule, of the vertex is

$$\sim i\epsilon e Q_f \gamma^\mu, \tag{1.1}$$

where e is the quantum electrodynamics (QED) coupling constant (the elementary charge), Q_f is the charge of the fermion, γ^μ the Dirac gamma matrices and ϵ is called the KM parameter which effectively acts as a new coupling constant for the DP.

However, this is not the only way one can define the coupling between the DP and the fermions, another way is through higher order electromagnetic moments [4]. The comparison between the effects of these types of interactions, including the KM, is the main focus of this thesis. One of the goals of the thesis is to, through simulations, examine how differentiable the interactions, modeled through this DP, are in the framework of the electron accelerator fixed-target search for DM the Light Dark Matter eXperiment (LDMX). The simulations are also compared to the Weizsäcker-Williams approximation. Another goal is to show how one can study the model more thoroughly by putting bounds on the parameters, for an example case of complex scalar DM, through the calculation of the expected relic abundance, meaning the present day density of DM.

The layout of the thesis is as follows. First in this chapter, 1, an introduction to the subject is provided. It includes an overview of some evidence for DM and

motivation for the particle approach, a discussion about how to model the DM density observed in the universe today, arguments for studying sub-GeV DM as well as a brief introduction of accelerator experiments and in particular the LDMX which is the main focus. A description of the simulation softwares used is also given here. Next, in chapter 2 a theoretical background is provided. Here the model is presented in more detail through the Lagrangian describing the interactions between the SM fermions and the DP. The chapter also includes the matrix elements for the s-channel annihilation of assumed complex scalar DM into SM electrons, that have been calculated. The main production bremsstrahlung process that the DP would give rise to is also presented here. Further, a description of the theory that underlies the calculations of the present day density of DM, through the use of the Boltzmann equation is provided. The chapter then finishes by giving the necessary background for the theory of the WW approximation. Continuing, in chapter 3, the results of the DM relic density calculations are presented and the bounds of the parameters in the model are discussed. After this, in chapter 4, the simulated energy and transverse momentum distributions of the recoiling electron, in a LDMX like framework, are shown and compared for different interactions and masses of the DP. A comparison to the WW approximation is also presented, for two of the interactions and a DP mass of $m_{A'} = 0.1\,\text{GeV}$. Following, in chapter 5, a discussion of the results and an outlook for future work is given, and finally, in chapter 6 one finds a conclusion highlighting the key points that have been brought up.

Throughout this thesis natural units are used, which means setting $c = \hbar = 1$, and also $k_B = 1$. A consequence of this is that particle masses are given in terms of energy, often in the unit of GeV. Additionally, as commonly used in particle physics, the Minkowski metric used will be the one with mostly negative signature, $\eta_{\mu\nu} = \text{diag}(+1, -1, -1, -1)$.

1.1 Evidence for Dark Matter

In modern days one of the pressing issues that are yet to be explained is the nature of DM. The following background is not complete in the sense that it does not cover all the evidence and theories of DM, but aims to describe a couple of the major parts. Some of the most prominent, historical and current, implications and evidence for DM are related to Fritz Zwicky's work on masses of galaxy clusters, Vera Rubin's measurements on galactic rotation curves as well as measurements of the cosmic microwave background and gravitational lensing [1].

In the 1930s Zwicky used the virial theorem to approximate the masses of galaxy clusters [5]. He was from this able to estimate the velocity dispersion of the cluster. What he found was a dispersion of 80 km/s, while the measured value was closer to 1000 km/s. This huge discrepancy then implied the need for more mass than what was visible, i.e. DM. Later on during the 1970s Vera Rubin, Kent Ford and Norbert Thonnard, amongst others, measured galactic rotation curves of galaxies [6]. From these measurements it was possible to estimate the distribution of the contained mass [1]. What was found was that the rotation curves were approximately flat

[6], which led to the conclusion that there should be a much higher abundance of mass in the outer parts of the galaxies than previously predicted [1]. Further evidence for the existence of DM comes from measurements of the anisotropies in the cosmic microwave background (CMB), which is for example measured by the Planck collaboration to obtain the present day density of DM, $\Omega h^2 = 0.120 \pm 0.001$ [7]. The CMB is made up of photons remaining from the earliest stages of the Universe that have travelled up until now to reach us, and today the temperature of the CMB is measured to $T_0 = 2.72548 \pm 0.00057\,\mathrm{K}$ [8]. Also, gravitational lensing of galaxies and clusters is used to indicate DM which works by the fact that massive objects bend light due to their gravity, which is known from general relativity.

The theories of DM are many. One of these is that DM is made of new particles not included in the Standard Model of particle physics [1]. This is the approach that this thesis will take. Another theory is that DM would be made of baryonic/ordinary matter, but that is not luminous enough to be observed [1]. These objects are named massive astrophysical compact halo objects (MACHOs) and could be for example black holes, planets or different types of stars. However, with the help of gravitational lensing measurements the MACHOs were shown to not have a large enough density to account for all the mass in the galactic halo of the Milky Way [9, 10]. Also related to the density another limit placed on baryonic models is given by the fact that the total density of baryonic matter in the entire universe, as measured by the mentioned Planck collaboration examining the CMB anisotropies, $\Omega_b h^2 = 0.0224 \pm 0.0001$ [7], does not even constitute 20% of the matter content of the universe [1]. Another related theory is concerned with primordial black holes [11], i.e. black holes formed in the very early stages of the Universe. However, that these black holes could make up DM is not as probable since their assumed abundance is too small [1]. Another interesting theory is that of modified gravity [1]. This theory takes the approach that the current theories we have to describe the Universe are not adequate or at least need to be modified to describe gravity and interpret DM. However, it has had difficulties describing clusters of galaxies correctly.

The difficulties presented for the other possible theories motivate the particle approach to DM. But, returning to DM as viewed as fundamental particles there is, also here, a sea of models. Three examples are supersymmetric particles [12], axions [13] and weakly interacting massive particles (WIMPs) [14]. Supersymmetry is a theory that, by definition, relates the bosons and fermions via a spacetime symmetry. This model would require new particles that could theoretically be interpreted as DM. Axions on the other hand are necessary for one type of solution of the strong CP-problem in quantum chromodynamics. Finally, WIMPs are particles that have interaction strengths close to that of the electroweak forces and are also among the most searched for [1].

1.2 Relic Abundance of Dark Matter

The relic abundance, or relic density, $\Omega = \frac{\rho}{\rho_c}$, of DM is the density in our observable universe, that we can measure today, given as a ratio of the critical density, $\rho_c = \frac{3H^2}{8\pi G}$ [15]. This density is often given as Ωh^2 where h is the reduced Hubble parameter i.e. $h = H/100$. As mentioned in section 1.1 the measurement of Ωh^2 has been performed by the Planck collaboration by studying the anisotropies of the cosmic microwave background (CMB) and is, repeating the result here, $\Omega h^2 = 0.120 \pm 0.001$ [7]. For a DM candidate, imposing that the calculated relic density is equal to the observed value puts a cosmological constraint on the model of interest. This is because the particles of the model has to interact strongly or weakly enough be able to produce the correct amount of DM to be consistent with the CMB measurements. To describe the production of DM in the universe's beginning one has to consider the construction of the early universe, during which most SM particles were considered to be in thermal equilibrium [15]. Today DM, as we know it, is not in equilibrium and if it ever was is an unanswered question. In this section a description of the physics of the equilibrium will be given. After this methods for DM creation will be described focusing in particular on the freeze-out mechanism, which is the one considered in this thesis, but also another mechanism, freeze-in, is mentioned in passing.

1.2.1 Statistical Properties in an Expanding Universe

The expansion of the universe can be described by the scale factor $a(t)$ and the rate of the expansion is given by the Hubble parameter $H \equiv \frac{\dot{a}}{a}$, where the dot describes a time derivative [15]. However, in the derivations to follow the time coordinate will be described in terms of the temperature of the universe, meaning the temperature of the photons, T. Also for convenience, it is common to define the ratio between the temperature and the mass of a considered particle species, i, as

$$x_i \equiv \frac{m_i}{T}. \tag{1.2}$$

The temperature can be used as a unit of time since the universe is expanding and therefore also cooling. To describe the statistical properties of a particle species the phase-space distribution f can be used. This is, in general, a function of the four-momentum of the particles and spacetime, but in an isotropic and homogeneous Friedman-Robertson-Walker universe this only becomes a function of time and energy, E, or the three momentum $|\vec{p}|$ through the energy-momentum relation $E^2 = |\vec{p}|^2 + m^2$ [15]. The phase-space distributions further relate to the density of the number of particles of the species under consideration, by integrating it over all possible three momenta and scaling by the internal degree of freedom factor, the spin, of that species, g_i, [15]

$$n_i(t) = \int g_i f(E,t) \frac{d^3\vec{p}}{(2\pi)^3}. \tag{1.3}$$

The number density is important, but the density property of interest is the one

that expands together with the universe. This is called the yield, Y_i, and is given by the number density divided by the entropy density of the universe, $s \equiv \frac{S}{a^3}$, where S is the total entropy per comoving volume, [15]

$$Y_i \equiv \frac{n_i}{s}. \tag{1.4}$$

The total entropy of the comoving volume will be approximated to be conserved, i.e. constant, which makes it possible to see that Y_i is comoving. This is because a constant S implies that $Y \propto n_i a^3$ which would be the exact comoving number density. The present day yield for a species relates to the present day density through $\rho_0 = s_0 m_i Y_{i,0}$, where s_0 is the present day total entropy density of the universe [15]. Due to this relation it also relates to the abundance Ωh^2 through

$$\Omega h^2 = \frac{s_0 m_i Y_{i,0}}{\rho_c}. \tag{1.5}$$

As stated previously most particles were in thermal equilibrium at some point in the early universe. This implies both kinetic and chemical equilibrium and specifies the phase-space distribution which takes the following form [15]

$$f^{EQ} = \frac{1}{e^{(E-\mu)/T} \pm 1}, \tag{1.6}$$

where the $-$ gives the Bose-Einstein distribution, used for bosons, and $+$ the Fermi-Dirac distribution, used for fermions. The chemical potential μ will be approximated to 0, for all species considered, since $|\mu| \ll T$ [15]. Another assumption that will be made is that the species are described by Maxwell-Boltzmann statistics which only differs from the previous ones by setting the ± 1 to zero.

Furthermore, the Hubble parameter in the early Universe under the radiation dominated era can also be specified and is given by [15]

$$H = \sqrt{\frac{8\pi^3 g_{*,E}}{90}} \frac{T^2}{m_P}, \tag{1.7}$$

where m_P is the Planck mass and $g_{*,E}$ is a degree of freedom parameter that relates to the energy density for the particles in the equilibrium, which is approximately given by [15]

$$g_{*,E} = \sum_{\text{Bosons}} g_i \left(\frac{T_i}{T}\right)^4 + \frac{7}{8} \sum_{\text{Fermions}} g_i \left(\frac{T_i}{T}\right)^4 \tag{1.8}$$

where g_i is the internal degree of freedom for particle i and T_i is the temperature of that species. Further, it is also possible to specify the entropy through a similar degree of freedom factor. If one assumes that mostly relativistic particles contribute to the calculation of the entropy density the expression becomes [15]

$$s = \frac{2\pi^2}{45} h_{*,s} T^3, \tag{1.9}$$

where $h_{*,S}$ is, as $g_{*,E}$, a degree of freedom parameter and is approximately given by

$$h_{*,s} = \sum_{\text{Bosons}} g_i \left(\frac{T_i}{T}\right)^3 + \frac{7}{8} \sum_{\text{Fermions}} g_i \left(\frac{T_i}{T}\right)^3 \tag{1.10}$$

where g_i is the internal degree of freedom for particle i and T_i is the temperature of that species. As more and more particles decouple from the equilibrium these degrees of freedom will decrease as the particle content is reduced.

1.2.2 Dark Matter Creation in the Early Universe

There are different theories that describe the creation process of DM. As stated above, DM is today not in thermal equilibrium and to describe the statistical properties of a DM species the Boltzmann equation (1.11) needs to be used, which describes how the phase-space occupancy of a species, f, evolves [15].

$$L[f] = C[f] \tag{1.11}$$

This equation relates the Lioville operator, L, of the studied species to the collision operator, C, that takes the interactions, production and annihilation, between particles into account. To get the equation in terms of the number density, and in the end the yield, one has to integrate it over all three-momenta, which will be done in section 2.4. Even though DM is not in equilibrium today the answer to the question if DM was ever a part of the thermal equilibrium is different between different creation mechanisms. For freeze-out, which will be the main focus of the thesis, DM is considered to once have been a part of the thermal bath and then decoupled at a later time, corresponding to a lower temperature called the freeze-out temperature T_f [15], while for models such as freeze-in the DM is considered to never have been a part of the equilibrium [16].

Decoupling from the thermal equilibrium is not something unique to DM, this happens to SM particles as well. If this was not the case then there would barely be any particles left since they would decay exponentially with the temperature of the universe as, $\propto e^{-m/T}$, when the temperature reaches far below the mass [15]. The intuitive picture of freeze-out can be explained in a few steps [17]. First, to consider a particle to have been in thermal equilibrium in the early universe it must interact strongly enough with the particles in the equilibrium so that the interaction rate, Γ, becomes larger than the expansion rate of the universe, i.e. $\Gamma > H$. As then the universe expands and cools it eventually reaches a point when the temperature is so low that there is statistically not enough energy to produce the species from particles with lower mass. At this point the density of the species can only decrease, which it does exponentially. This continues until the interaction rate becomes low enough in comparison to the expansion rate, $\Gamma < H$, and around this point the species leaves the thermal bath and the comoving density, Y, becomes almost constant, since statistically they are then too far apart due to the universe expanding faster than they can interact. A more exact definition of what is considered the freeze-out temperature will be given when expanding on the Boltzmann equation in

section 2.4. An upper limit on the possible interaction strength to the equilibrium particles is then set by the fact that the species should not have annihilated away too much of its density before it decouples, since Γ is dependent on the strength of the interactions. As a side note, for the freeze-in case the particles would have a weak enough interaction to not thermalize and become part of the full equilibrium [16].

1.3 Motivation for Sub-GeV Dark Matter Through a New Mediator

Weakly interacting massive particles (WIMPs) have, as mentioned in chapter 1.1, been one of the leading theories for DM candidates. Nevertheless, these type of particles have limitations and if one considers them as interacting via the SM weak force then there is a lower bound set on the mass at $\gtrsim 2\,\mathrm{GeV}$, estimated by Lee and Weinberg [18]. Following, due to the fact that WIMPS have yet to be discovered, one possibility is that DM could have evaded the current searches by being to light. This combined with the fact that DM with mass below a few GeV has not been as probed by experiments [3], motivates the investigation for DM at masses below the Lee-Weinberg bound, i.e. sub-GeV DM. To be able to investigate DM at these mass ranges the model used then needs a mechanism that is different from the regular SM weak interaction. One possible way of doing this is by introducing another, beyond the SM, mediator which in this thesis will be the DP, A'.

1.4 Accelerator Searches for Dark Matter

The search for DM particles can be divided into different types of experiments some of which are [19]: direct detection, which aims at having DM particles interact with SM particles here on earth, indirect detection which tries to detect SM remnants of DM particles interacting with themselves, and collider searches where DM is created in a collision process between SM particles. As of now, no DM particles have been discovered, but each experiment that is running sets limits on the parameter space of many models.

The type of experiments of interest for this thesis is accelerator based ones and the main focus will be on the fixed target search the Light Dark Matter eXperiment (LDMX) [3]. There are of course other searches for DM which utilise particle accelerators, for example at the LHC. The goal of the LDMX is to search for DM in the sub-GeV mass range [3], which as described in section 1.3 is motivated by the lack of discovery in the heavier regions. LDMX is an accelerator experiment that in the first stage will be stationed at the National Accelerator Laboratory SLAC, and utilise a 4 GeV electron beam, from the accelerator LCLS-II [20]. The collision target is tungsten and the idea is to measure the energy and momenta of the recoiling electrons in an attempt to deduce if there has been any production of DM particles, or mediators, that have obtained parts of the energy and momenta of the

incoming electrons. A discovery could then be considered when the recoil electrons' properties deviate from the expected ones.

Some quantities that are relevant for accelerator experiments are the energy, E, and transverse momentum, p_T, distributions of the particles being detected. The transverse momentum is defined as the part of the total three-momentum, $\vec{p}$, that is orthogonal to the beam axis [21]. Since the beam axis is usually placed along the z-axis in calculations the amount of momentum following the beam axis is named p_z. The angle, θ, between the beam axis and the outgoing particle is often given in terms of the pseudorapidity $\eta \equiv \ln\left(\cot\frac{\theta}{2}\right)$.

1.5 Simulation Software

The main simulation software that has been used to examine the models in the LDMX framework is MadGraph5 (MG5) [22], which allows for the simulation of interactions in an artificial collider experiment given the definitions of the particles included and the Feynman rules of the vertices. To generate these the model Lagrangian, described in section 2.1, has been implemented through the Mathematica package FeynRules [23]. This is a tool that can calculate the quantum field theory (QFT) Feynman rules for the Lagrangian in question, and also allows for the implementation of the different particles that are relevant. To add the SM physics to the model a premade FeynRules SM file was used, which is found at [24]. The FeynRules output was then used to create model files of the UFO format that further was implemented in MG5. Another feature of FeynRules is that it can provide the decay rates for a particle in the model. Furthermore, to calculate the relic densities and other cosmological properties of the DM model the program micrOMEGAs [25] was used. However, the program version has been micrOMEGAs 5.2.13, since for the sub-GeV masses of interest there seems to, currently, be an apparent bug or flaw in the latest version, micrOMEGAs 6.0. To run micrOMEGAs one generates a CalcHEP [26] file structure for the model, which can be done from knowing the Lagrangian and again utilising FeynRules as for the UFO. Outside of working as model files to run in micrOMEGAs, CalcHEP is a tool that can also calculate the matrix elements squared of a given process of an implemented model. In this thesis, the relevant matrix element calculations have been made by hand to validate the results, due to the bug in micrOMEGAs 6.0. To crosscheck trace evaluations in matrix element calculations the Mathematica package FeynCalc [27, 28] was used.

2

Theoretical Background

In this chapter the studied model is described in more detail. First, the Feynman rules for the interaction vertex between the DP and the SM fermions is presented and from this a position space Lagrangian that generates the interactions is constructed. Following, the bremsstrahlung production process under consideration for the DP at the LDMX is discussed. After this, the matrix elements for the annihilation of DM into SM electrons, with the assumption of complex scalar DM, are calculated for KM and the electromagnetic interactions. Also the decay rates for the DP into SM electrons and DM is given. Furthermore, the theory of how to calculate the relic density, starting from the Boltzmann equation, for a given DM theory is discussed. Finally, the Weizsäcker-Williams approximation for the scattering process, in the case of the KM and magnetic dipole interactions, is presented.

2.1 The Interaction Lagrangian

The Feynman rules for the vertex between the DP, A', and the SM fermions, ψ, can be read from the matrix element of the unphysical process $\psi^-(p) \to \psi^-(p')A'(q)$. This process can schematically be denoted by something that looks like the familiar QED vertex [4]

$$i\mathcal{M} = \bar{\psi}(p')\Gamma^\mu\psi(p)A'_\mu(q), \tag{2.1}$$

where the four-momentum of the DP is given by $q = p - p'$ and Γ^μ gives the Feynman rules of the vertex. These interactions are provided in [4] and stated in equation (2.2). Here an i is included in the Γ^μ while in [4] it is not.

$$\Gamma^\mu = ie\epsilon Q_f\gamma^\mu - \frac{1}{\tilde{\Lambda}_f}\sigma^{\mu\nu}q_\nu\left[M(q^2) + iE(q^2)\gamma^5\right] + \frac{i}{\tilde{\Lambda}_f^2}(q^2\gamma^\mu - q^\mu q_\nu\gamma^\nu)\left[C(q^2) - A(q^2)\gamma^5\right]. \tag{2.2}$$

In the above expression, γ^μ is the Dirac gamma matrices, $\gamma^5 = i\gamma^0\gamma^1\gamma^2\gamma^3$, and $\sigma^{\mu\nu} = \frac{i}{2}[\gamma^\mu, \gamma^\nu]$. The first term, which looks very similar to the QED vertex with only an extra coupling constant ϵ, comes from the theory of KM [2–4], as mentioned in chapter 1. M, E, C, A are form factors and, as written explicitly in the equation, are functions of the DP momentum squared, q^2. However, these factors, called magnetic and electric dipole, charge, and anapole moment, can for the purposes

of this thesis be treated as constants. To more easily study the behaviour of the model and the size of the couplings the mass scale factor, $\tilde{\Lambda}_f$, and the now assumed constant form factors are absorbed into the more general coupling constants g_D and g'_D. These will then be dimensionful and have different units $[g_D] = \text{GeV}^{-1}$ and $[g'_D] = \text{GeV}^{-2}$, to compensate the units of the momentum factor(s) in the higher order electromagnetic terms. Note that the notation seems to suggest that the coupling constants, for example, of magnetic and electric dipole interactions are equal, but this is not necessarily the case. Even though the form factors are not explicitly included in the calculations throughout the thesis the different interactions presented in this model will still be referred to as KM, magnetic, electric, charge and anapole. Each of these interactions will be treated separately and compared. As a side note the addition of the γ^5 in the electric and anapole case makes them CP-violating.

To be able to further understand these interactions, and implement them in the simulation software, the interaction Lagrangian in position space is needed. The Lagrangian can be inferred from imposing that it generates the correct Feynman rules for the electron DP vertex and knowing that derivatives on the position coordinate acting on the fields provide a momentum factor when Wick contracted in the S-matrix calculations. The interaction Lagrangian derived in this fashion is shown in equation (2.3), and the full calculation of the Feynman rules, verifying that they are the same as given in equation (2.2), can be found in appendix A.2.

$$\begin{aligned}\mathcal{L}_I(x) = &\underbrace{e\epsilon\bar{\psi}\gamma^\mu\psi A'_\mu}_{\text{KM}} - \underbrace{g_D\partial_\nu(\bar{\psi}\sigma^{\mu\nu}\psi)A'_\mu}_{\text{Magnetic}} - \underbrace{ig_D\partial_\nu(\bar{\psi}\sigma^{\mu\nu}\gamma^5\psi)A'_\mu}_{\text{Electric}} - \\ &- \underbrace{g'_D\left[\Box(\bar{\psi}\gamma^\mu\psi) - \partial^\mu\partial_\nu(\bar{\psi}\gamma^\nu\psi)\right]A'_\mu}_{\text{Charge}} + \\ &+ \underbrace{g'_D\left[\Box(\bar{\psi}\gamma^\mu\gamma^5\psi) - \partial^\mu\partial_\nu(\bar{\psi}\gamma^\nu\gamma^5\psi)\right]A'_\mu}_{\text{Anapole}}\end{aligned} \tag{2.3}$$

2.2 Production Processes of the Dark Photon at LDMX

In the LDMX framework, the production process considered for the DP in this thesis is $e^- N_W \to e^- N_W A'$. This describes an incoming electron beam that scatters off the tungsten nucleus, N_W, and creates a DP in a bremsstrahlung like process, see figure 2.1. As seen in the figure the two contributing diagrams are: the one where the scattered electron emits a DP, or the one where the incoming electron emits a DP. In both cases the nucleus interacts with the electron through the regular photon γ. The dark mediator particle, the DP, can then in a later stage decay into DM. This will not be taken into account here as the process of interest is the production of the DP itself and the focus of LDMX, and the simulations made, is to recreate the electron energy and transverse momentum. This means that the DP will be treated on-shell.

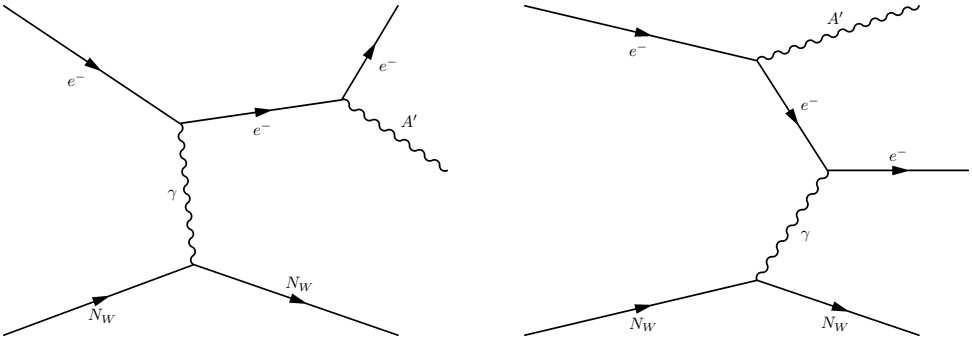

Figure 2.1: Feynman diagrams of the bremsstrahlung process considered for the DP creation at the LDMX.

2.3 Matrix Elements for Annihilation of Scalar Dark Matter

To learn more about the properties of the model and to crosscheck the calculation of the relic density one can calculate the matrix elements for the annihilation of DM. In the equations the DM field is called χ and the annihilation process considered is that of DM to electrons and positrons via the DP. Here, this is done assuming elastic complex scalar DM, naturally one could also assume other types of DM such as inelastic complex scalars, Majorana or Dirac fermions [3] or even spin-1 particles [29], but for clarity this is not done here. One can introduce the scalar DM via the following addition to the total Lagrangian [3]

$$\mathcal{L}_I^S = -g_{DM} A'_\mu (\chi^* \partial^\mu \chi - \chi \partial^\mu \chi^*). \tag{2.4}$$

Here g_{DM} is a new coupling constant of the vertex between two DM particles and the DP. This gives rise to the following vertex, derived from the unphysical process $\chi(p) \to \chi(p')A'(q)$ in appendix A.1,

$$\chi \to \chi A' \sim -ig_{DM}(p^\mu + p'^\mu). \tag{2.5}$$

Where p is the four-momentum of the incoming and p' of the outgoing DM particle.

Moving to the annihilation of DM this will be through the s-channel process $\chi(p_1)\chi^*(p_2) \to e^-(k_1)e^+(k_2)$ shown in figure 2.2, since there is no interaction defined directly between the DM particles and the SM particles. As seen in the figure the DP momentum definition is changed, from the calculation of the DP DM vertex, and is now $q = p_1 + p_2$, which yields the Mandelstam variable $s = q^2$. By using the Feynman rules in equation (2.2) and (2.5) one can write down the matrix element of the process for the different couplings. Proceeding with standard QFT calculations, such as spin sum rules and trace identities, it is possible to obtain the squared matrix element

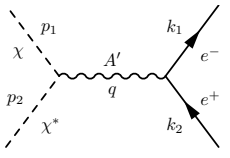

Figure 2.2: The s-channel process for complex scalar DM annihilation into SM electrons through a DP mediator.

averaged over initial state spins and summed over final state ones, $\overline{|\mathcal{M}|^2}$, which is done in appendix B. The result of that calculation, defining here also the difference in the incoming particles four momenta $d \equiv p_1 - p_2$, is the following

$$\begin{aligned}
\overline{|\mathcal{M}|^2}_{\text{KM}} =& \frac{4g_{DM}^2\epsilon^2e^2}{(q^2-m_{A'}^2)^2+m_{A'}^2\Gamma_{A'}^2}\left[2(d\cdot k_1)(d\cdot k_2)-(k_1\cdot k_2)d^2-m_e^2d^2\right] \\
\overline{|\mathcal{M}|^2}_{\text{Magnetic}} =& \frac{4g_{DM}^2g_D^2}{(q^2-m_{A'}^2)^2+m_{A'}^2\Gamma_{A'}^2}\times \\
& \times\left[d^2q^2(k_1\cdot k_2)-2d^2(k_1\cdot q)(k_2\cdot q)-2q^2(d\cdot k_1)(d\cdot k_2)-m_e^2d^2q^2\right] \\
\overline{|\mathcal{M}|^2}_{\text{Electric}} =& \frac{4g_{DM}^2g_D^2}{(q^2-m_{A'}^2)^2+m_{A'}^2\Gamma_{A'}^2}\times \\
& \times\left[d^2q^2(k_1\cdot k_2)-2d^2(k_1\cdot q)(k_2\cdot q)-2q^2(d\cdot k_1)(d\cdot k_2)+m_e^2d^2q^2\right] \\
\overline{|\mathcal{M}|^2}_{\text{Charge}} =& \frac{4g_{DM}^2g_D'^2}{(q^2-m_{A'}^2)^2+m_{A'}^2\Gamma_{A'}^2}q^4[2(d\cdot k_1)(d\cdot k_2)-d^2(k_1\cdot k_2)-m_e^2d^2] \\
\overline{|\mathcal{M}|^2}_{\text{Anapole}} =& \frac{4g_{DM}^2g_D'^2}{(q^2-m_{A'}^2)^2+m_{A'}^2\Gamma_{A'}^2}q^4[2(d\cdot k_1)(d\cdot k_2)-d^2(k_1\cdot k_2)+m_e^2d^2].
\end{aligned} \tag{2.6}$$

To arrive at the above equations the fact that $d\cdot q = 0$ is also used, where $d\cdot q$ means the contraction of the Lorentz indices, i.e. $d^\mu q_\mu$. The $\Gamma_{A'}$ is the decay rate of the DP, which is included to deal with resonances. To be able to use these calculations further one can move to the center-of-mass (CM) frame, and with the definitions as in figure 2.3, one finds that $d = (0, 2\vec{p})$ and $q = (2E, 0)$, giving $q^2 = 4E^2 = s$. Here $\vec{p}$ gives the three-momentum of the DM particle and E is half the CM energy.

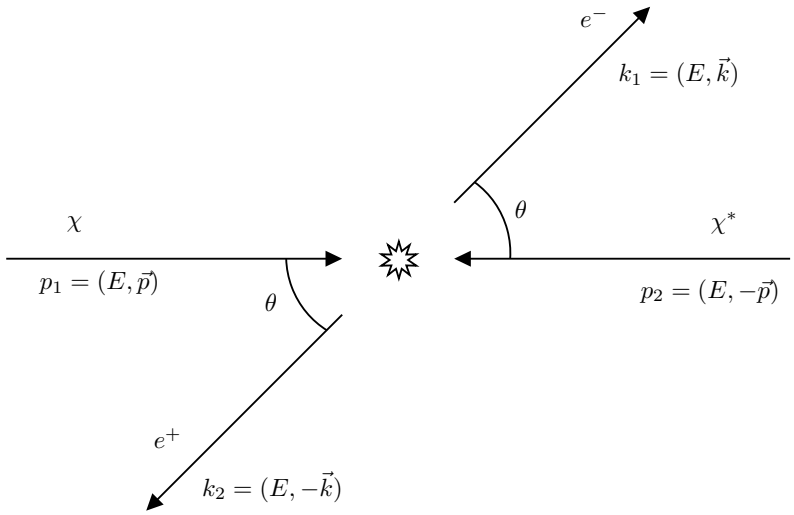

Figure 2.3: Schematic picture of the annihilation process of DM into an electron and a positron shown in the CM frame of the interaction.

Making the contractions of the Lorentz indices in the equations in (2.6) one finds

that in the CM frame the matrix elements described by the energy of the particles, the absolute value of their three-momentum and the CM scattering angle, θ, becomes

$$\begin{aligned}
\overline{|\mathcal{M}|^2}^{\mathrm{CM}}_{\mathrm{KM}} =& \frac{32 g_{DM}^2 \epsilon^2 e^2}{(4E^2 - m_{A'}^2)^2 + m_{A'}^2 \Gamma_{A'}^2} |\vec{p}|^2 (E^2 - |\vec{k}|^2 cos^2\theta) \\
\overline{|\mathcal{M}|^2}^{\mathrm{CM}}_{\mathrm{Magnetic}} =& \frac{128 g_{DM}^2 g_D^2}{(4E^2 - m_{A'}^2)^2 + m_{A'}^2 \Gamma_{A'}^2} E^2 |\vec{p}|^2 (|\vec{k}|^2 cos^2\theta + m_e^2) \\
\overline{|\mathcal{M}|^2}^{\mathrm{CM}}_{\mathrm{Electric}} =& \frac{128 g_{DM}^2 g_D^2}{(4E^2 - m_{A'}^2)^2 + m_{A'}^2 \Gamma_{A'}^2} E^2 |\vec{p}|^2 |\vec{k}|^2 cos^2\theta \\
\overline{|\mathcal{M}|^2}^{\mathrm{CM}}_{\mathrm{Charge}} =& \frac{512 g_{DM}^2 g_D'^2}{(4E^2 - m_{A'}^2)^2 + m_{A'}^2 \Gamma_{A'}^2} E^4 |\vec{p}|^2 (E^2 - |\vec{k}|^2 cos^2\theta) \\
\overline{|\mathcal{M}|^2}^{\mathrm{CM}}_{\mathrm{Anapole}} =& \frac{512 g_{DM}^2 g_D'^2}{(4E^2 - m_{A'}^2)^2 + m_{A'}^2 \Gamma_{A'}^2} E^4 |\vec{p}|^2 |\vec{k}|^2 sin^2\theta.
\end{aligned} \tag{2.7}$$

Integrating over the solid angle, $\int d\Omega$, results in

$$\begin{aligned}
\int \overline{|\mathcal{M}|^2}^{\mathrm{CM}}_{\mathrm{KM}} d\Omega =& \frac{32 \cdot 4\pi g_{DM}^2 \epsilon^2 e^2}{(4E^2 - m_{A'}^2)^2 + m_{A'}^2 \Gamma_{A'}^2} |\vec{p}|^2 (E^2 - \frac{1}{3}|\vec{k}|^2) \\
\int \overline{|\mathcal{M}|^2}^{\mathrm{CM}}_{\mathrm{Magnetic}} d\Omega =& \frac{128 \cdot 4\pi g_{DM}^2 g_D^2}{(4E^2 - m_{A'}^2)^2 + m_{A'}^2 \Gamma_{A'}^2} E^2 |\vec{p}|^2 (\frac{1}{3}|\vec{k}|^2 + m_e^2) \\
\int \overline{|\mathcal{M}|^2}^{\mathrm{CM}}_{\mathrm{Electric}} d\Omega =& \frac{128 \cdot 4\pi g_{DM}^2 g_D^2}{(4E^2 - m_{A'}^2)^2 + m_{A'}^2 \Gamma_{A'}^2} \frac{1}{3} E^2 |\vec{p}|^2 |\vec{k}|^2 \\
\int \overline{|\mathcal{M}|^2}^{\mathrm{CM}}_{\mathrm{Charge}} d\Omega =& \frac{512 \cdot 4\pi g_{DM}^2 g_D'^2}{(4E^2 - m_{A'}^2)^2 + m_{A'}^2 \Gamma_{A'}^2} E^4 |\vec{p}|^2 (E^2 - \frac{1}{3}|\vec{k}|^2) \\
\int \overline{|\mathcal{M}|^2}^{\mathrm{CM}}_{\mathrm{Anapole}} d\Omega =& \frac{1024 \cdot 4\pi g_{DM}^2 g_D'^2}{(4E^2 - m_{A'}^2)^2 + m_{A'}^2 \Gamma_{A'}^2} \frac{1}{3} E^4 |\vec{p}|^2 |\vec{k}|^2.
\end{aligned} \tag{2.8}$$

Further, one can also calculate the decay rates, $\Gamma_{A'}$, of the DP. For the $1 \to 2$ process of the decay of the DP, the differential decay rate is given by equation (4.86) in [30]

$$d\Gamma_{A' \to 1+2} = \frac{1}{2m_{A'}} \overline{|\mathcal{M}_{A' \to 1+2}|^2} \frac{d^3 p_1}{(2\pi)^3} \frac{1}{2E_1} \frac{d^3 p_2}{(2\pi)^3} \frac{1}{2E_2} (2\pi)^4 \delta^{(4)}(p_{A'} - p_1 - p_2) \tag{2.9}$$

The decay rate is defined in the rest frame of the A'. Looking at the DP coupled to

DM and the SM electron and positron, the $A' \to 1+2$ matrix elements possible are

$$\begin{aligned}
\overline{|\mathcal{M}_{A'\to\chi+\chi^*}|^2} &= \frac{g_{DM}^2}{3}(m_{A'}^2 - 4m_\chi^2) \\
\overline{|\mathcal{M}_{A'\to e^-+e^+}|^2}_{\text{KM}} &= \frac{e^2\epsilon^2}{3}(4m_{A'}^2 + 8m_e^2) \\
\overline{|\mathcal{M}_{A'\to e^-+e^+}|^2}_{\text{Magnetic}} &= \frac{g_D^2}{3}(16m_e^2 m_{A'}^2 + 2m_{A'}^4) \\
\overline{|\mathcal{M}_{A'\to e^-+e^+}|^2}_{\text{Electric}} &= \frac{g_D^2}{3}(m_{A'}^4 - 4m_{A'}^2 m_e^2) \\
\overline{|\mathcal{M}_{A'\to e^-+e^+}|^2}_{\text{Charge}} &= \frac{4g_D'^2}{3}(m_{A'}^6 + 2m_{A'}^4 m_e^2) \\
\overline{|\mathcal{M}_{A'\to e^-+e^+}|^2}_{\text{Anapole}} &= \frac{4g_D'^2}{3}(m_{A'}^6 - 4m_{A'}^4 m_e^2).
\end{aligned} \tag{2.10}$$

The calculations for these decay rates are shown in detail for $A' \to \chi\chi^*$ in appendix C, where the other decays are also discussed. The first three decay rates are calculated by hand and crosschecked with the program FeynRules and the last three are fully calculated with FeynRules, due to the agreement between the by hand and the computer generated calculations. As one can see the matrix elements are not dependent on the momentum of any of the particles and when integrating $d\Gamma_{A'\to 1+2}$ one can bring $\overline{|\mathcal{M}_{A'\to 1+2}|^2}$ out of the integral. The decay rate becomes, using the properties of the Dirac delta, spherical coordinates and also knowing that $m_1 = m_2$,

$$\begin{aligned}
\Gamma_{A'\to 1+2} &= \frac{\overline{|\mathcal{M}_{A'\to 1+2}|^2}}{8\pi^2 m_{A'}} \int \frac{d^3p_1 d^3p_2}{4E_1E_2}\delta(E_{A'} - E_1 - E_2)\delta^{(3)}(\vec{p}_{A'} - \vec{p}_1 - \vec{p}_2) = \\
&= \{\vec{p}_{A'} = 0,\ A' \text{ at rest},\ \implies\ p_1^2 = p_2^2, E_{A'} = m_{A'}\} = \\
&= \{m_1 = m_2 \equiv m_{12}\ \implies\ E_1 = E_2 \equiv E\} = \\
&= \frac{\overline{|\mathcal{M}_{A'\to 1+2}|^2}}{8\pi^2 m_{A'}} \int \frac{d^3p_1}{4E^2}\delta(m_{A'} - 2E) = \\
&= \frac{\overline{|\mathcal{M}_{A'\to 1+2}|^2}}{8\pi^2 m_{A'}} 4\pi \int \frac{1}{4E^2}\delta(m_{A'} - 2E)|\vec{p_1}|^2 d|\vec{p_1}| = \\
&= \{|\vec{p}_1|^2 = E^2 - m_{12}^2\} = \\
&= \frac{\overline{|\mathcal{M}_{A'\to 1+2}|^2}}{8\pi m_{A'}^2}\sqrt{\frac{m_{A'}^2}{4} - m_{12}^2}.
\end{aligned} \tag{2.11}$$

The 4π in front of the final integral comes from integrating the solid angle. This is the same result for the integrated decay rate as is found in [31]. Then since decay rates for different final states add [30] the total decay rate is given by

$$\Gamma_{A'} = \Gamma_{A'\to e^-+e^+} + \Gamma_{A'\to\chi+\chi^*}. \tag{2.12}$$

The matrix elements and decay rates can then be used to calculate the thermally averaged cross section times velocity, which one could use further to obtain the relic density, for the case of scalar DM coupling to the electron.

2.4 Relic Abundance from the Boltzmann Equation

Focusing on the freeze-out mechanism in the early universe it is possible, using the Boltzmann equation stated in section 1.2, to calculate the relic abundance of DM. In other words what is left after freeze-out until today's CMB temperature for a particle species χ. Previously χ has denoted DM and since that is what is of interest in this thesis it is also used here, but this is more general than just for DM since as stated in section 1.2 other particles in the equilibrium freeze-out as well. Following the works of [15] and [32] the evolution of the yield, Y, which relates to the density can be derived. However, before moving to the yield it is easiest to first obtain a description of how the number density of a particle species, n_χ, changes. This is done by integrating the Boltzmann equation, equation (1.11) over the momentum and multiplying it with the internal degrees of freedom for that particle, since the relation between the phase-space density and the number density is that of equation (1.3). Assuming that the universe is an isotropic and homogeneous Friedman-Robertson-Walker universe the left hand side of the Boltzmann equation, the Liouville operator L, takes the form [15, 32]

$$L[f_\chi] = \frac{\partial f_\chi}{\partial t} - H\frac{|\vec{p}_\chi|^2}{E_\chi}\frac{\partial f_\chi}{\partial E_\chi}. \tag{2.13}$$

The integral over momentum can then be evaluated using $E_\chi = \sqrt{|p_\chi|^2 + m_\chi^2}$, spherical coordinates and integration by parts. This results in

$$\begin{aligned} g_\chi \int L[f_\chi]\frac{d^3\vec{p}}{(2\pi)^3} &= g_\chi \frac{\partial}{\partial t}\int f\frac{d^3\vec{p}}{(2\pi)^3} - g_\chi H \int \frac{|\vec{p}_\chi|^2}{E_\chi}\frac{\partial f_\chi}{\partial |p_\chi|}\frac{\partial |\vec{p}_\chi|}{\partial E_\chi}\frac{d^3\vec{p}}{(2\pi)^3} = \\ &= \left\{\frac{\partial |\vec{p}_\chi|}{\partial E_\chi} = \frac{E_\chi}{|\vec{p}_\chi|}\right\} = \dot{n} - g_\chi H \int d\Omega \int |\vec{p}_\chi|^3 \frac{\partial f_\chi}{\partial |\vec{p}_\chi|}\frac{d|\vec{p}_\chi|}{(2\pi)^3} = \\ &= \dot{n}_\chi - g_\chi H \int d\Omega \left(\left[\frac{|\vec{p}_\chi|^3 f_\chi}{(2\pi)^3}\right] - 3\int f_\chi |\vec{p}_\chi|^2 \frac{d|\vec{p}_\chi|}{(2\pi)^3}\right) = \\ &= \dot{n}_\chi + 3Hn_\chi. \end{aligned} \tag{2.14}$$

Here the assumption of the isotropy of f is used and it is therefore not a function of the solid angle. It is also assumed that f follows the Maxwell-Boltzman distribution and is therefore zero at $|\vec{p}_\chi| = \infty$. Now move to the collision operator, C, to describe how the particle species interacts with other particles in the thermal equilibrium. Let $\sum|\mathcal{M}|^2$ symbolise the matrix element squared summed over initial and final state spins, this thesis takes the convention that $\overline{|\mathcal{M}|^2}$ denotes average over initial and sum over final state spins, then the integrated C has a general expression for

any process $\chi + i + \cdots \leftrightarrow f + \cdots$, namely [15, 32]

$$\begin{aligned} g_\chi \int C[f_\chi] \frac{d^3\vec{p}}{(2\pi)^3} = -\int \big[\sum |\mathcal{M}|^2_{\chi+i+\cdots\to f+\cdots} f_\chi f_i \cdots (1 \pm f_f) \cdots \\ - \sum |\mathcal{M}|^2_{f+\cdots\to\chi+i+\cdots} f_f \cdots (1 \pm f_\chi)(1 \pm f_i) \cdots \big] \times \\ \times (2\pi)^4 \delta^{(4)}(p_\chi + p_i + \cdots - p_f - \cdots) \times \\ \times \frac{d^3\vec{p}_\chi}{(2\pi)^3 2E_\chi} \frac{d^3\vec{p}_i}{(2\pi)^3 2E_i} \cdots \frac{d^3\vec{p}_f}{(2\pi)^3 2E_f} \cdots . \end{aligned} \tag{2.15}$$

The $1 \pm f$ factors come from the statistics being used, fermions or bosons, but as mentioned in section 1.2.1 the particles in the thermal equilibrium will be treated with Maxwell-Boltzmann statistics and the chemical potential will be approximated to zero, $f = e^{-E/T}$, this makes the $\pm$ factors negligible [15, 32]. A further approximation that is made is that the process is invariant under time reversal symmetry, making $\sum |\mathcal{M}|^2_{\chi+i+\cdots\to f+\cdots} = \sum |\mathcal{M}|^2_{f+\cdots\to\chi+i+\cdots}$ [15, 32]. This changes the Boltzmann equation, including both the Liouville and the collision operator, to

$$\begin{aligned} \dot{n}_\chi + 3Hn_\chi = -\int \overline{|\mathcal{M}|^2}_{\chi+i+\cdots\to f+\cdots} [f_\chi f_i \cdots - f_f \cdots] \times \\ \times (2\pi)^4 \delta^{(4)}(p_\chi + p_i + \cdots - p_f - \cdots) \times \\ \times g_\chi \frac{d^3\vec{p}_\chi}{(2\pi)^3 2E_\chi} g_i \frac{d^3\vec{p}_i}{(2\pi)^3 2E_i} \cdots \frac{d^3\vec{p}_f}{(2\pi)^3 2E_f} \cdots . \end{aligned} \tag{2.16}$$

Note in the equation that there is no spin factor for the final state particles and that the ones included for the initial state ones are cancelled by $\overline{|\mathcal{M}|^2}$. Now to simplify one can consider the $2 \leftrightarrow 2$ annihilation process of a species into particles in the thermal equilibrium $\chi\bar{\chi} \to \psi\bar{\psi}$, the only process that will be considered in this thesis. To avoid statistical prefactors from identical initial or final states it is assumed that $\chi \neq \bar{\chi}$ and $\psi \neq \bar{\psi}$, which is also the case in this thesis. If one wants to look at other cases a factor of $\frac{1}{k!}$, where k is the number of identical particles, is to be included in the collision term [15]. However, if the initial state particles are identical, then also a combinatorial factor of 2 would be included since there would be two of that particle species annihilating in each interaction [32]. This would cancel the factor from identical initial states. Further, annihilation products of χ and $\bar{\chi}$, or the particles involved in the creation process, are considered to be contained in the thermal bath and due to this can be treated with their equilibrium distributions, f^{EQ}_ψ and $f^{EQ}_{\bar{\psi}}$ [15, 32]. An advantage of this is that one can then relate the equilibrium distributions for the initial and final state particles by using the properties of the four-momentum conserving δ-function in the integral of the collision term in the following way [15],

$$f^{EQ}_\psi f^{EQ}_{\bar{\psi}} = e^{-\frac{(E_\psi + E_{\bar{\psi}})}{T}} = \{\delta(E_\psi + E_{\bar{\psi}} - E_\chi - E_{\bar{\chi}})\} = e^{-\frac{(E_\chi + E_{\bar{\chi}})}{T}} = f^{EQ}_\chi f^{EQ}_{\bar{\chi}}. \tag{2.17}$$

The Boltzmann equation, equation 2.16, for this $2 \leftrightarrow 2$ process then becomes

$$\begin{aligned}\dot{n}_\chi + 3Hn_\chi = -\int \overline{|\mathcal{M}|^2}_{\chi+\bar{\chi}\to\psi+\bar{\psi}}[f_\chi f_{\bar{\chi}} - f_\chi^{EQ} f_{\bar{\chi}}^{EQ}]\times \\ \times(2\pi)^4\delta^{(4)}(p_\chi + p_{\bar{\chi}} - p_\psi - p_{\bar{\psi}})\times \\ \times g_\chi \frac{d^3\vec{p}_\chi}{(2\pi)^3 2E_\chi} g_{\bar{\chi}} \frac{d^3\vec{p}_{\bar{\chi}}}{(2\pi)^3 2E_{\bar{\chi}}} \frac{d^3\vec{p}_\psi}{(2\pi)^3 2E_\psi} \frac{d^3\vec{p}_{\bar{\psi}}}{(2\pi)^3 2E_{\bar{\psi}}}.\end{aligned} \tag{2.18}$$

To further simplify the expression one can utilise that the cross section of the annihilation process, $\sigma_{\chi+\bar{\chi}\to\psi+\bar{\psi}}$, times the velocity $v \equiv \sqrt{(p_\chi \cdot p_{\bar{\chi}})^2 - m_\chi^2 m_{\bar{\chi}}^2}/E_\chi E_{\bar{\chi}}$ is given by [32]

$$\sigma_{\chi+\bar{\chi}\to\psi+\bar{\psi}} v \equiv \frac{1}{2E_\chi 2E_{\bar{\chi}}} \int \overline{|\mathcal{M}|^2}_{\chi+\bar{\chi}\to\psi+\bar{\psi}} (2\pi)^4 \delta^{(4)}(p_\chi + p_{\bar{\chi}} - p_\psi - p_{\bar{\psi}}) \frac{d^3\vec{p}_\psi}{(2\pi)^3 2E_\psi} \frac{d^3\vec{p}_{\bar{\psi}}}{(2\pi)^3 2E_{\bar{\psi}}}. \tag{2.19}$$

Now the start of a workable expression begins to take form and equation (2.18) becomes

$$\dot{n}_\chi + 3Hn_\chi = -\int \sigma_{\chi+\bar{\chi}\to\psi+\bar{\psi}} v [f_\chi f_{\bar{\chi}} - f_\chi^{EQ} f_{\bar{\chi}}^{EQ}] g_\chi \frac{d^3\vec{p}_\chi}{(2\pi)^3} g_{\bar{\chi}} \frac{d^3\vec{p}_{\bar{\chi}}}{(2\pi)^3}. \tag{2.20}$$

It is customary to write it in terms of the thermally averaged cross section times velocity which is defined as [15, 32]

$$\langle \sigma_{\chi+\bar{\chi}\to\psi+\bar{\psi}} v \rangle \equiv \frac{1}{n_\chi^{EQ} n_{\bar{\chi}}^{EQ}} \int \sigma_{\chi+\bar{\chi}\to\psi+\bar{\psi}} v f_\chi^{EQ} f_{\bar{\chi}}^{EQ} g_\chi \frac{d^3\vec{p}_\chi}{(2\pi)^3} g_{\bar{\chi}} \frac{d^3\vec{p}_{\bar{\chi}}}{(2\pi)^3}. \tag{2.21}$$

It is good to include here that to obtain $\langle \sigma_{\chi+\bar{\chi}\to\psi+\bar{\psi}} v \rangle$ a very handy expression derived in [32] is

$$\langle \sigma_{\chi+\bar{\chi}\to\psi+\bar{\psi}} v \rangle = \frac{1}{8m_\chi^4 T K_2^2(m/T)} \int_{4m_\chi^2}^\infty \sigma_{\chi+\bar{\chi}\to\psi+\bar{\psi}} (s - 4m_\chi^2) \sqrt{s} K_1(\sqrt{s}/T) ds, \tag{2.22}$$

where $K_{1/2}$ are modified Bessel functions of order 1 or 2, and $s = (p_\chi + p_{\bar{\chi}})^2$ is the invariant Mandelstam variable for the s-channel. Moving forward to be able to use the definition of the thermally averaged cross section times velocity, equation 2.21, and rewrite the Boltzmann equation, now given by equation 2.20, one has to assume that the particles stay in kinetic equilibrium with the ones in the thermal bath even after decoupling, which means that their distributions can be described by the thermal equilibrium distributions, f^{EQ}, times a prefactor only dependent on time, $\xi(t)$, meaning that $f = \xi(t) f^{EQ}$ for a particle still in kinetic equilibrium [32, 33]. Since $\xi(t)$ is not dependent on the three-momentum it can be brought out of

the integral and equation (2.20) now becomes

$$\begin{aligned}\dot{n}_\chi + 3Hn_\chi =& -\frac{n_\chi^{EQ} n_{\bar{\chi}}^{EQ}}{n_\chi^{EQ} n_{\bar{\chi}}^{EQ}} \xi_\chi(t)\xi_{\bar{\chi}}(t) \int \sigma_{\chi+\bar{\chi}\to\psi+\bar{\psi}} v f_\chi^{EQ} f_{\bar{\chi}}^{EQ} g_\chi \frac{d^3\vec{p}_\chi}{(2\pi)^3} g_{\bar{\chi}} \frac{d^3\vec{p}_{\bar{\chi}}}{(2\pi)^3} \\ &+ \langle\sigma_{\chi+\bar{\chi}\to\psi+\bar{\psi}} v\rangle n_\chi^{EQ} n_{\bar{\chi}}^{EQ} = \\ =&\{f = \xi(t) f^{EQ} \implies n = \xi(t) n^{EQ}\} = \\ =& -\langle\sigma_{\chi+\bar{\chi}\to\psi+\bar{\psi}} v\rangle (n_\chi n_{\bar{\chi}} - n_\chi^{EQ} n_{\bar{\chi}}^{EQ}) \end{aligned} \tag{2.23}$$

$$\implies \dot{n}_\chi + 3Hn_\chi = -\langle\sigma_{\chi+\bar{\chi}\to\psi+\bar{\psi}} v\rangle (n_\chi n_{\bar{\chi}} - n_\chi^{EQ} n_{\bar{\chi}}^{EQ}).$$

The stated equation gives the number density for the χ particles. However, for a DM contender one is interested in the total density generated by all possible species [32]. In this example it would be only the particle and the antiparticle, and the total number density would become $n = n_\chi + n_{\bar{\chi}}$. This would then contribute to the total relic abundance and can be compared to that measured from the anisotropies in the CMB. Due to the fact that the chemical potential is assumed to be zero, or at least very small, both in and outside equilibrium, the number of particles and antiparticles are equal, $n_\chi = n_{\bar{\chi}}$ [32]. If there was a matter/anti-matter asymmetry included then the chemical potential could not be neglected. This makes $n = 2n_\chi$ and the equation for the total density becomes

$$\frac{1}{2}\dot{n} + 3H\frac{1}{2}n = -\langle\sigma_{\chi+\bar{\chi}\to\psi+\bar{\psi}} v\rangle \left(\left(\frac{1}{2}n\right)^2 - \left(\frac{1}{2}n^{EQ}\right)^2\right) \tag{2.24}$$

$$\implies \dot{n} + 3Hn = -\frac{1}{2}\langle\sigma_{\chi+\bar{\chi}\to\psi+\bar{\psi}} v\rangle (n^2 - n^{EQ2}). \tag{2.25}$$

Of course also $m_\chi = m_{\bar{\chi}}$. In the studies that follow the $\frac{1}{2}$ accounting for both the particles and antiparticles will be included in the calculation of the thermally averaged cross section times velocity and therefore it will be stated as $\frac{1}{2}\langle\sigma_{\chi+\bar{\chi}\to\psi+\bar{\psi}} v\rangle$ in the results to make this explicit. Moving forward to account for the expansion of the universe one should change variables [15, 32] to get the equation in terms of the yield $Y = n/s$, which is comoving, and the equilibrium yield $Y^{EQ} = n^{EQ}/s$,

$$\begin{aligned} \frac{d(sY)}{dt} + 3H(sY) &= -\frac{1}{2}\langle\sigma_{\chi+\bar{\chi}\to\psi+\bar{\psi}} v\rangle ((sY)^2 - (sY^{EQ})^2) \\ \{\frac{d(sa^3Y/a^3)}{dt} &= sa^3\left(\frac{1}{a^3}\frac{dY}{dt} - 3\frac{Y}{a^4}\frac{da}{dt}\right)\} \\ \implies \dot{Y} - 3\frac{Y}{a}\dot{a} + 3HY &= -s\frac{1}{2}\langle\sigma_{\chi+\bar{\chi}\to\psi+\bar{\psi}} v\rangle (Y^2 - Y^{EQ2}) \\ \implies \dot{Y} &= -s\frac{1}{2}\langle\sigma_{\chi+\bar{\chi}\to\psi+\bar{\psi}} v\rangle (Y^2 - Y^{EQ2}). \end{aligned} \tag{2.26}$$

In the above it is used that the total entropy of the comoving volume, $S = sa^3$, is assumed to be conserved, i.e. it has zero time derivative. It is standard to work

with the ratio between the mass and temperature instead of time which motivates the change from t to $x = \frac{m_\chi}{T}$. For the equilibrium yield of the species χ this can be calculated and is described by [32]

$$Y_\chi^{EQ} = \frac{45 g_\chi x^2 K_2(x)}{4\pi^4 h_{*,s}(T)}. \tag{2.27}$$

To make the change of variables for the entire expression the following equivalence, also based on the assumption of constant total entropy $S = sa^3$, is needed

$$\begin{aligned} \frac{dY}{dx} = \frac{dY}{da}\frac{da}{dx} = \frac{dY}{dt}\frac{1}{\frac{da}{dt}}\frac{d(S^{1/3}/s^{1/3})}{dx} = -\frac{1}{3}\dot{Y}\frac{1}{\dot{a}}\frac{S^{1/3}}{s^{4/3}}\frac{ds}{dx} \\ \implies \dot{Y} = -3Hs\frac{1}{\frac{ds}{dx}}\frac{dY}{dx}. \end{aligned} \tag{2.28}$$

The x derivative of s can be evaluated by using that it is a function of T given by equation (1.9), and that x is inversely proportional to the temperature. The derivative becomes

$$\frac{ds}{dx} = \frac{dT}{dx}\frac{d}{dT}\left(\frac{2\pi^2}{45} h_{*,s} T^3\right) = -\frac{2\pi^2}{45}\frac{m_\chi T^2}{x^2}\left(3h_{*,s} + T\frac{dh_{*,s}}{dT}\right). \tag{2.29}$$

Using the expression for H in the radiation dominated era, equation (1.7), and substituting equation (2.28) into (2.26), one ends up with the Boltzmann equation given in terms of the yield and x,

$$\begin{aligned} \frac{dY}{dx} &= \frac{1}{3H}\frac{ds}{dx}\frac{1}{2}\langle\sigma_{\chi+\bar{\chi}\to\psi+\bar{\psi}}v\rangle(Y^2 - Y^{EQ^2}) = \\ &= \frac{1}{3\left(\sqrt{\frac{8\pi^3 g_{*,E}}{90}}\frac{T^2}{m_P}\right)}\left(-\frac{2\pi^2}{45}\frac{m_\chi T^2}{x^2}\left(3h_{*,s} + T\frac{dh_{*,s}}{dT}\right)\right)\frac{1}{2}\langle\sigma_{\chi+\bar{\chi}\to\psi+\bar{\psi}}v\rangle(Y^2 - Y^{EQ^2}) \\ &= -\sqrt{\frac{\pi}{45}}\frac{m_P m_\chi}{x^2}\underbrace{\frac{1}{\sqrt{g_{*,E}}}\left(h_{*,s} + \frac{T}{3}\frac{dh_{*,s}}{dT}\right)}_{\equiv g_*}\frac{1}{2}\langle\sigma_{\chi+\bar{\chi}\to\psi+\bar{\psi}}v\rangle(Y^2 - Y_\chi^{EQ^2}). \end{aligned} \tag{2.30}$$

In agreement with [32], the final differential equation, which is to be solved to determine the comoving density of the species after freeze-out, is then

$$\frac{dY}{dx} = \sqrt{\frac{\pi}{45}}\frac{m_P m_\chi}{x^2} g_* \frac{1}{2}\langle\sigma_{\chi+\bar{\chi}\to\psi+\bar{\psi}}v\rangle(Y^{EQ^2} - Y_\chi^2). \tag{2.31}$$

Returning to freeze-out, to solve equation 2.31 one has to find the temperature, or x, where χ decouples from the thermal equilibrium. One way to define this temperature is that it is the temperature where the difference between the yield and

the equilibrium yield is at a certain threshold, i.e. $\Delta \equiv Y - Y^{EQ} = \delta Y^{EQ}$, for some δ [32]. This is an approximation of course but gives a way to estimate the decoupling temperature without having the full Y_χ at hand. Substituting Y for Δ in equation 2.30 one arrives at

$$\frac{d\Delta}{dx} + \frac{dY^{EQ}}{dx} = \sqrt{\frac{\pi g_*}{45}} \frac{m_P m_\chi}{x^2} \frac{1}{2} \langle \sigma_{\chi+\bar{\chi}\to\psi+\bar{\psi}} v \rangle (Y^{EQ\,2} - (\Delta + Y^{EQ})^2) = \tag{2.32}$$

$$\frac{dY^{EQ}}{dx} = -\sqrt{\frac{\pi g_*}{45}} \frac{m_P m_\chi}{x^2} \frac{1}{2} \langle \sigma_{\chi+\bar{\chi}\to\psi+\bar{\psi}} v \rangle (\Delta^2 + 2\Delta Y^{EQ}). \tag{2.33}$$

The derivative of Δ is approximated to zero until freeze-out since χ is then still in the thermal bath and therefore $Y \approx Y^{EQ}$ [32]. Inserting our chosen freeze-out condition gives an equation to be solved for the freeze-out mass to temperature ratio $x = x_f$,

$$\frac{dY^{EQ}}{dx} = -\sqrt{\frac{\pi g_*}{45}} \frac{m_P m_\chi}{x^2} \frac{1}{2} \langle \sigma_{\chi+\bar{\chi}\to\psi+\bar{\psi}} v \rangle Y^{EQ\,2} (\delta^2 + 2\delta). \tag{2.34}$$

After calculating the freeze-out temperature x_f one can solve the final Boltzmann equation, equation 2.31, and obtain the present day yield by integrating from freeze-out x_f to present day CMB temperature x_0 [32]. The assumption that Y^{EQ} becomes small after the decoupling, due to it exponentially decaying, is made and therefore the equilibrium yield is not taken into account [32]. This gives the equation for the present day yield as

$$\frac{1}{Y_0} = \frac{1}{Y_f} + \sqrt{\frac{\pi}{45}} m_P \int_{x_f}^{x_0} \frac{m_\chi}{x^2} g_* \frac{1}{2} \langle \sigma_{\chi+\bar{\chi}\to\psi+\bar{\psi}} v \rangle dx. \tag{2.35}$$

Here Y_f is the yield at freeze-out and one way to approximate it is by using the equilibrium yield at x_f and making a deviation from this since the species has only just begun to depart from the equilibrium at this point, $Y_f = Y^{EQ}(x_f)(1+\delta)$ [17]. To then obtain the relic abundance, Ωh^2, which can be compared to measurements, one just uses the relation between the yield and the abundance given in equation 1.5.

2.5 The Weizsäcker-Williams Approximation

In this section a short intro to the Weizsäcker-Williams (WW) approximation is given and results derived for the KM interaction [34] and the magnetic dipole [4] are stated. This method and the results mentioned in this section can then be used to compare and validate some of the simulations of the MG5 generated energy distributions for a process in a LDMX like framework, see section 4.2.

The WW approximation is an approximation that allows for the simplification of the process of a scattering electron beam off a target nucleus where the electron emits a photon, or here a DP, through a bremsstrahlung like process [34]. In this thesis the considered nucleus is tungsten, denoted by N_W. Following the arguments of [34], the WW approximation reduces the process, described in section 2.2, $e^-(p)\, N_W(P_i) \to e^-(p')\, N_W(P_f)\, A'(q)$ to a prefactor times the sub-process

$e^-(p)\,\gamma(k) \rightarrow e^-(p')\,A'(q)$, by assuming that the incoming electron only interacts with a photon cloud surrounding the nucleus. Defining the energy of the incoming electron beam as E_0, for the case of LDMX $E_0 = 4\,\text{GeV}$ [3], one can define the ratio between the outgoing DP and the incoming electron beam as $x_{A'} \equiv E_{A'}/E_0$. Also defining the angle of the DP with respect to the beam axis as θ, which is considered to be small. It is also useful to define the function U, as is done in [34],

$$U = E_0^2\theta^2 x_{A'} + m_{A'}^2\frac{1-x_{A'}}{x_{A'}} + m_e^2 x_{A'}. \tag{2.36}$$

This approximation has been applied to calculate the double differential cross section in both [34], for the KM interaction, and [4], for the magnetic dipole case. The differential cross section for KM [34] is

$$\frac{d\sigma_{\text{KM}}^{\text{WW}}}{dx_{A'}dcos\theta} = Ax_{A'}\left[\frac{1-x_{A'}+x_{A'}^2/2}{U^2} + \frac{(1-x_{A'})^2 m_{A'}^2}{U^4}\left(m_{A'}^2 - \frac{Ux_{A'}}{1-x_{A'}}\right)\right]. \tag{2.37}$$

Where A is approximated to a constant, but in general this includes information about the nucleus and photon flux described further in [34]. The differential cross section for the magnetic dipole interaction looks like [4]

$$\frac{d\sigma_{\text{Magnetic}}^{\text{WW}}}{dx_{A'}dcos\theta} = B\frac{x_{A'}^2}{U}. \tag{2.38}$$

Where B is, as for A in the KM case, approximated to a constant, but as mentioned contains more information. The above cross sections are defined for the energy of the outgoing DP. However, in a collision experiment such as the LDMX one would be more interested in the outgoing electron energy, E_e, and momenta, p', since this is what the experiment would measure. To achieve a dependency of E_e, or the ratio $x_e \equiv E_e/E_0$, the energy part of the four-momentum conservation of the full process including the nucleus, is considered. In the lab frame the target is stationary meaning that $P_i = (M_N, \vec{0})$.

$$M_N + E_0 = P_f^0 + E_e + E_{A'} \tag{2.39}$$

Considering the momentum of the photon in the sub-process, $k = P_i - P_f$, an expression for this, in terms of $x_{A'}$, is derived in [34] using that momentum squared is equal to the mass of the particle squared. The result is

$$k^0 = \frac{|\vec{k}|^2}{2M_N}, \quad |\vec{k}| = \frac{U}{2E_0(1-x_{A'})}. \tag{2.40}$$

Rewriting equation (2.39) using $|\vec{k}| = |\vec{P}_i - \vec{P}_f| = |\vec{P}_f|$ since the target is initially stationary, and $P_f^0 = \sqrt{M_N^2 + |\vec{P}_f|^2}$, one gets

$$\begin{aligned} M_N + E_0 &= \sqrt{M_N^2 + |\vec{k}|^2} + E_e + E_{A'} \\ \frac{M_N}{E_0} + 1 &= \frac{\sqrt{M_N^2 + |\vec{k}|^2(x_{A'})}}{E_0} + x_e + x_{A'}, \end{aligned} \tag{2.41}$$

dividing by E_0 in the last step. This equation can then be solved for $x_{A'}(x_e)$ to get the cross sections as a function of x_e. However, assuming, as they do in [34], that $|\vec{k}|^2 \ll M_N$ means that $\sqrt{M_N^2 + |\vec{k}|^2} \approx M_N$, i.e. the nucleus initial and final state energy is the same, and the equation becomes

$$x_{A'} = 1 - x_e \quad (\text{or } E_{A'} = E_0 - E_e). \tag{2.42}$$

The validity of this approximation is discussed in more detail in 4.2 where the WW is compared to the MG5 simulations and the nucleus energy distribution from MG5 is shown. What is concluded is that it seems to hold since the energy of the simulated nucleus is many orders lower than that of the electron and the DP. To get a distribution in the energy of the recoil electron one has to first integrate the θ dependency. This is done by integrating from the beam axis, $\theta = 0$ to a maximum angle, $\theta = \theta_M$, discussed more in section 4.2.

$$\frac{d\sigma}{dx_{A'}} = \int \frac{d\sigma^{\text{WW}}}{dx_{A'} d\cos\theta} d\cos\theta = \int_0^{\theta_M} \frac{d\sigma^{\text{WW}}}{dx_{A'} d\cos\theta}(x_{A'}, \theta) \sin\theta d\theta. \tag{2.43}$$

This then leaves only the $x_{A'}$ differential cross section and the assumption $x_{A'} = 1 - x_e$ can be utilised.

Furthermore, the transverse momentum of the electron is also interesting to consider and for this one has to change integration variables. Let $(x_{A'}, \cos\theta) \to (x_{A'}, p_T^{A'})$, where $p_T^{A'}$ is the transverse momentum of the DP given by

$$p_T^{A'}(x_{A'}, \theta) = |\vec{p}_{A'}| \sin\theta = E_0 \sqrt{x_{A'}^2 - \frac{m_{A'}^2}{E_0^2}} \sin\theta. \tag{2.44}$$

Where $|\vec{p}_{A'}| = \sqrt{E_{A'}^2 - m_{A'}^2}$ is the absolute value of the three-momentum of the DP. Using that $\sin\theta = +\sqrt{1 - \cos^2\theta}$ since we are in the region $\theta \in [0, \frac{\pi}{2}]$, due to that the angle is assumed to be small, implies that

$$\cos\theta = \sqrt{1 - \frac{p_T^{A'2}}{|\vec{p}_{A'}|^2}} \tag{2.45}$$

The integrand then becomes, utilising the absolute value of the determinant of the Jacobian to change variables

$$\begin{aligned} \sigma &= \int \frac{d\sigma}{dx_{A'} dcos\theta} dx_{A'} dcos\theta = \int \frac{d\sigma}{dx_{A'} dcos\theta}(x_{A'}, p_T^{A'}) \begin{vmatrix} \frac{\partial x_{A'}}{\partial x_{A'}} & \frac{\partial x_{A'}}{\partial p_T^{A'}} \\ \frac{\partial \cos\theta}{\partial x_{A'}} & \frac{\partial \cos\theta}{\partial p_T^{A'}} \end{vmatrix} dx_{A'} dp_T^{A'} \\ &= \left\{ \frac{\partial \cos\theta}{\partial x_{A'}} = 0 \right\} = \int \frac{d\sigma}{dx_{A'} dcos\theta}(x_{A'}, p_T^{A'}) \frac{p_T^{A'}}{|\vec{p}_{A'}|^2 \sqrt{1 - \frac{p_T^{A'2}}{|\vec{p}_{A'}|^2}}} dx_{A'} dp_T^{A'} \end{aligned} \tag{2.46}$$

This then yields the differential cross section with respect to $p_T^{A'}$ as

$$\frac{d\sigma}{dp_T^{A'}} = \int_{x_{A'}^{(1)}}^{x_{A'}^{(2)}} \frac{d\sigma}{dx_{A'}dcos\theta}(x_{A'}, p_T^{A'}) \frac{p_T^{A'}}{|\vec{p}_{A'}|^2\sqrt{1-\frac{p_T^{A'2}}{|\vec{p}_{A'}|^2}}} dx_{A'} \tag{2.47}$$

As for the energy the interesting quantity is that of the scattered electron, p_T^e. To get the cross section as a function of this it is assumed that the target does not move much in the transverse direction and that its transverse momentum is much lower than that of the electron and DP. Momentum conservation then requires that the electron transverse momentum becomes equal to the DP, i.e. $p_T^e \approx p_T^{A'}$. However, unlike the assumption made in the energy case, $|\vec{k}| \ll M_N$, this approximation does not seem as valid when comparing this WW approximation to the MG5 simulations of the recoiling electron and examining the nucleus p_T from MG5. What is found, in chapter 4.2 where it is discussed further, is that the p_T of the nucleus is of the same order of magnitude as that of the DP and recoil electron.

3

Cosmological Constraints

In this chapter the results of the calculated relic abundance of DM is presented. The calculations have been made for the model presented in chapter 2.1 and assuming complex scalar DM. A further restriction is that only the coupling to the electron is considered. This, combined with that the DM in the model only interacts with the SM through the DP mediator, means that the annihilation process for the DM is the s-channel one through the DP mediator to an electron and a positron, discussed in section 2.3. This simulation shows one way to further investigate the properties of the model and put limitations on the coupling constants for the different interactions and masses of the DM and the DP. Throughout the chapter the mass relation between the DP and the DM is assumed to be such that the DP is three times heavier than the DM, i.e. $m_{A'} = 3m_\chi$ in agreement with the benchmark calculations presented in [3]. Further, the coupling between the DP and the complex scalar DM is set to a fixed value given by $\alpha_{DM} = \frac{g_{DM}^2}{4\pi} = 0.5$ as a conservative benchmark, also in agreement with [3]. In section 3.1 the results of the relic density simulations for the different interactions, using micrOMEGAs, are presented. Following in section 3.2 is a calculation of the thermally averaged cross section times velocity made separate from micrOMEGAs to crosscheck the output. As discussed in section 2.4 when referring to the thermally averaged cross section times velocity the factor of $\frac{1}{2}$, accounting for that the DM considered is not its own antiparticle, is always included. In these simulations the varied parameters are the mass of the DM, which also then varies the DP mass, and the coupling constants to the DP. For KM this is done through the dimensionless quantity $y = \epsilon^2 \alpha_{DM} (\frac{m_\chi}{m_{A'}})^4$. The choice of y as a variable to vary is motivated by the use in [3], but as can be seen since α_{DM} and the mass ratio $\frac{m_\chi}{m_{A'}}$ are both fixed it effectively corresponds to the mixing parameter squared, $\propto \epsilon^2$. For the electromagnetic interactions the parameter under consideration is also related to the coupling constant squared, but through $\alpha_D = \frac{g_D^2}{4\pi}$ or $\alpha'_D = \frac{g_D'^2}{4\pi}$.

3.1 Relic Density Simulation

To be able to simulate the system the fields of the SM extended particles, A' and χ/χ^*, were implemented in FeynRules. To retrieve the physics and the couplings the interaction Lagrangians for both the DP coupled to the DM, given in equation (2.4), and the coupling between the DP and the SM electron/positron, given in

equation, (2.3), were also added. In addition to this the regular SM Lagrangian and particles are included in the simulations, to include the SM electron as an annihilation final state and a possible production initial state for the DM. This was then exported as a CalcHEP model file and used in micrOMEGAs. To obtain the relic density micrOMEGAs calculates the thermally averaged cross section and solves the Boltzmann equation in a similar fashion to what is discussed in section 2.4.

The line in the parameter space that corresponds to the observed relic density, $\Omega h^2 \approx 0.12$ [7], is shown in figure 3.1, where a very large parameter space for the electromagnetic interactions is considered, and 3.2, which zooms in on the electromagnetic interactions. This can then be used to put bounds on the coupling constant for different masses, since the model has to be able to produce the correct relic abundance. The total relic density that would be produced by all the different combinations of masses and coupling constants in the region is shown in figure 3.3. From this plot one can see how the relic density would evolve for a deviation from the parameters that yield the $\Omega h^2 = 0.12$ line. The thermally averaged cross section times velocity for a fixed typical mass to freeze-out temperature ratio of $x_f = 20$ is shown in figure 3.4. This is an important property in the calculation of the relic density and will be used in comparing the result from micrOMEGAs to one calculated outside the program in section 3.2. The figures have been made by calculating the relic density or thermally averaged cross section in a 50x50 grid for each model, even the zoomed in versions consist of a 50x50 grid of the stated parameter space consisting of DM masses and coupling constants between the electron and the DP.

In the plots of figure 3.1 and 3.2 one can see that there are at least two lines for all the interactions except for the KM. However, one can also note that the line in the top right corner corresponds to very large coupling constants, which would be excluded by unitarity bounds. These bounds are discussed in [35]. In the bottom left corner of the plots for the electromagnetic interactions there is some notable noise, but as seen in the colour plots this is most likely due to numerical inaccuracies in micrOMEGAs as there is a sharp cutoff. This could possibly be due to the fact that in these extreme parameter regions the freeze-out ratio $x_f = m\chi/T_f$ becomes very low and the program might have difficulties handling this. The low x_f value would arise since the coupling constants small and that would make the particles interact very feebly with the ones in the thermal bath and χ would therefore decouple faster, meaning at a higher temperature. One can also see that the noise is not present in the thermally averaged cross section times velocity plots. Possibly due to the fact that the freeze-out temperature here is fixed. The lines to focus on for the higher order electromagnetic couplings is therefore the ones in the middle of the graphs.

Staying in figure 3.1, for KM one sees that the slope is increasing from $y \approx 10^{-13}$ to $y \approx 10^{-7}$, when going between $m_\chi = 1\,\mathrm{MeV}$ to $m_\chi = 1\,\mathrm{GeV}$. Moving to the electromagnetic couplings one thing that is noticeable is the fact that the magnetic and electric dipole generate almost the same relic density. This also seems to be the case for charge and anapole interactions. In figure 3.2 one sees that for the magnetic

and electric dipole the relic density lies almost constant around $\alpha_D = 10^{-7}\,\mathrm{GeV}^{-2}$ for all masses, while for the charge and anapole interactions the line goes from around $\alpha'_D = 10^{-2}\,\mathrm{GeV}^{-4}$ to $\alpha'_D = 10^{-8}\,\mathrm{GeV}^{-4}$ as the DM masses increase. This means a downward slope in the coupling constants for charge and anapole in contrast to the KM whose coupling constant increases with increasing mass. These results then mean that for KM as the DP mass increases the coupling constant would have to increase as well to generate $\Omega h^2 = 0.12$ and the opposite is true for the charge and anapole interactions, while for the magnetic and electric dipole the coupling constant is as mentioned approximately constant and this would indicate that it does not have to change for increasing mass of the DP. Once again it is worth stating that only complex scalar DM with couplings through the DP to the SM electron and positron is considered here and that adding other annihilation channels through interactions with other particles and other types of DM would most likely shift the relic density curves. An annihilation channel to, for example, the SM muons would be expected as well due to their similarities with the electron.

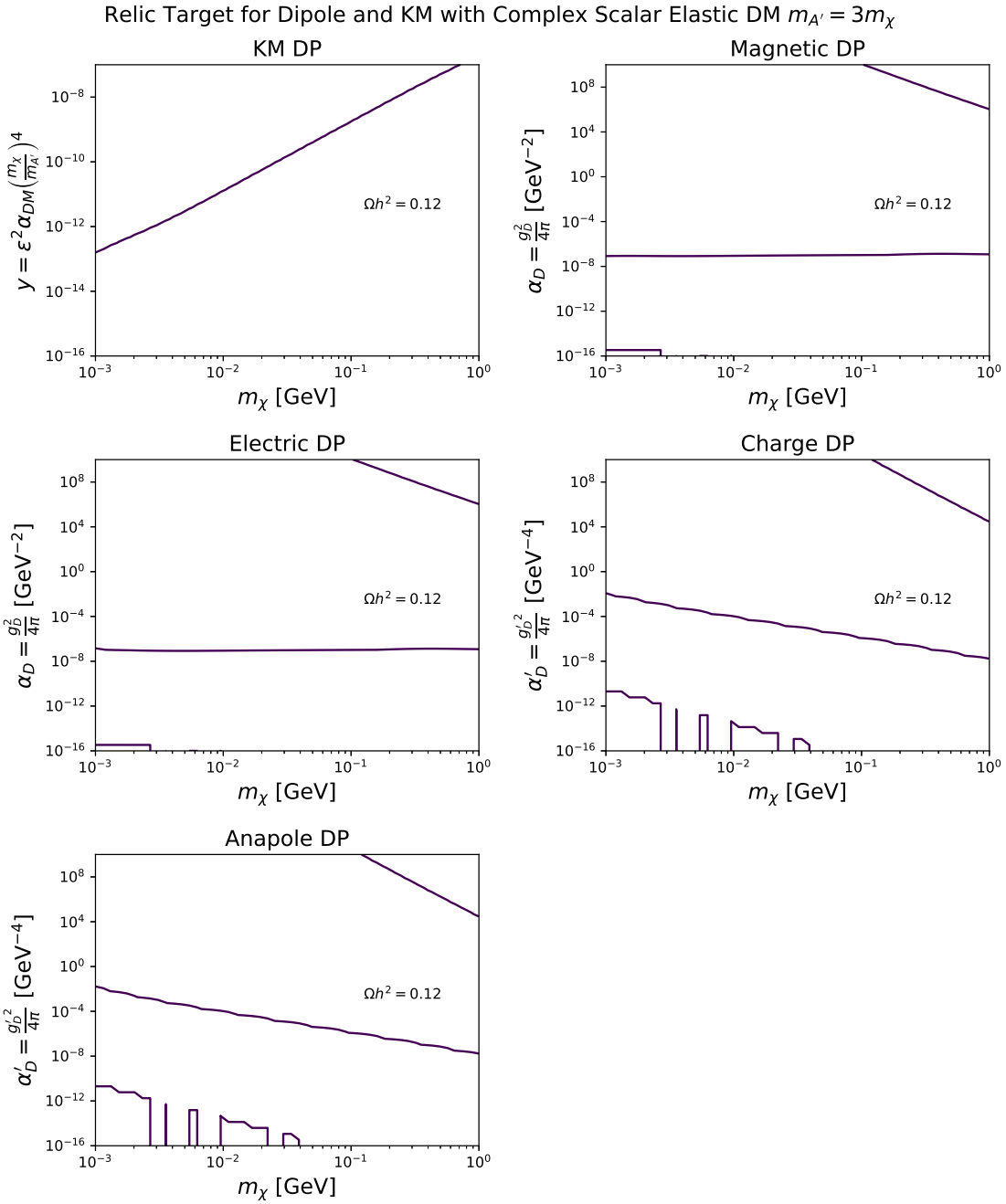

Figure 3.1: The line corresponding to the DM relic density of $\Omega h^2 = 0.12$, for the DP coupling to the electron and complex scalar DM. This has been plotted for masses $m_\chi = 1\,\text{MeV}$ to $m_\chi = 1\,\text{GeV}$ and coupling constants in the ranges $y = 10^{-16} - 10^{-7}$, $\alpha_D = 10^{-16} - 10^{10}\,\text{GeV}^{-2}$ and $\alpha'_D = 10^{-16} - 10^{10}\,\text{GeV}^{-4}$. The relation between the DM and the DP mass is $m_{A'} = 3m_\chi$. Also used is $\alpha_{DM} = 0.5$.

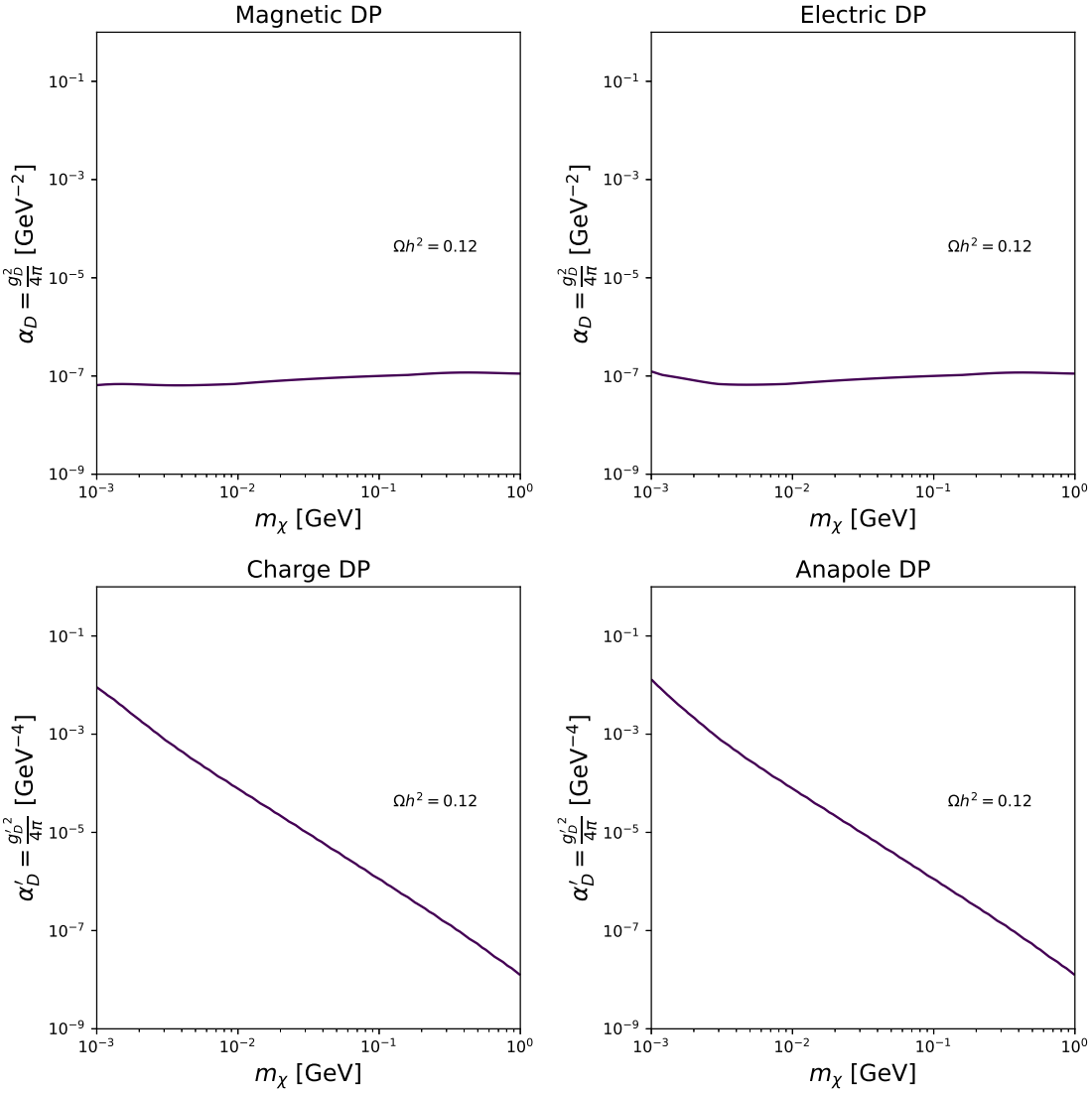

Figure 3.2: Zoomed in version of the line corresponding to the DM relic density of $\Omega h^2 = 0.12$, for the DP coupling to the electron and complex scalar DM, for all couplings but KM. This has been plotted for masses $m_\chi = 1\,\text{MeV}$ to $m_\chi = 1\,\text{GeV}$ and coupling constants in the ranges $\alpha_D = 10^{-9}{-}1\,\text{GeV}^{-2}$ and $\alpha'_D = 10^{-9}{-}1\,\text{GeV}^{-4}$. The relation between the DM and the DP mass is $m_{A'} = 3m_\chi$. Also used is $\alpha_{DM} = 0.5$.

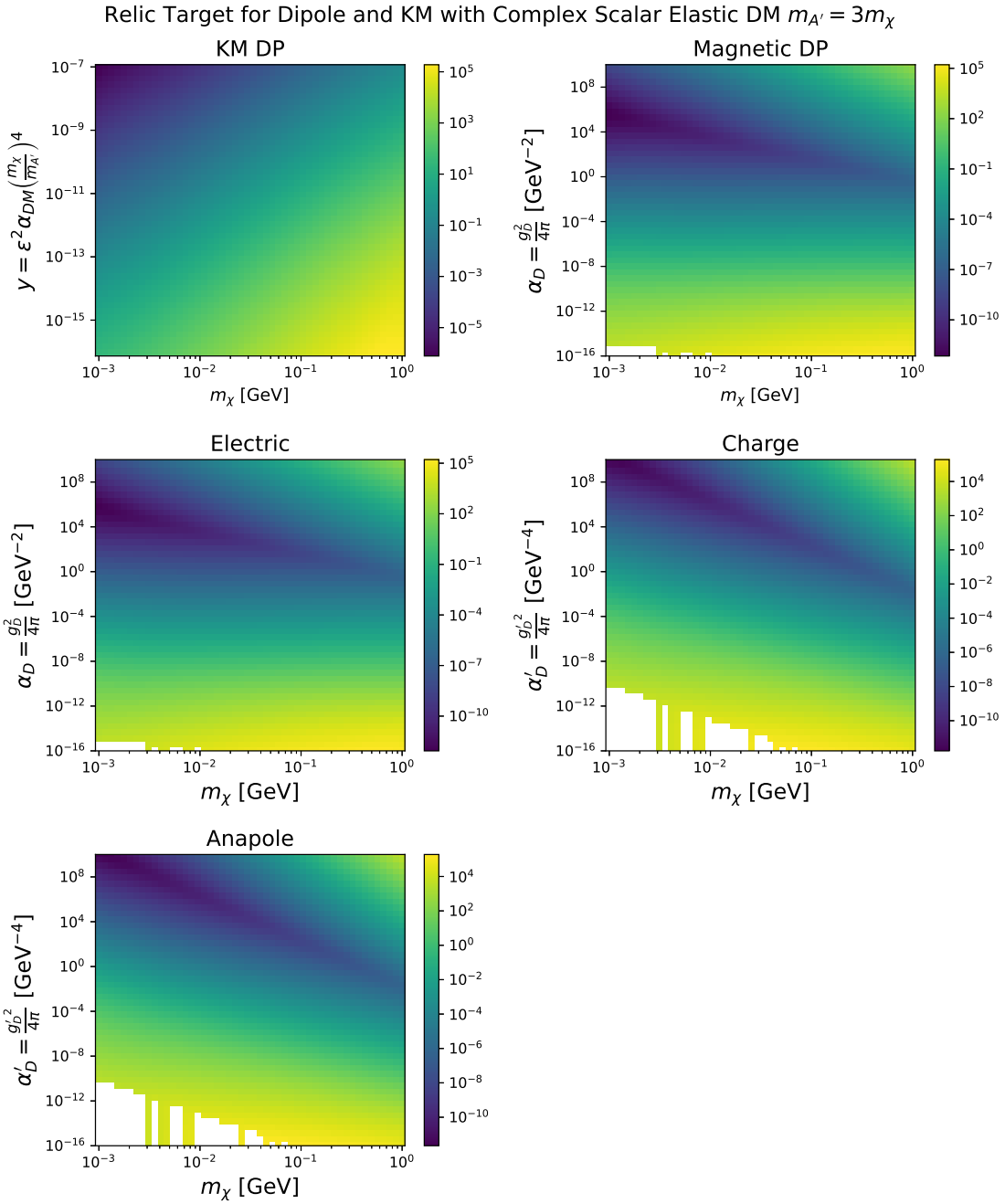

Figure 3.3: The total relic density for all the possible combinations of coupling constants and masses in the regions $y = 10^{-16} - 10^{-7}$, $\alpha_D = 10^{-16} - 10^{10}\,\mathrm{GeV}^{-2}$, $\alpha'_D = 10^{-16} - 10^{10}\,\mathrm{GeV}^{-4}$ and $m_\chi = 1\,\mathrm{MeV}$ to $m_\chi = 1\,\mathrm{GeV}$. The plots are for the coupling of the DP to the electron and complex scalar DM. The relation between the DM and the DP mass is $m_{A'} = 3m_\chi$. Also used is $\alpha_{DM} = 0.5$.

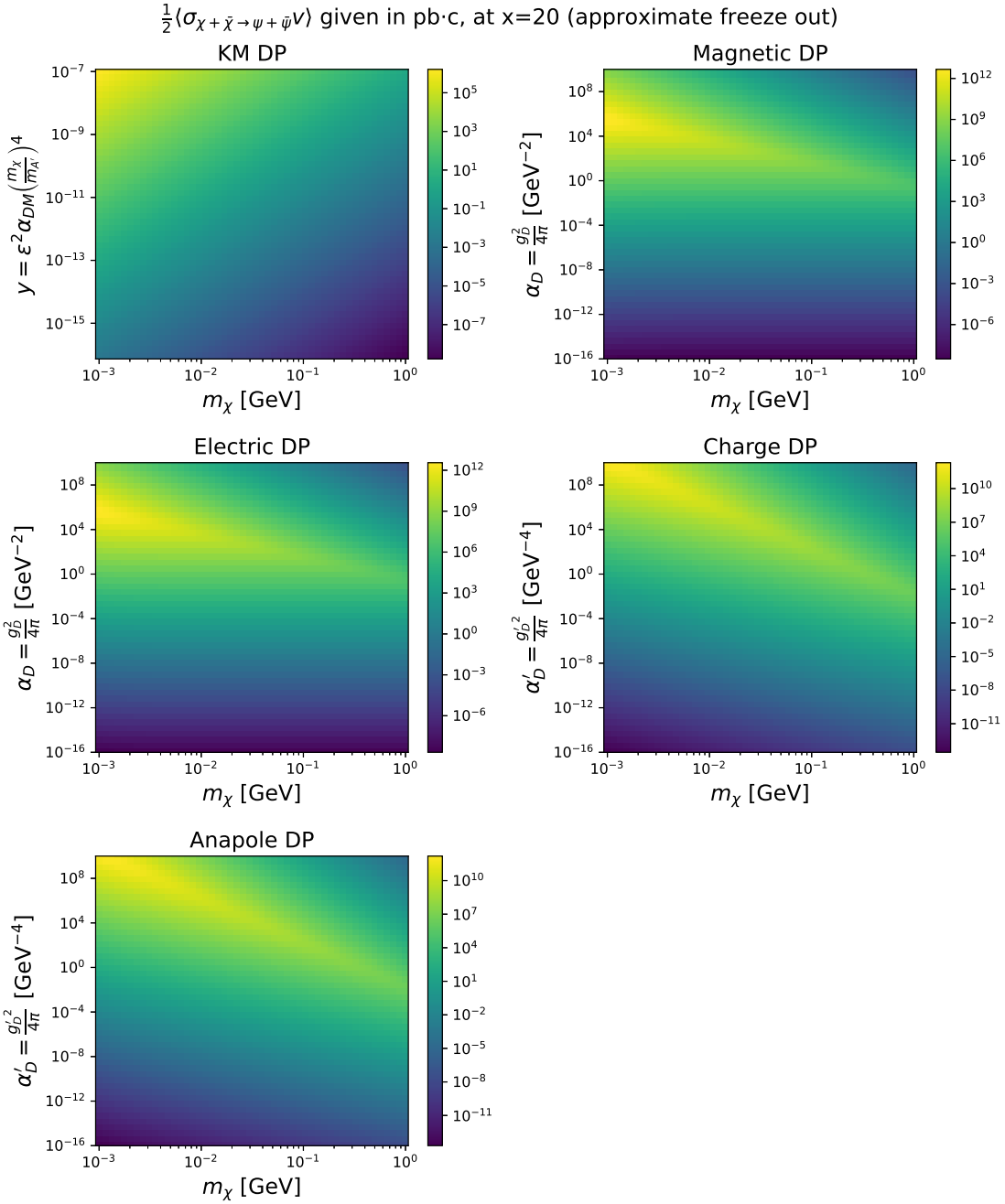

Figure 3.4: The thermally averaged cross section times velocity, for a fixed freeze-out mass to temperature ratio of $x_f = \frac{m_\chi}{T_f} = 20$ for all the possible combinations of coupling constants and masses in the region $m_\chi = 1\,\text{MeV}$ to $m_\chi = 1\,\text{GeV}$ and $y = 10^{-16} - 10^{-7}$, $\alpha_D = 10^{-16} - 10^{10}\,\text{GeV}^{-2}$ and $\alpha'_D = 10^{-16} - 10^{10}\,\text{GeV}^{-4}$. The plots are for the coupling of the DP to the electron and complex scalar DM. The relation between the DM and the DP mass is $m_{A'} = 3m_\chi$. Also used is $\alpha_{DM} = 0.5$.

3.2 Crosscheck of the Simulation Results

The fact that there was a bug in micrOMEGAs 6.0 that gave the wrong, and sometimes even negative, values of the relic densities for the simulated models when applying it to DM in the sub-GeV range, motivated the calculation of the thermally averaged cross section times velocity outside of the program. This was done to ensure that micrOMEGAs 5.2.13 gave reasonable results, and the calculations were performed following the theory presented by Gondolo and Gelmini [32].

To do this first note that the expression for the thermally averaged cross section times velocity $\frac{1}{2}\langle\sigma_{\chi\bar{\chi}\to\psi\bar{\psi}}v\rangle$, as presented in section 2.4, can be simplified further from equation (2.22) by describing the velocity in a reference frame where one of the incoming particles are stationary [32]. This is equivalent to the earlier description and it is given by [32] as

$$\begin{aligned}\frac{1}{2}\langle\sigma_{\chi+\bar{\chi}\to\psi+\bar{\psi}}v\rangle &= \int_0^\infty \frac{x}{K_2^2(x)}\sqrt{\epsilon}(1-2\epsilon)K_1(2x\sqrt{1+\epsilon})\sigma_{\chi+\bar{\chi}\to\psi+\bar{\psi}}v_{lab}d\epsilon,\\ \epsilon &= \frac{s^2-4m_\chi^2}{4m_\chi^2}.\end{aligned} \tag{3.1}$$

In the above expression K_1 and K_2 are as in equation (2.22), modified Bessel functions of the first and second order, and s is the invariant Mandelstam variable. Now focusing on the example at hand, namely the s-channel annihilation process of complex scalar DM to electrons and positrons, $\chi(p_1)\chi^*(p_2)\to e^-(k_1)e^+(k_2)$, as described in section 2.3. The masses of both initial state particles are equal, m_χ, and the same applies to the final state particles, m_e. This makes it possible to describe $\sigma_{\chi\chi^*\to e^-e^+}v_{lab}$ by the following expression [32]

$$\sigma_{\chi\chi^*\to e^-e^+}v_{lab} = \frac{1}{64\pi^2(s-2m_\chi^2)}\frac{|\vec{k}|}{E}\int\overline{|M|^2}^{\mathrm{CM}}d\Omega, \tag{3.2}$$

where the $\overline{|M|^2}^{\mathrm{CM}}$ is the squared matrix element averaged over initial state spins and summed over final state ones in the CM frame, and the integral is over the CM solid angle, $d\Omega$, of the outgoing electron. Here it is clear that one can advantageously use the matrix elements calculated in section 2.3 to obtain σv_{lab}. The $\frac{|\vec{k}|}{E}$ is the absolute value of the outgoing electron, or positron, CM three-momentum (which is shared since they have the same mass) divided by the energy of the particle. The energy is half the CM energy. For clarity see figure 2.3 for the definitions of momentum and energy. Since the matrix elements are given in terms of the CM three-momentum and $E = E_{CM}/2$ a variable change from ϵ to E in equation 3.1 is motivated. Using that $s = 4E^2$ the resulting integral is

$$\begin{aligned}\frac{1}{2}\langle\sigma_{\chi\chi^*\to e^-e^+}v\rangle = \int_m^\infty dE\frac{2E}{m^2}\frac{x}{K_2^2(x)}\sqrt{\epsilon(E)}(1-2\epsilon(E))\times\\ \times K_1(2x\sqrt{1+\epsilon(E)})\sigma_{\chi+\bar{\chi}\to\psi+\bar{\psi}}v_{lab}.\end{aligned} \tag{3.3}$$

Knowing that the three-momentum relates to the energy and mass the integral can be evaluated and compared to that of micrOMEGAs. This has been done for a 50x50 grid with the same bounds on the coupling constants and masses of the DP as for micrOMEGAs, see section 3.1, and the plot for the thermally averaged cross section simulated following the Gondolo and Gelmini procedure is given in figure 3.5. In the figure one can see that the resemblance to figure 3.4 produced with micrOMEGAs is immense. In the tables 3.1, 3.2 and 3.3 some values from the plots are shown to see roughly how close the micrOMEGAs simulation is compared to this one. In the tables one notes that they indeed are rather close. For KM, which seems to deviate the most, the outputs differ by only about $\sim 7\,\%$ and for some of the other couplings and values this shrinks down to $\sim 0.35\,\%$. These crosschecks imply that the values from micrOMEGAs version 5.2.13 are reasonable and can most likely be trusted even for the sub-GeV DM case. This was not the case for micrOMEGAs 6.0.

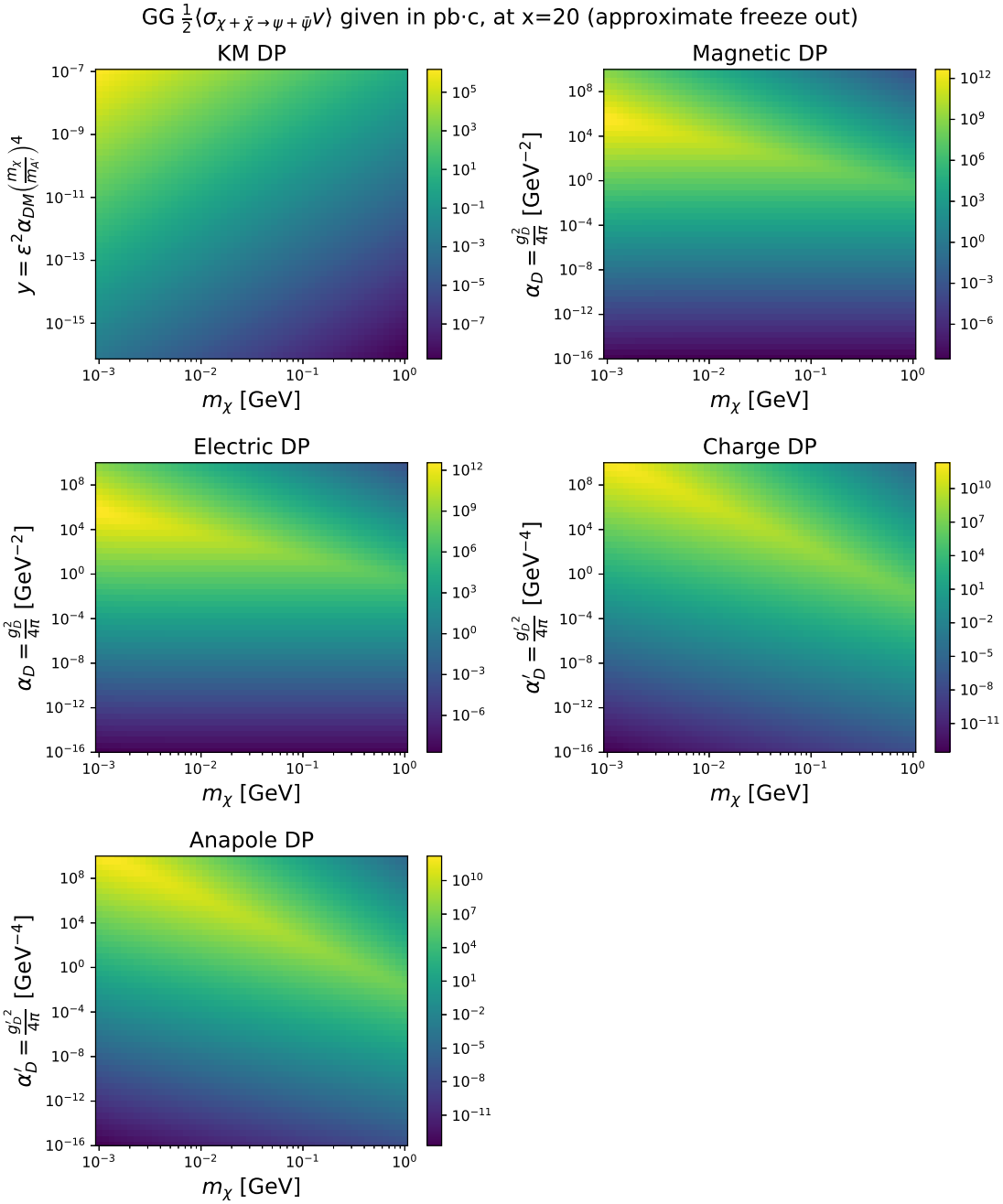

Figure 3.5: The thermally averaged cross section times velocity from following the theory in the paper by Gondolo and Gelmini [32], GG, for a fixed mass temperature ratio of $x = 20$. The mass and coupling constant ranges are the same as for the micrOMEGAs simulation in section 3.1. Also here the relation between the DM and DP mass is $m_{A'} = 3m_\chi$ and $\alpha_{DM} = 0.5$.

Table 3.1: Comparison of $\frac{1}{2}\langle\sigma_{\chi+\bar{\chi}\to\psi+\bar{\psi}}v\rangle$ between the micrOMEGAs values, MO, and the method following Gondolo and Gelmini [32], GG, to crosscheck. Values calculated with coupling constants $y = 10^{-15}$, $\alpha_D = 10^{-15}\,\mathrm{GeV}^{-2}$ and $\alpha'_D = 10^{-15}\,\mathrm{GeV}^{-4}$.

m_χ [GeV]		0.1	0.3	0.5	0.7	1
KM $\frac{1}{2}\langle\sigma v\rangle$ [pb·c]	GG	1.521e-02	1.726e-03	1.554e-04	1.553e-06	1.554e-08
	MO	1.632e-02	1.852e-03	1.667e-04	1.667e-06	1.667e-08
Magnetic $\frac{1}{2}\langle\sigma v\rangle$ [pb·c]	GG	3.899e-08	3.168e-08	3.066e-08	3.057e-08	3.056e-08
	MO	3.908e-08	3.177e-08	3.075e-08	3.065e-08	3.065e-08
Electric $\frac{1}{2}\langle\sigma v\rangle$ [pb·c]	GG	2.088e-08	2.942e-08	3.046e-08	3.057e-08	3.056e-08
	MO	2.094e-08	2.951e-08	3.054e-08	3.064e-08	3.065e-08
Charge $\frac{1}{2}\langle\sigma v\rangle$ [pb·c]	GG	2.665e-13	2.581e-12	2.870e-11	2.720e-09	2.870e-07
	MO	2.820e-13	2.592e-12	2.881e-11	2.881e-09	2.881e-07
Anapole $\frac{1}{2}\langle\sigma v\rangle$ [pb·c]	GG	1.874e-13	2.487e-12	2.861e-11	2.719e-09	2.870e-07
	MO	1.980e-13	2.497e-12	2.871e-11	2.881e-09	2.881e-07

Table 3.2: Comparison of $\frac{1}{2}\langle\sigma_{\chi+\bar{\chi}\to\psi+\bar{\psi}}v\rangle$ between the micrOMEGAs values, MO, and the method following Gondolo and Gelmini [32], GG, to crosscheck. Values calculated with coupling constants $y = 10^{-11}$, $\alpha_D = 10^{-8}\,\mathrm{GeV}^{-2}$ and $\alpha'_D = 10^{-8}\,\mathrm{GeV}^{-4}$.

m_χ [GeV]		0.1	0.3	0.5	0.7	1
KM $\frac{1}{2}\langle\sigma v\rangle$ [pb·c]	GG	1.521e+02	1.726e+01	1.554e+00	1.554e-02	1.554e-04
	MO	1.632e+02	1.852e+01	1.667e+00	1.667e-02	1.667e-04
Magnetic $\frac{1}{2}\langle\sigma v\rangle$ [pb·c]	GG	3.898e-01	3.168e-01	3.066e-01	3.056e-01	3.056e-01
	MO	3.908e-01	3.177e-01	3.075e-01	3.065e-01	3.065e-01
Electric $\frac{1}{2}\langle\sigma v\rangle$ [pb·c]	GG	2.087e-01	2.942e-01	3.046e-01	3.056e-01	3.056e-01
	MO	2.094e-01	2.951e-01	3.054e-01	3.064e-01	3.065e-01
Charge $\frac{1}{2}\langle\sigma v\rangle$ [pb·c]	GG	2.810e-06	2.583e-05	2.870e-04	2.870e-02	2.870e+00
	MO	2.822e-06	2.592e-05	2.881e-04	2.881e-02	2.881e+00
Anapole $\frac{1}{2}\langle\sigma v\rangle$ [pb·c]	GG	1.967e-06	2.488e-05	2.861e-04	2.870e-02	2.870e+00
	MO	1.977e-06	2.497e-05	2.871e-04	2.881e-02	2.881e+00

Table 3.3: Comparison of $\frac{1}{2}\langle\sigma_{\chi+\bar{\chi}\to\psi+\bar{\psi}}v\rangle$ between the micrOMEGAs values, MO, and the method following Gondolo and Gelmini [32], GG, to crosscheck. Values calculated with coupling constants $y = 10^{-8}$, $\alpha_D = 1\,\mathrm{GeV}^{-2}$ and $\alpha'_D = 1\,\mathrm{GeV}^{-4}$.

m_χ [GeV]		0.1	0.3	0.5	0.7	1
KM $\frac{1}{2}\langle\sigma v\rangle$ [pb·c]	GG	1.521e+05	1.726e+04	1.554e+03	1.554e+01	1.554e-01
	MO	1.632e+05	1.852e+04	1.667e+03	1.667e+01	1.667e-01
Magnetic $\frac{1}{2}\langle\sigma v\rangle$ [pb·c]	GG	3.898e+07	3.168e+07	3.066e+07	3.044e+07	2.789e+06
	MO	3.908e+07	3.177e+07	3.075e+07	3.065e+07	2.785e+06
Electric $\frac{1}{2}\langle\sigma v\rangle$ [pb·c]	GG	2.087e+07	2.942e+07	3.046e+07	3.044e+07	2.789e+06
	MO	2.094e+07	2.951e+07	3.054e+07	3.064e+07	2.785e+06
Charge $\frac{1}{2}\langle\sigma v\rangle$ [pb·c]	GG	2.812e+02	2.583e+03	2.870e+04	2.868e+06	8.929e+04
	MO	2.822e+02	2.592e+03	2.881e+04	2.881e+06	8.924e+04
Anapole $\frac{1}{2}\langle\sigma v\rangle$ [pb·c]	GG	1.969e+02	2.488e+03	2.861e+04	2.868e+06	8.929e+04
	MO	1.977e+02	2.497e+03	2.871e+04	2.881e+06	8.924e+04

4

Higher Order Electromagnetic Moments in the LDMX Framework

In this chapter the energy and transverse momentum distributions for the different electromagnetic interactions and KM, simulated with MG5, are shown and compared. For each interaction the mass of the DP is also varied in the sub-GeV region. After this a comparison with the WW approximation covered in section 2.5 is made for the case of $m_{A'} = 0.1\,\text{GeV}$ interacting through the KM or magnetic dipole interaction. For all the MG5 simulations there is a rapidity cut for the maximum angle of the recoil electron and the tungsten nucleus of $\eta = 0$ which means an angle of 90° from the beam axis. This is motivated by the fact that the LDMX does not measure backward scattering electrons [3]. There is in the MG5 simulations no cut applied for the minimum energy or p_T. Further, no cuts have been made for the DP since this is not being detected and therefore is not limited by the angles that the detector can measure. All the simulations utilise the coupling constants $y = 10^{-7}, \alpha_D = 10^{-7}$ or $\alpha'_D = 10^{-7}$. The scale of these are motivated by the relic density, but as seen in figure 3.1 the relic density is not constant for all masses. However, this is not an issue for the results in the coming analysis since the coupling constants only provide a constant factor to the overall cross section that is calculated. The reason for this is that the number of events is fixed to the same number for the compared simulations and the interactions are not mixed, but considered in isolation. The overall factor has no impact on the kinematics of the particles in the process and therefore does not impact the energy and transverse momentum diagrams. In all the simulations the tungsten nucleus is modelled as a heavy fermion with a mass of 171 GeV and to achieve the nucleus behaviour there are form factors added to compensate for the fact that the nucleus is not a point particle. Further, an electron beam energy of $E_0 = 4\,\text{GeV}$ is used since this is the planned energy for the LDMX [3] as described in section 1.4.

4.1 Energy and Transverse Momentum Distributions for Different Interactions and Masses

Below follows energy and transverse momentum distributions for the recoiling electron generated in MG5. As for the relic density simulations, considered in chapter 3, the first step in generating these was to implement the DP, A', in FeynRules. Also to describe the interactions the Lagrangian given in equation (2.3), for the couplings between the A' and the SM electron was implemented. Additionally in these simulations the full SM Lagrangian was added to keep the regular physics and generate the particles needed, in this case the electron and photon. The complex scalar DM χ is also implemented through the Lagrangian in equation (2.4), but since decays of the DP are not considered this has no effect on the simulations made. What differs in the case of the MG5 simulations, compared to the relic density ones, is that also the nucleus of the tungsten target has to be included. After implementing everything needed the simulations of the bremsstrahlung process, as described in section 2.2, $e^- N_W \to e^- N_W A'$, where N_W symbolises the target tungsten nucleus, could be carried out. For all the simulations in this section a number of generated events of 50 000 has been used, meaning that the simulation "creates" 50 000 DP:s. In the following figures the energy distributions are plotted in bins of 50 MeV and the p_T distributions have 10 MeV bins. The distributions are also normalised so that their respective integrals are equal to one.

In figures 4.1 and 4.2 the different interactions are plotted against each other for a, in each plot, fixed mass of the DP in the range $m_{A'} = 0.1 - 1\,\text{GeV}$. From these plots one can note that the KM, charge and anapole parts of the model align rather closely with each other. The same can be seen for the magnetic and electric dipole moments. This seems to be the case for both the energy and transverse momentum. A consequence of this alignment could be that the different interactions could be harder to differentiate and in an experiment match to the correct model. Another thing to consider is the fact that as the mass of the DP grows the different interactions seem to approach each other, which also could make them harder to distinguish. A common feature for all masses is that the magnetic dipole and electric dipole interactions seem to generate more electrons of higher energy due to their distributions being flatter and lying above the ones of the other interactions. This feature does seem to decrease when the mass increases but it is still there even at $m_{A'} = 1\,\text{GeV}$.

In figure 4.3 and 4.4 each of the interactions is plotted against themselves but for different masses, also here, in the range $m_{A'} = 0.1 - 1\,\text{GeV}$. It is clear from these plots that the energy of the recoiling electron tends to be larger for the lighter DP masses, since there are more events in the higher region of the energy distributions. One reason is that the DP when it is heavier takes more energy just to be created. For the p_T the opposite is seen, as the mass of the DP increases the p_T of the recoiling electron also does for all models.

Following, in figures 4.5, 4.6 and 4.7 different interactions and different masses have

been overlapped for comparison of how differentiable they are. These specific simulations have been chosen to show different cases of curves that are similar. Here one can see that in figure 4.5, where the KM interaction for a DP mass of $m_{A'} = 1\,\text{GeV}$ is compared to the magnetic dipole interaction with $m_{A'} = 0.7\,\text{GeV}$, the energy distributions are very similar and this can also be seen in the ratio of the number of events that is close to 1, except for the upper regions where the number of events are lower. This could indicate that these two would be more difficult to differentiate, but what could balance that is that the p_T distribution is a lot more different for the models in most regions of the distribution. Moving to figure 4.6, where the charge and anapole interactions have been compared for the same mass $m_{A'} = 0.5\,\text{GeV}$, it is noticeable that they are extremely close for both distributions which could prove very difficult to differentiate in an experiment. Finally in figure 4.7, which shows the magnetic dipole interaction for $m_{A'} = 0.3\,\text{GeV}$ and the charge interaction for $m_{A'} = 0.1\,\text{GeV}$, one can see that the energy distributions overlap in the early and middle parts of the distributions where there are a lot of events but deviate at the larger energies. This could mean that they could be harder to differentiate if the detector is most sensitive to the middle regions of the spectrum, however as for figure 4.5 the p_T distribution here also deviates a lot which could help in decoding which interaction has been observed.

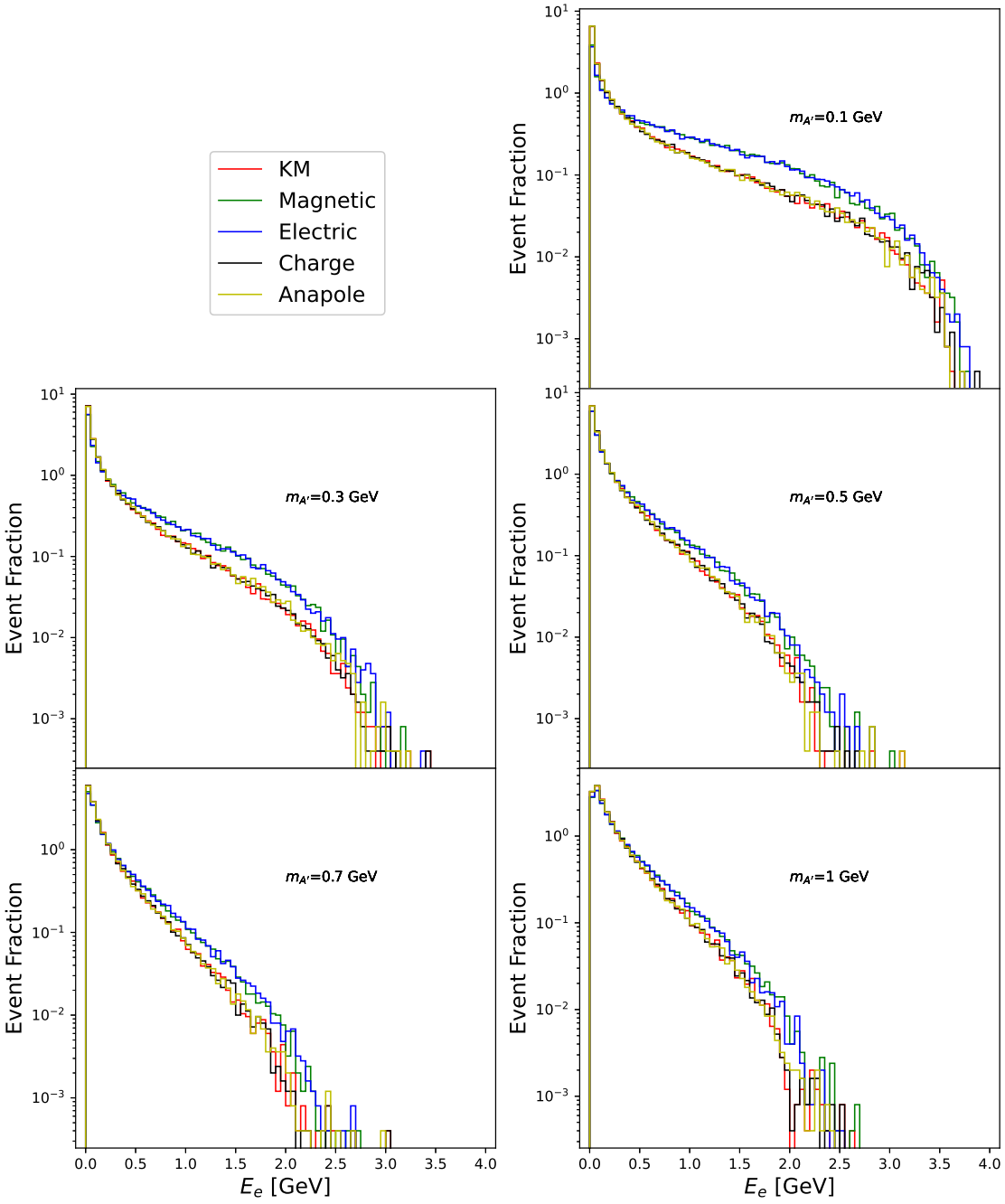

Figure 4.1: Energy distributions comparing the different interactions against each other for a fixed DP mass, $m_{A'} = 0.1, 0.3, 0.5, 0.7$ or $1\,\text{GeV}$, in each plot. The different interactions are KM, magnetic and electric dipole, charge and anapole.

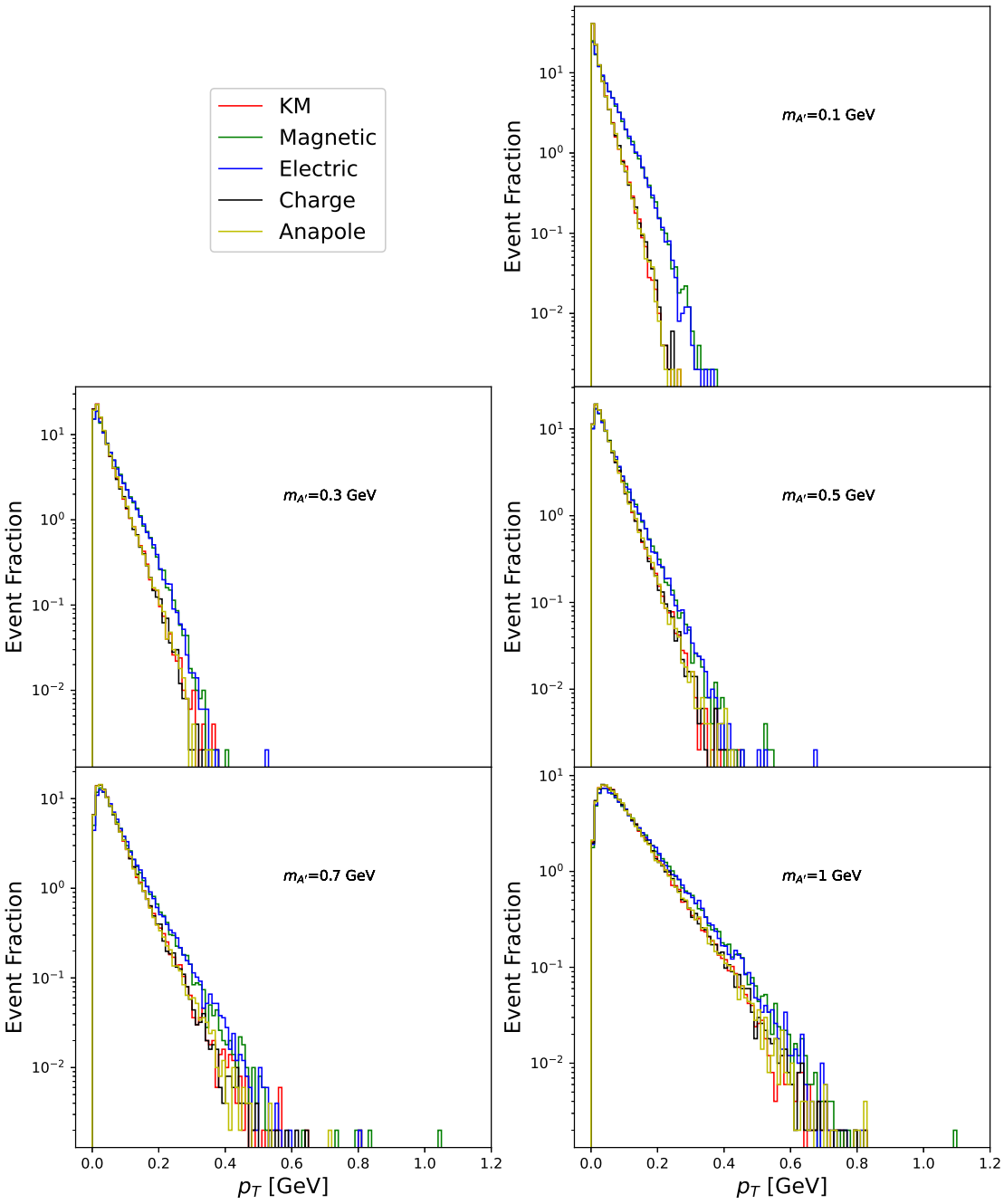

Figure 4.2: Transverse momentum distributions comparing the different interactions against each other for a fixed DP mass, $m_{A'} = 0.1, 0.3, 0.5, 0.7$ or $1\,\text{GeV}$, in each plot. The different interactions are KM, magnetic and electric dipole, charge and anapole.

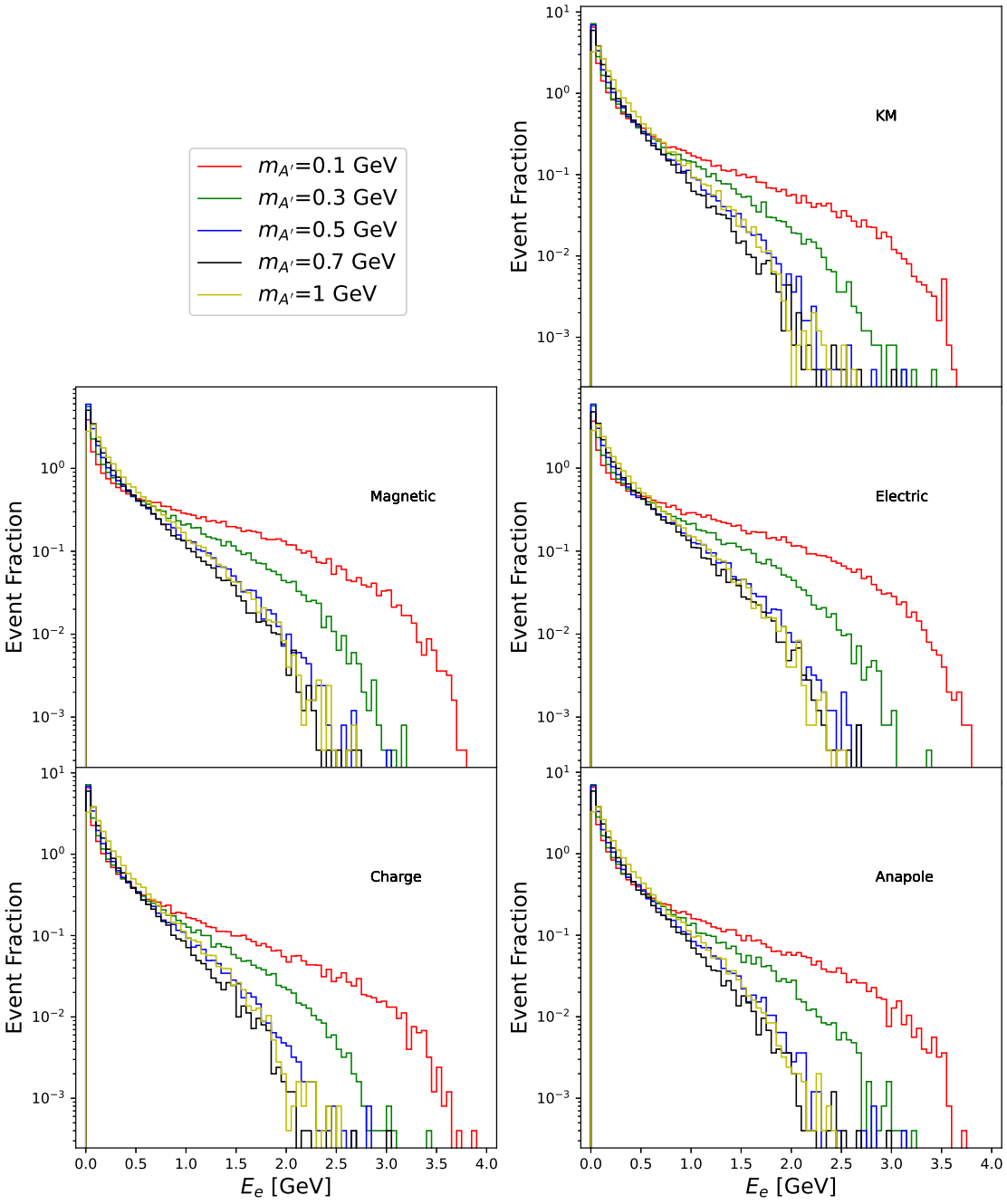

Figure 4.3: Energy distributions comparing different DP masses for each interaction, KM, magnetic or electric dipole, charge or anapole, separately. The different masses are $m_{A'} = 0.1, 0.3, 0.5, 0.7$ and $1\,\text{GeV}$.

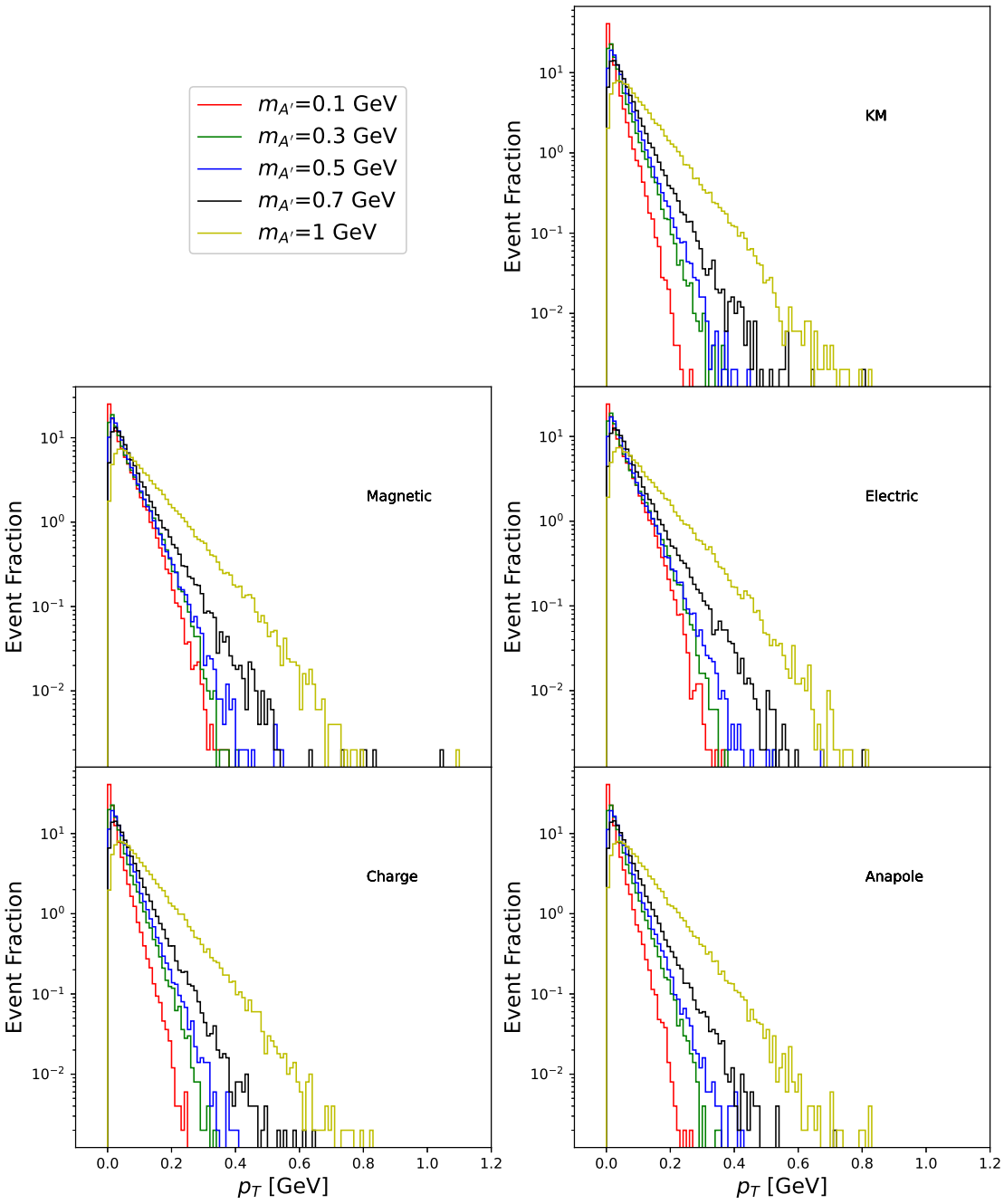

Figure 4.4: Transverse momentum distributions comparing different DP masses for each interaction, KM, magnetic or electric dipole, charge or anapole, separately. The different masses are $m_{A'} = 0.1, 0.3, 0.5, 0.7$ and $1\,\text{GeV}$.

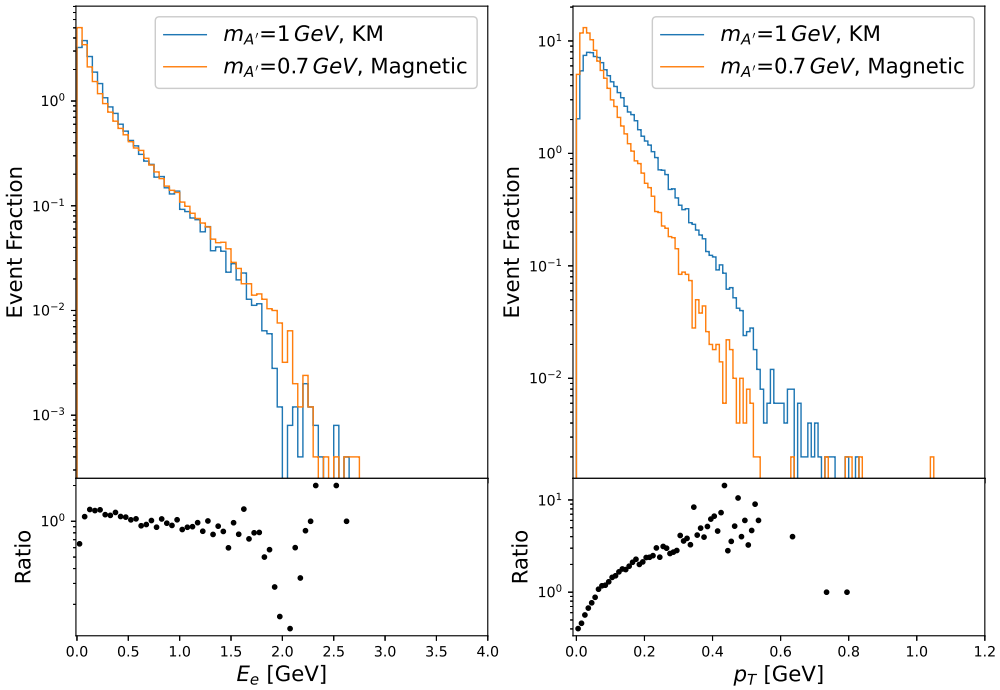

Figure 4.5: Ratio comparison of the energy distribution and transverse momentum of the scattering electron. Comparing KM interaction with $m_{A'} = 1\,\text{GeV}$ to magnetic dipole interaction with $m_{A'} = 0.7\,\text{GeV}$.

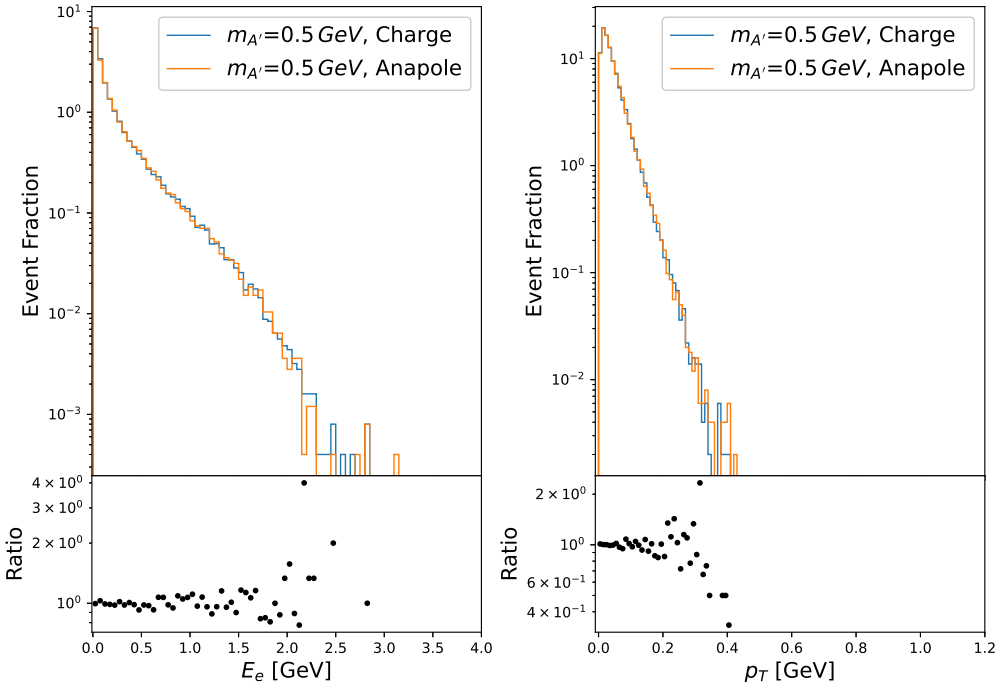

Figure 4.6: Ratio comparison of the energy distribution and transverse momentum of the scattering electron. Comparing charge interaction with $m_{A'} = 0.5\,\text{GeV}$ to anapole interaction with $m_{A'} = 0.5\,\text{GeV}$.

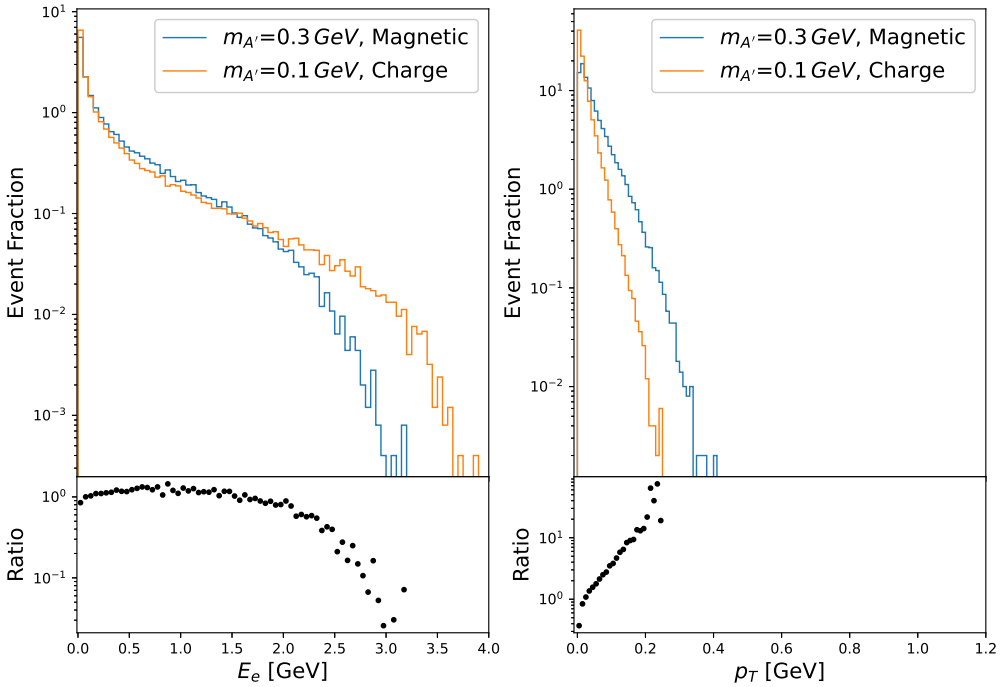

Figure 4.7: Ratio comparison of the energy distribution and transverse momentum of the scattering electron. Comparing magnetic dipole interaction with $m_{A'} = 0.3\,\text{GeV}$ to charge interaction with $m_{A'} = 0.1\,\text{GeV}$.

4.2 Comparison to the Weizsäcker-Williams Approximation

In this section the energy and transverse momentum distributions of the recoiling electron generated by MG5, simulating the electron collision in a LDMX like framework, are compared to the analytical WW approximation. These have been generated from the differential WW cross sections in equations (2.37) derived in [34] and (2.38) derived in [4], discussed in section 2.5. The results are shown in figure 4.8 and 4.9. The assumed constant prefactors, A and B, of the differential cross sections are set equal to one. For the energy distribution the normalisation is later established by imposing that the integral of the distribution over the space is one. The same normalisation is made for the MG5 distributions. For the transverse momentum the normalisation is such that the first bin aligns with that of the MG5 simulation since they, as will be seen, differ a lot.

The energy distributions of the recoiling electrons are acquired from the WW approximation by first integrating away the DP angle, θ, dependency of the differential cross sections. This is here done for four different maximum angles $\theta_M = 0.004, 0.087, 0.5$ and $\frac{\pi}{2}$ rad. After this one utilises the change of variables $x_{A'} = 1 - x_e$, when integrating the energy ratio differential cross section, $\frac{d\sigma}{dx_{A'}}$, given in equation 2.43, to get the energy distribution of the recoil electron and not the DP. This integral is

evaluated by sampling bins of $\delta E = 50\,\text{MeV}$ with 1000 points each and integrated over each bin to generate an energy distribution. For bin i this is described by

$$\sigma_i^{\text{WW}} = \int \frac{d\sigma^{\text{WW}}}{dx_{A'}} dx_{A'} = \int_{E_e[i]/E_0}^{(E_e[i]+\delta E)/E_0} \frac{d\sigma^{\text{WW}}}{dx_{A'}}(x_e) dx_e. \tag{4.1}$$

In the above expression the sign from the change of variables is absorbed into the integral by swapping integration limits. This can be done since $0 < x < 1$ which means that $x_e^i = 1 - x_{A'}^i > 1 - x_{A'} = x_e^f$, where $x_e^{i/f}$ are theoretical lower/upper bounds for the electron energy ratio.

The numerical integration of the angle and energy is then repeated for both the interactions, KM and magnetic dipole cross sections from equations (2.37) and (2.38), and each σ_i is then plotted over the respective bin and can be seen in figure 4.8, where it is compared to the MG5 output. The bins are as mentioned 50 MeV in size, and they range from a cutoff at $E_e = 50\,\text{MeV}$ to the maximum possible energy, where the DP has zero three-momentum, i.e. it stands still, $E_e = E_0 - m_{A'}$. The MG5 simulations are here made with 100 000 events and there has been no cut applied to the energy, but they are also plotted from 50 MeV to $E_e = E_0 - m_{A'}$, which means that there is a cut of 50 MeV made in the plotting so that not all of the 100 000 events are included in the plots. However, this does not pose an issue since both the WW approximation and the MG5 are normalised in the same way, and 100 000 events are more than enough to show the behaviour of the interactions, even without the events in the first 50 MeV bin. Other than this the same rapidity cut as described at the start of this chapter, 4, is applied. The motivation for the cut at $E_e = 50\,\text{MeV}$ is due to the lack of detectability in that region. This is in agreement with [3]. The integral of the MG5 data is then normalised to have an integral equal to 1, and the WW approximation is also normalised in this way so that the integral of the different plots is the same.

In the figure different maximal θ_M are presented and compared. As can be seen the angle of about $5° \approx 0.087\,\text{rad}$ is the one that matches the best to the MG5 output. This is reasonable since for a too small θ_M in the WW approximation, for example 0.004 rad, one only accounts for very close to the beam scattering, and misses ones that scatter further from the beam. Also the larger angles presented are further from the MG5 output, see for example $\theta_M = 0.5$ and $\theta_M = \pi/2$. This could be due to more A' scattering at sharper angles in the MG5 simulations, which will be treated as doing no approximation to the process, and therefore the WW here overcounts the number of A' since it possibly accounts for some scattering at larger angles. However, in all the plots no matter what θ_M one picks a common trait that is shared between both the MG5 simulations and the WW approximation is that the magnetic dipole interactions distribution is flatter, meaning it produces more electrons with larger energy, than the KM one. This is something that differs from [4]. Though supported by the MG5 simulations, the behaviour of the magnetic dipole interaction in comparison to the KM interaction most likely is as stated in this thesis.

Looking at the left figure in 4.10 one can note that the assumption of $x_{A'} = 1 - x_e$

is valid due to the fact that it comes from approximating the energy of the final state nucleus, E_W^f, to be equal to the initial state energy i.e. the nucleus mass, $M_N = 171\,\text{GeV}$. From the figure it is clear that this is the case since at most in some extreme cases, many orders of magnitude lower in occurrence, $|E_W^f - M_N|$ is only a few thousands of a GeV which is three orders of magnitude lower than that of the electron energy distribution if one looks at the MG5 curves of figure 4.8. This is true also compared to the DP energy distribution shown to the left in figure 4.11 which has the same order of magnitude as the electrons' distribution.

Moving on to the electron transverse momentum, p_T^e, one first completes the integral over the DP energy in equation (2.47) with the boundaries $x_{A'}^{(1)} = \sqrt{\frac{{p_T^{A'}}^2}{E_0^2} + \frac{m_{A'}^2}{E_0^2}}$, given by the fact that $p_T^{A'} \leq |\vec{p}_{A'}|$, and $x_{A'}^{(2)} = 1 - \frac{m_{A'}}{E_0}$, which is the maximum possible and is the same as saying that the DP is stationary at emission. The p_T^e is then gotten by making a change of variables, utilising the approximation $p_T^e \approx p_T^{A'}$, and then integrating the transverse momentum differential cross section in bins of $\delta p_T^e = 10\,\text{MeV}$. In the same way as for the energy each bin, i, is given by

$$\sigma_i^{\text{WW}} = \int \frac{d\sigma}{dp_T^{A'}} dp_T^{A'} = \int_{p_T^e[i]}^{p_T^e[i]+\delta p_T^{A'}} \frac{d\sigma}{dp_T^{A'}}(p_T^e) dp_T^e. \tag{4.2}$$

The result is shown in figure 4.9 where the bin range is $p_T^e = 0 - 1.2\,\text{GeV}$. Here there is no limit in the lower end of the p_T spectra, as all the momentum could be along the beam axis , and the upper limit is set by the fact that it should be comparable with the MG5 simulations which have a much sharper decline. The MG5 data has been normalised so that the integral is one. As one can see from the figure the WW approximation for the transverse momentum differs a lot from that of the MG5 simulation. For this reason the way MG5 and the WW data have been overlapped is by letting the first bin of each interaction of WW be equal to that of the MG5 to compare since normalising to the same integral would not show the features. One reason for this extreme difference could be the fact that the assumption of $p_T^e \approx p_T^{A'}$ does not seem to hold. This is because the nucleus seems to have non-negligible p_T which can be seen to the right in figure 4.10. In the figure the p_T of the nucleus is shown and even though it, in general, is smaller than that of the electrons in the MG5 plots of figure 4.9, and the p_T of the DP shown to the right in figure 4.11, it is still the same order of magnitude. This means that the assumption of negligible nucleus p_T does not hold, unlike the energy case.

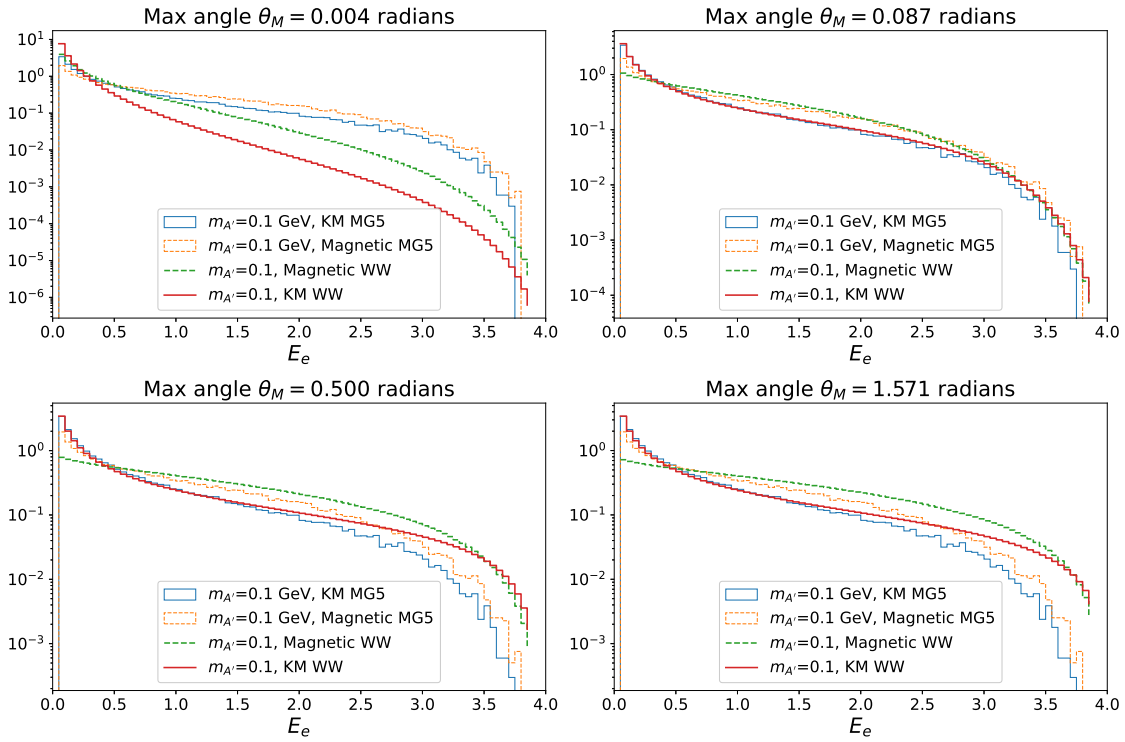

Figure 4.8: The energy distribution of the recoiling electron in the WW approximation plotted against the MG5 simulations for the KM and magnetic dipole interactions and a DP mass of $m_{A'} = 0.1\,\text{GeV}$. In the figure different maximum angles, θ_M, are shown. They are plotted in bins of 50 MeV from a cutoff at $E_e = 50\,\text{MeV}$ to a maximally possible $E_e = E_0 - m_{A'}$, i.e. a DP without any three-momentum.

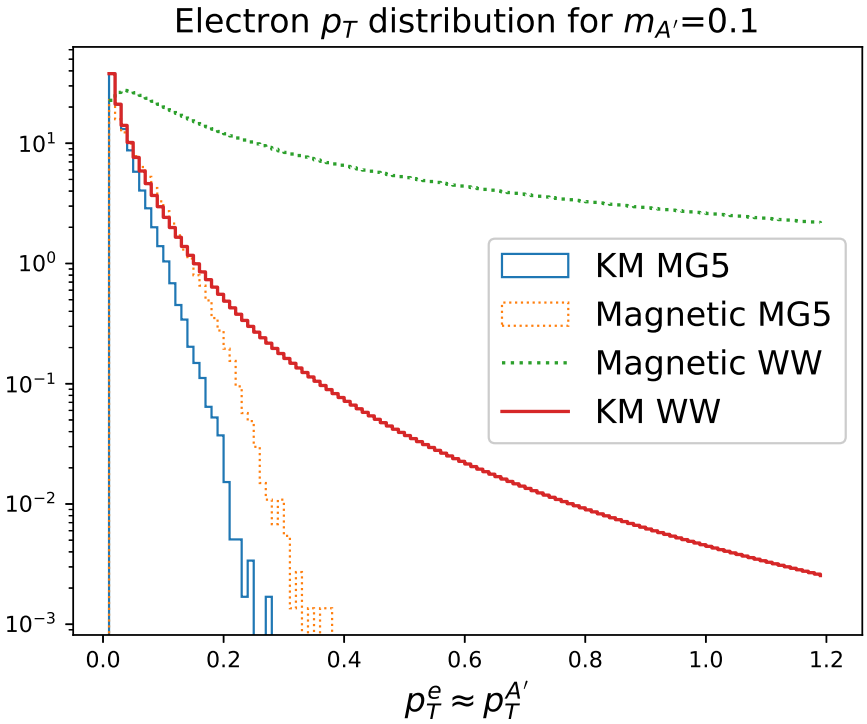

Figure 4.9: The transverse momentum distribution of the recoiling electron in the WW approximation plotted against the MG5 simulation for the KM and magnetic dipole interactions and a DP mass of $m_{A'} = 0.1\,\text{GeV}$. The transverse momentum is plotted in bins of 10 MeV for $p_T^e = 0 - 1.2\,\text{GeV}$.

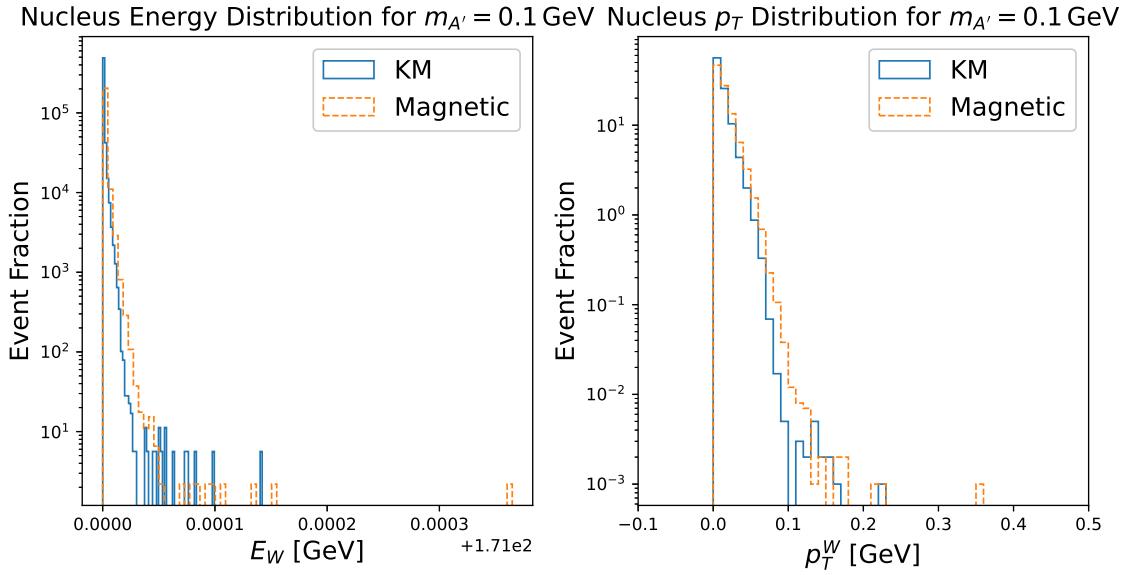

Figure 4.10: Energy and transverse momentum distributions of the final state nucleus for both KM and magnetic dipole interactions. The mass of the DP for these plots is $m_{A'} = 0.1\,\text{GeV}$.

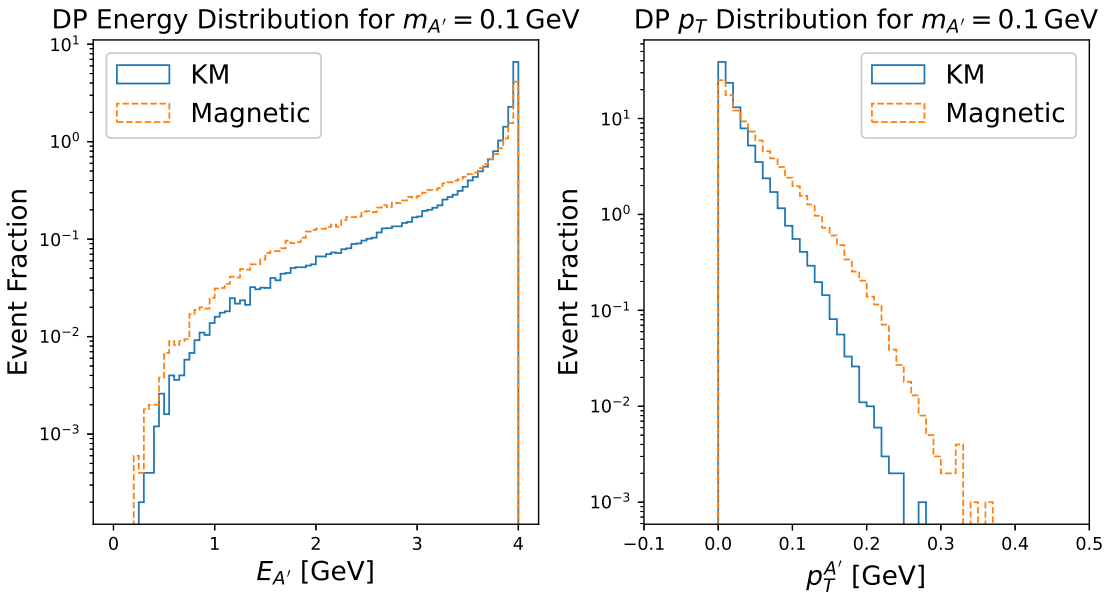

Figure 4.11: Energy and transverse momentum distributions for the DP for both KM and magnetic dipole interactions. The mass of the DP for these plots is $m_{A'} = 0.1\,\mathrm{GeV}$.

5

Discussion and Outlook for Future Work

In this chapter the results of chapters 3 and 4 are discussed further and an outlook for future work to build upon the results of this thesis is presented.

5.1 Discussion of the Results

In the results of chapter 3 and 4 one can see that for both the relic density calculations, section 3.1, and the simulations of the LDMX distributions, section 4.1, the magnetic and electric dipole show very similar behaviour and seem to overlap, and the same goes for the charge and anapole interactions. From looking at the mathematical differences of the overlapping interactions, see the Feynman rules of the DP and electron vertex in equation (2.2), one can note that essentially it is only the addition of a γ^5 to the electric and charge terms that differ them from the magnetic and anapole ones respectively. That the results of the energy and p_T distribution simulations are so similar for these interactions seem to indicate that the CP-violating terms that include the γ^5 do not seem to change the characteristics from the CP-preserving ones and therefore could potentially be difficult to differentiate in an experiment. From the relic density calculations the same type of behaviour is shown which implies that for this example the addition of a γ^5 in the interaction does not seem to make a large difference for the properties of the model, for these types of calculations.

Another interesting aspect that can be seen in the LDMX simulations is that the KM and the charge and anapole interactions are quite similar. This does not only have to do with a γ^5 factor, but looking again at the DP electron interaction one sees that the vertices of the KM and the charge and anapole terms are quite similar with both being proportional to a γ^μ. Further, considering the fact that in the LDMX simulations the DP is treated as a final state particle, and is therefore on-shell, makes $q^2 = m_{A'}^2$, which is constant. From this it then follows that the first part of the charge and anapole interactions $\sim q^2\gamma^\mu$ becomes $\sim m_{A'}^2\gamma^\mu$. This is just a constant times a γ matrix, which is the exact same form as for the KM case $\sim e\epsilon\gamma^\mu$. This could potentially be the reason for the similarity between these curves, taking

into account that the γ^5 in the anapole interaction does not seem to deviate it too much from the charge. Due to the results showing such similarities between KM, charge and anapole interactions the previous arguments would then indicate that the $\sim q^\mu q_\nu \gamma^\nu$ part of the charge and anapole interaction would either also give a constant times the γ matrix or that its impact is small compared to the $\sim q^2\gamma^\mu$ part.

An argument for why the magnetic and electric dipole deviates more from the other interactions then follows from the same type of reasoning, but reversed. In other words they differ from the other interactions due to having a different type of γ-structure, namely that they are proportional to $\sigma^{\mu\nu}$ instead of only γ^μ. In the case of the relic density there are no similarities in the generated Ωh^2 between the KM and the charge and anapole terms. The reason why the same argument does not hold here is because the DP is not on-shell in these calculations, but is instead acting as a virtual mediator particle in the s-channel annihilation/production between the DM and the SM electrons. This means that q^2 does not necessarily equal $m_{A'}^2$ and, possibly, therefore the interactions deviate much more.

For the relic density one can see that the plots of the thermally averaged cross section seem to imply that the shape of the relic abundance curves are correct. This is the case since the constant lines of the thermally averaged cross section in the regions of the parameter space that generate $\Omega h^2 = 0.12$ behave similarly to that of the Ωh^2 plots. For example in figure 3.4 it is seen that $\frac{1}{2}\langle\sigma_{\chi+\chi^*\to e^-+e^+}v\rangle$ stays constant when m_χ and the coupling constant increases for the KM case, for the magnetic and electric interactions it is constant for the case of $\alpha_D \approx 10^{-7}$ no matter the DM mass and finally it also stays constant in the case of decreasing α'_D and increasing m_χ in the relevant regions of the charge and anapole case. Even though the choice of $x_f = 20$ is not the exact freeze-out value for all the points in the parameter space it is still representative for the sake of argument.

Another validation for the relic abundance curves comes from the fact that in the region of $\Omega h^2 = 0.12$ one would expect that the thermally averaged cross section times velocity is fairly close to the WIMP reference value of $\langle\sigma v\rangle \approx 3 \cdot 10^{-26}\,\mathrm{cm}^3/\mathrm{s}$ $\approx 1\,\mathrm{pb}\cdot\mathrm{c}$ [36]. WIMPs are not the DM considered here, but this value still works as a reference value to compare with for this example of thermal DM. If one looks at the parameter region of the $\langle\sigma v\rangle$ plots that correspond to $\Omega h^2 = 0.12$ it is seen that the thermally averaged cross section times velocity is around this reference value, even for the example of $x_f = 20$. This makes the results even more reasonable.

The reason for the difference in the behaviour of the relic density for the different interactions with respect to the coupling constant and the DM mass can be understood from analysing the analytical expressions from the matrix elements that generate the process, see them listed in section 2.3. This is because of their direct relation to the $\langle\sigma v\rangle$ through an integral over the energy, see for example equation 2.22 or more explicitly in equation 3.3. One of the major differences in these matrix elements is that the overall factor of energy increases when looking at different interactions. For KM there is E^0, for magnetic and electric dipole E^2 and for the

charge and anapole E^4. The dimensions are still fine since as mentioned in section 2.1 the g_D and g'_D carry dimensions of GeV^{-1} and GeV^{-2} respectively. This effect of the increasing exponent of the energy in combination with the change of the decay rate, see in equations 2.10 that they are increasing in factors of $m_{A'}$, could be the reason for this change in the $\langle \sigma v \rangle$. This would then also imply the change in the relic abundance curves. This analytical discussion is then further validated by the fact that it coincides with the micrOMEGAs simulations.

Focusing on the results of the MG5 simulations figures 4.1, 4.2, 4.3 and 4.4 a general feature seems to be that the mass of the DP gives larger effects on the energy and transverse momentum than changing the interaction type. Also worth mentioning is that the detector is likely most sensitive in the middle region of the energy and p_T distributions where one still has a lot of events, unlike the higher regions, and is more differentiable from the background events, that are more present in the lower energy spectrum. This seems to be the regions where the magnetic and electric dipole interactions differ the most from the others, for the same mass of the DP, which could be good for differentiating the models in experiments.

In the MG5 simulations the fact that the nucleus also has a cut in the rapidity probably has some effect on the end results of the kinematics, but since the nucleus does not move much and gains very little energy in comparison to its initial, stationary, state this should not change things considerably. Also since this cut is made for all the interactions the qualitative behaviour and differences can still be compared.

5.2 Outlook

The relic density calculation that has been made in section 3, is as mentioned, carried out for an example where complex scalar DM with an s-channel annihilation to the SM electron is considered. For a more thorough analysis one should include more possible final states for the annihilation. For example annihilation to muons could be added to the model through a very similar coupling as the one presented for the electrons and this would also be expected since electrons and muons are so similar. One could also compare other models of DM such as Majorana or Dirac fermions [3] or spin-1 DM [29] and let the coupling constant of these also be a parameter to vary. One could vary the coupling α_{DM} in the case considered here as well and not just have it fixed to $\alpha_{DM} = 0.5$.

For the scattering electron energy and momentum simulations in the LDMX framework, further statistical analysis could be made to make a more confident statement of how differentiable the interactions and masses are. An example of how this could be done is by also including the coupling parameters' effects on the process and make a χ^2 test in a similar fashion to that made for a more analytical approach in chapter IIV of [37], where their model describes a new scalar boson and a comparison is made between making no approximations, WW approximation and the improved WW approximation. An approach like this applied to the MG5 simulations for the different electromagnetic interactions would give a result that could take a stronger

stance on questions such as how likely it is to fit the data to the wrong interaction or mass of the DP. At least how much error is large enough to differentiate between them could be examined. Also what could be considered is adding a detector simulation on top of the MG5 simulations. This would then make the simulation more comparable to an actual experiment.

6

Conclusion

In this thesis the higher order electromagnetic couplings between the DP and the SM electrons have been investigated through relic density calculations and simulations of the energy and transverse momentum distributions in the framework of the LDMX. Starting with the relic density simulations, these give a constraint to the coupling constants with respect to the mass of the DM in the case of complex scalar DM annihilating to SM electrons via the DP. The Ωh^2 curves, that symbolise the measured amount of the DM density for this case, varied substantially in their dependence on the DM mass and coupling constant, for the different interactions. The relic abundance results were validated both by the thermally averaged cross section showing the same pattern as the relic density and that the thermally averaged cross section was calculated in two different ways giving comparable results.

Moving to the LDMX simulations what was found was that the mass of the DP has a large impact on the distributions. This is because as the DP mass increases it both decreases the amount of high energy electrons, due to the DP taking more energy to be created, and also makes the distributions of the different interactions come closer together which could make them more difficult to differentiate in experiments. An increasing DP mass also seemed to have the effect that there are more high p_T recoiling electrons. An overlap of the KM, charge and anapole interactions was found for the energy and p_T distributions and a possible explanation presented for this was that since the DP is treated as on-shell the DP momentum squared, which is what mostly deviates the Feynman rule for charge and anapole from the KM, becomes $q^2 = m_{A'}^2$ which is just a constant. What was also found is that the magnetic and electric terms differ from the other three and could possibly be more easily differentiated in experiments. This is believed to be due to that they have a different γ matrix structure.

The LDMX simulations were also compared to the semi-analytical WW approximation and here alignment between the energy distributions was found, but not between the p_T distributions. Another interesting discovery was that the energy distribution that was created from the WW approximation seems to show a different behaviour to that found in [4]. Strengthened by the alignment with the MG5 simulations the behaviour of the WW distribution presented in this thesis is believed to be correct.

Further, it was concluded that the addition of a γ^5 in the CP-violating electric and anapole interactions does not seem to have a large impact on the models, at least for the type of processes that have been considered here. This was the case for both the LDMX simulations and the relic density calculations and could be seen from the fact that they overlap their CP-conserving counterparts, the magnetic and charge interactions. The fact that they are similar could also result in them being more difficult to differentiate in experiments.

Also presented in the thesis was an outlook for further studies that could be made to the work presented. Brought up was that to elevate the results a further statistical analysis of the distributions could be made. Also for the relic abundance different DM candidates and SM particles that could couple to the DP could be considered.

References

[1] G. Bertone and D. Hooper, "A history of dark matter," *Rev. Mod. Phys.*, vol. 90, no. 4, p. 045 002, Oct. 15, 2018. DOI: 10.1103/RevModPhys.90.045002. [Online]. Available: http://arxiv.org/abs/1605.04909.

[2] A. Berlin, N. Blinov, G. Krnjaic, P. Schuster, and N. Toro, "Dark matter, millicharges, axion and scalar particles, gauge bosons, and other new physics with LDMX," *Phys. Rev. D*, vol. 99, no. 7, p. 075 001, Apr. 1, 2019. DOI: 10.1103/PhysRevD.99.075001. [Online]. Available: https://link.aps.org/doi/10.1103/PhysRevD.99.075001.

[3] T. Åkesson *et al.*, "Light dark matter eXperiment (LDMX)," Aug. 15, 2018. [Online]. Available: http://arxiv.org/abs/1808.05219.

[4] T. G. Rizzo, "Dark moments for the standard model ?" *J. High Energ. Phys.*, vol. 2021, no. 11, p. 35, Nov. 2021. DOI: 10.1007/JHEP11(2021)035. [Online]. Available: http://arxiv.org/abs/2106.11150.

[5] F. Zwicky, "Republication of: The redshift of extragalactic nebulae," *Gen Relativ Gravit*, vol. 41, no. 1, pp. 207–224, Jan. 1, 2009. DOI: 10.1007/s10714-008-0707-4. [Online]. Available: https://doi.org/10.1007/s10714-008-0707-4.

[6] V. C. Rubin, W. K. Ford Jr., and N. Thonnard, "Extended rotation curves of high-luminosity spiral galaxies. IV. systematic dynamical properties, sa -> sc.," *ApJ*, vol. 225, pp. L107–L111, Nov. 1, 1978. DOI: 10.1086/182804. [Online]. Available: https://ui.adsabs.harvard.edu/abs/1978ApJ...225L.107R.

[7] P. Collaboration *et al.*, "Planck 2018 results. VI. cosmological parameters," *Astron. Astrophys.*, vol. 641, A6, Sep. 2020. DOI: 10.1051/0004-6361/201833910. [Online]. Available: http://arxiv.org/abs/1807.06209.

[8] D. J. Fixsen, "The temperature of the cosmic microwave background," *ApJ*, vol. 707, no. 2, pp. 916–920, Dec. 20, 2009. DOI: 10.1088/0004-637X/707/2/916. [Online]. Available: http://arxiv.org/abs/0911.1955.

[9] T. Lasserre and E. Collaboration, *Not enough stellar mass machos in the galactic halo*, Mar. 2, 2000. DOI: 10.48550/arXiv.astro-ph/0002253. [Online]. Available: http://arxiv.org/abs/astro-ph/0002253.

[10] P. Tisserand *et al.*, "Limits on the macho content of the galactic halo from the EROS-2 survey of the magellanic clouds," *Astron. Astrophys.*, vol. 469, no. 2, pp. 387–404, Jul. 2007. DOI: 10.1051/0004-6361:20066017. [Online]. Available: http://arxiv.org/abs/astro-ph/0607207.

[11] B. J. Carr and S. W. Hawking, "Black holes in the early universe," *Monthly Notices of the Royal Astronomical Society*, vol. 168, no. 2, pp. 399–415, Aug. 1, 1974. DOI: 10.1093/mnras/168.2.399. [Online]. Available: https://doi.org/10.1093/mnras/168.2.399.

[12] J. L. Gervais and B. Sakita, "Field theory interpretation of supergauges in dual models," *Nuclear Physics B*, vol. 34, no. 2, pp. 632–639, Nov. 15, 1971. DOI: 10.1016/0550-3213(71)90351-8. [Online]. Available: https://www.sciencedirect.com/science/article/pii/0550321371903518.

[13] R. D. Peccei and H. R. Quinn, "Constraints imposed by CP conservation in the presence of pseudoparticles," *Phys. Rev. D*, vol. 16, no. 6, pp. 1791–1797, Sep. 15, 1977. DOI: 10.1103/PhysRevD.16.1791. [Online]. Available: https://link.aps.org/doi/10.1103/PhysRevD.16.1791.

[14] G. Steigman and M. S. Turner, "Cosmological constraints on the properties of weakly interacting massive particles," *Nuclear Physics B*, vol. 253, pp. 375–386, Jan. 1, 1985. DOI: 10.1016/0550-3213(85)90537-1. [Online]. Available: https://www.sciencedirect.com/science/article/pii/0550321385905371.

[15] E. W. Kolb and M. S. Turner, *The Early Universe*. Taylor and Francis, 1990, vol. 69. DOI: 10.1201/9780429492860.

[16] L. J. Hall, K. Jedamzik, J. March-Russell, and S. M. West, "Freeze-in production of FIMP dark matter," *J. High Energ. Phys.*, vol. 2010, no. 3, p. 80, Mar. 2010. DOI: 10.1007/JHEP03(2010)080. [Online]. Available: http://arxiv.org/abs/0911.1120.

[17] T. Gray, "How was dark matter produced in the early universe? a study of fermionic dark matter with a z-prime portal," Master of Science, Carleton University, Ottawa, Ontario, 2020. DOI: 10.22215/etd/2020-14172. [Online]. Available: https://repository.library.carleton.ca/concern/etds/44558f29n.

[18] B. W. Lee and S. Weinberg, "Cosmological lower bound on heavy-neutrino masses," *Phys. Rev. Lett.*, vol. 39, no. 4, pp. 165–168, Jul. 25, 1977. DOI: 10.1103/PhysRevLett.39.165. [Online]. Available: https://link.aps.org/doi/10.1103/PhysRevLett.39.165.

[19] J. Cooley *et al.*, "Report of the topical group on particle dark matter for snowmass 2021," Sep. 15, 2022. [Online]. Available: http://arxiv.org/abs/2209.07426.

[20] T. Raubenheimer *et al.*, "DASEL: Dark sector experiments at LCLS-II," Jan. 24, 2018. DOI: 10.48550/arXiv.1801.07867. [Online]. Available: http://arxiv.org/abs/1801.07867.

[21] M. D. Schwartz, *TASI lectures on collider physics*, Harvard University, Sep. 13, 2017. [Online]. Available: http://arxiv.org/abs/1709.04533.

[22] J. Alwall *et al.*, "The automated computation of tree-level and next-to-leading order differential cross sections, and their matching to parton shower simulations," *J. High Energ. Phys.*, vol. 2014, no. 7, p. 79, Jul. 2014. DOI: 10.1007/JHEP07(2014)079. [Online]. Available: http://arxiv.org/abs/1405.0301.

[23] A. Alloul, N. D. Christensen, C. Degrande, C. Duhr, and B. Fuks, "FeynRules 2.0 - a complete toolbox for tree-level phenomenology," *Computer Physics*

Communications, vol. 185, no. 8, pp. 2250–2300, Aug. 2014. DOI: 10.1016/j.cpc.2014.04.012. [Online]. Available: http://arxiv.org/abs/1310.1921.

[24] N Christensen, C. Duhr, and B. Fuks. "SM.fr on StandardModel – attachment – FeynRules." (), [Online]. Available: https://feynrules.irmp.ucl.ac.be/attachment/wiki/StandardModel/SM.fr.

[25] G. Belanger, F. Boudjema, A. Pukhov, and A. Semenov, "micrOMEGAs2.0: A program to calculate the relic density of dark matter in a generic model," *Computer Physics Communications*, vol. 176, no. 5, pp. 367–382, Mar. 2007. DOI: 10.1016/j.cpc.2006.11.008. [Online]. Available: http://arxiv.org/abs/hep-ph/0607059.

[26] A. Belyaev, N. D. Christensen, and A. Pukhov, "CalcHEP 3.4 for collider physics within and beyond the standard model," *Computer Physics Communications*, vol. 184, no. 7, pp. 1729–1769, Jul. 2013. DOI: 10.1016/j.cpc.2013.01.014. [Online]. Available: http://arxiv.org/abs/1207.6082.

[27] R. Mertig, M. Böhm, and A. Denner, "Feyn calc - computer-algebraic calculation of feynman amplitudes," *Computer Physics Communications*, vol. 64, no. 3, pp. 345–359, Jun. 1, 1991. DOI: 10.1016/0010-4655(91)90130-D. [Online]. Available: https://www.sciencedirect.com/science/article/pii/001046559190130D.

[28] V. Shtabovenko, R. Mertig, and F. Orellana, "FeynCalc 10: Do multiloop integrals dream of computer codes?," Dec. 21, 2023. DOI: 10.48550/arXiv.2312.14089. [Online]. Available: http://arxiv.org/abs/2312.14089.

[29] R. Catena and T. R. Gray, "Spin-1 thermal targets for dark matter searches at beam dump and fixed target experiments," Oct. 19, 2023. [Online]. Available: http://arxiv.org/abs/2307.02207.

[30] M. E. Peskin and D. V. Schroeder, *An Introduction to Quantum Field Theory*. Boca Raton, FL, USA: Taylor & Francis Group, 1995.

[31] R. Catena, J. Conrad, and M. B. Krauss, "Compatibility of a dark matter discovery at XENONnT/LZ with the WIMP thermal production mechanism," *Phys. Rev. D*, vol. 97, no. 10, p. 103 002, May 1, 2018. DOI: 10.1103/PhysRevD.97.103002. [Online]. Available: http://arxiv.org/abs/1712.07969.

[32] P. Gondolo and G. Gelmini, "Cosmic abundances of stable particles: Improved analysis," *Nuclear Physics B*, vol. 360, no. 1, pp. 145–179, Aug. 1991. DOI: 10.1016/0550-3213(91)90438-4. [Online]. Available: https://linkinghub.elsevier.com/retrieve/pii/0550321391904384.

[33] D. Morrissey, *Lecture note #2: Thermal dark matter creation*, Apr. 16, 2012. [Online]. Available: https://particletheory.triumf.ca/dmorrissey/Teaching/PI-DM-2012/notes-2.pdf.

[34] J. D. Bjorken, R. Essig, P. Schuster, and N. Toro, "New fixed-target experiments to search for dark gauge forces," *Phys. Rev. D*, vol. 80, no. 7, p. 075 018, Oct. 28, 2009. DOI: 10.1103/PhysRevD.80.075018. [Online]. Available: http://arxiv.org/abs/0906.0580.

[35] F. Kahlhoefer, K. Schmidt-Hoberg, T. Schwetz, and S. Vogl, "Implications of unitarity and gauge invariance for simplified dark matter models," *J. High*

Energ. Phys., vol. 2016, no. 2, p. 16, Feb. 2016. DOI: 10.1007/JHEP02(2016)016. [Online]. Available: http://arxiv.org/abs/1510.02110.

[36] G. Steigman, B. Dasgupta, and J. F. Beacom, "Precise relic WIMP abundance and its impact on searches for dark matter annihilation," *Phys. Rev. D*, vol. 86, no. 2, p. 023 506, Jul. 3, 2012. DOI: 10.1103/PhysRevD.86.023506. [Online]. Available: https://link.aps.org/doi/10.1103/PhysRevD.86.023506.

[37] Y.-S. Liu, D. McKeen, and G. A. Miller, "The validity of the weizsacker-williams approximation and the analysis of beam dump experiments: Production of a new scalar boson," *Phys. Rev. D*, vol. 95, no. 3, p. 036 010, Feb. 14, 2017. DOI: 10.1103/PhysRevD.95.036010. [Online]. Available: http://arxiv.org/abs/1609.06781.

[38] F. Mandl and G. Shaw, *Quantum Field Theory*, 2. ed. Chichester, UK: Wiley, 2010.

[39] D. J. Griffiths, *Introduction to Elementary Particles*, 2. ed. Weinheim, Germany: Wiley-VCH, 2008.

A

Derivation of Feynman rules

What follows is the QFT calculations that generate the Feynman rules from the different interaction Lagrangians used for the DP couplings to the DM, equation (2.4), and the electron, equation (2.3). Only the calculations are provided and no deeper discussion on the theory of QFT is provided. For details on this see [30, 38].

A.1 Feynman rules for scalar DM

The interaction Lagrangian for this case is

$$\mathcal{L}_I = -g_{DM} A'_\mu (\chi^* \partial^\mu \chi - \chi \partial^\mu \chi^*). \tag{A.1}$$

Consider one scalar DM in the initial state, $|i\rangle = |\chi, p, s\rangle$, and one scalar DM and the dark photon in the final state, $|f\rangle = |\chi, p', s'; A', q, r\rangle$. Using the S-matrix formalism, Wick's theorem and perturbation theory the vertex Feynman rule can be calculated.

$$\begin{aligned} S_{fi}^{(1)} =& -i \int d^4x \langle f|T\{\mathcal{H}_I\}|i\rangle = \{\mathcal{H}_I = -\mathcal{L}_I\} = \\ =& g_{DM} \int d^4x \Big(\langle \overbrace{\chi, p', s'; \overbrace{A', q, r|N\{\overbrace{A'_\mu \chi^*}\partial^\mu \chi\}}|\chi}, p, s\rangle - \\ & - \langle \overbrace{\chi, p', s'; \overbrace{A', q, r|N\{\overbrace{A'_\mu \chi}\partial^\mu \chi^*\}}|\chi}, p, s\rangle \Big). \end{aligned} \tag{A.2}$$

With χ being a scalar field we can just move it to achieve normal ordering. Doing so and utilizing the positive and negative frequency parts of $(A^+ + A^-), (\chi^+ + \chi^-)$, giving annihilation and creation operators respectively it is possible to evaluate this. Using a general complex scalar field as an example of the quantisation, [30, 38]

$$\phi(x) = \int \frac{d^3\vec{p}}{(2\pi)^3} \left(\frac{1}{2E_{\vec{p}}}\right)^{1/2} \left[a_{\vec{p}} e^{-ip\cdot x} + b^\dagger_{\vec{p}} e^{ip\cdot x}\right], \tag{A.3}$$

one notes that acting with a spacetime derivative ∂_μ on the field will "bring down" a momentum factor as $\mp ip_\mu$ ($\mp$ depending on if it is part of the positive or negative frequency part/annihilation or creation part) [38]. This allows for the evaluation of the Wick contractions using that the dark photon has a polarisation vector, $\epsilon'_{r\mu}$, as the regular photon, one gets

$$S_{fi}^{(1)} = g_{DM} \int d^4x \left(\epsilon'_{r\mu}(\vec{q}) e^{iq\cdot x} e^{ip'\cdot x} (-ip^\mu) e^{-ip\cdot x} - \epsilon'_{r\mu}(\vec{q}) e^{iq\cdot x} (ip'^\mu) e^{ip'\cdot x} e^{-ip\cdot x} \right) \langle 0|0\rangle, \tag{A.4}$$

where the $|0\rangle$ states come from the annihilation of the initial and final states. Using that the states are normalised as $\langle 0|0\rangle = 1$ and the Dirac-δ relation [30]

$$\int d^4x e^{ip\cdot x} = (2\pi)^4 \delta^{(4)}(p), \tag{A.5}$$

the calculation of $S_{fi}^{(1)}$ simplifies to

$$S_{fi}^{(1)} = -ig_{DM} \int d^4x (p^\mu + p'^\mu) \epsilon'_{r\mu}(\vec{q}) e^{i(q+p'-p)\cdot x} = \tag{A.6}$$

$$= -ig_{DM}(p^\mu + p'^\mu)\epsilon'_{r\mu}(2\pi)^4 \delta^{(4)}(q + p' - p) = i\mathcal{M}(2\pi)^4 \delta^{(4)}(q + p' - p). \tag{A.7}$$

From the above expression one notes that the process between scalar dark matter and the dark photon yields the following Feynman rule for the vertex

$$\chi \to A'\chi \sim -ig_{DM}(p^\mu + p'^\mu). \tag{A.8}$$

A.2 Feynman rules for the interaction Lagrangian

The Lagrangian in question is given in equation (2.3) and repeated below

$$\begin{aligned} \mathcal{L}_I(x) =& e\epsilon \bar{\psi}\gamma^\mu \psi A'_\mu - g_D \partial_\nu (\bar{\psi}\sigma^{\mu\nu}\psi) A'_\mu - ig_D \partial_\nu (\bar{\psi}\sigma^{\mu\nu}\gamma^5\psi) A'_\mu - \\ & - g'_D \left[\Box(\bar{\psi}\gamma^\mu\psi) - \partial^\mu \partial_\nu (\bar{\psi}\gamma^\nu \psi) \right] A'_\mu + \\ & + g'_D \left[\Box(\bar{\psi}\gamma^\mu\gamma^5\psi) - \partial^\mu \partial_\nu (\bar{\psi}\gamma^\nu\gamma^5 \psi) \right] A'_\mu. \end{aligned} \tag{A.9}$$

We can find the Feynman rules for the vertex e^-, e^+, A' by looking at the process $e^- \to e^- + A'$ (which is not a physical process but gives the Feynman rule for the vertex in question). This means that $|i\rangle = |e^-, p, s\rangle$ and $|f\rangle = |e^-, p', s'; A', q, r\rangle$.

Due to four momentum conservation $p - p' = q$.

$$\begin{aligned}
S_{fi}^{(1)} =& - i \int d^4x \langle f|T\{\underbrace{-\mathcal{L}_I}_{=\mathcal{H}_I}\}|i\rangle = \\
=& - i \int d^4x \langle A', q, r; e^-, p', s'|T\Bigg\{ - \Bigg(\underbrace{e\epsilon\bar{\psi}\gamma^\mu\psi A'_\mu}_{I} - \underbrace{g_D\partial_\nu(\bar{\psi}\sigma^{\mu\nu}\psi)A'_\mu}_{II} - \\
& - \underbrace{ig_D\partial_\nu(\bar{\psi}\sigma^{\mu\nu}\gamma^5\psi)A'_\mu}_{III} - \\
& - \underbrace{g'_D\left[\Box(\bar{\psi}\gamma^\mu\psi) - \partial^\mu\partial_\nu(\bar{\psi}\gamma^\nu\psi)\right]A'_\mu}_{IV} + \\
& + \underbrace{g'_D\left[\Box(\bar{\psi}\gamma^\mu\gamma^5\psi) - \partial^\mu\partial_\nu(\bar{\psi}\gamma^\nu\gamma^5\psi)\right]A'_\mu}_{V} \Bigg)\Bigg\}|e^-, p, s\rangle.
\end{aligned} \tag{A.10}$$

Dealing with one term at a time. First the KM

$$\begin{aligned}
I =& i \int d^4x \langle \overbrace{A'; e^-|e\epsilon\bar{\psi}\gamma^\mu\psi A'_\mu|e^-}\rangle = \\
=& i \int d^4x \bar{u}^{s'}(p')e^{ip'\cdot x}\gamma^\mu\epsilon'_{r\mu}(\vec{q})e^{iq\cdot x}u^s(p)e^{-ip\cdot x} = \\
=& i \int d^4x \bar{u}^{s'}(p')\gamma^\mu\epsilon'_{r\mu}(\vec{q})u^s(p)e^{i(q+p'-p)\cdot x} = \\
=& \left\{\int d^4x e^{ip\cdot x} = (2\pi)^4\delta^{(4)}(p)\right\} = \\
=& ie\epsilon\bar{u}^{s'}(p')\gamma^\mu\epsilon'_{r\mu}(\vec{q})u^s(p)(2\pi)^4\delta^{(4)}(q+p-p') = i\mathcal{M}(2\pi)^4\delta^{(4)}(q+p-p') \\
\implies & (e^- \to e^- + A')_I \sim ie\epsilon\gamma^\mu.
\end{aligned} \tag{A.11}$$

Then the magnetic dipole term

$$\begin{aligned}
II =& - i \int d^4x \left(\langle \overbrace{A'; e^-|g_D\partial_\nu\bar{\psi}\sigma^{\mu\nu}\psi A'_\mu|e^-}\rangle + \langle \overbrace{A'; e^-|g_D\bar{\psi}\sigma^{\mu\nu}\partial_\nu\psi A'_\mu|e^-}\rangle \right) = \\
=& \{\overbrace{\partial_\nu\psi|e^-}\rangle = (-ip_\nu)u^s(p)e^{-ip\cdot x}|0\rangle, \quad \langle e^-|\overbrace{\partial_\nu\bar{\psi}} = (+ip'_\nu)\bar{u}^{s'}(p')e^{ip\cdot x}\} = \\
=& - ig_D \int d^4x \Bigg((+ip'_\nu)\bar{u}^{s'}(p')e^{ip\cdot x}\sigma^{\mu\nu}\epsilon'_{r\mu}(\vec{q})e^{iq\cdot x}u^s(p)e^{-ip\cdot x} + \\
& + \bar{u}^{s'}(p')e^{ip\cdot x}\sigma^{\mu\nu}\epsilon'_{r\mu}(\vec{q})e^{iq\cdot x}(-ip_\nu)u^s(p)e^{-ip\cdot x}\Bigg) = \\
=& g_D \int d^4x \underbrace{(p'_\nu - p_\nu)}_{-q_\nu}\bar{u}^{s'}(p')\sigma^{\mu\nu}\epsilon'_{r\mu}(\vec{q})u^s(p)e^{i(q+p'-p)\cdot x} = \\
=& - g_D\bar{u}^{s'}(p')\sigma^{\mu\nu}q_\nu\epsilon'_{r\mu}(\vec{q})u^s(p)(2\pi)^4\delta^{(4)}(q+p-p') \\
\implies & (e^- \to e^- + A')_{II} \sim -g_D\sigma^{\mu\nu}q_\nu.
\end{aligned} \tag{A.12}$$

Term III, the electric dipole term, is the same as the magnetic, term II, but with an extra γ^5 and an i,

$$(e^- \to e^- + A')_{III} \sim -ig_D \sigma^{\mu\nu}\gamma^5 q_\nu. \tag{A.13}$$

To get term IV, charge, and V, the anapole moment, one can repeatedly use the product rule resulting in

$$\begin{aligned}\underbrace{\Box}_{\partial^\nu\partial_\nu}(\bar\psi\gamma^\mu\psi) - \partial^\mu\partial_\nu(\bar\psi\gamma^\nu\psi) =& \partial^\nu(\partial_\nu\bar\psi\gamma^\mu\psi + \bar\psi\gamma^\mu\partial_\nu\psi) - \partial^\mu(\partial_\nu\bar\psi\gamma^\nu\psi + \bar\psi\gamma^\nu\partial_\nu\psi) = \\ =& \Box\bar\psi\gamma^\mu\psi + 2\partial_\nu\bar\psi\gamma^\mu\partial^\nu\psi + \bar\psi\gamma^\mu\Box\psi - \\ & - \partial^\mu\partial_\nu\bar\psi\gamma^\nu\psi - \partial_\nu\bar\psi\gamma^\nu\partial^\mu\psi - \partial^\mu\bar\psi\gamma^\nu\partial_\nu\psi - \bar\psi\gamma^\nu\partial^\mu\partial_\nu\psi.\end{aligned} \tag{A.14}$$

The contraction for the second derivatives gives a momentum squared dropping down. For example for $\Box$ one get

$$\overbrace{\Box\psi|e^-}\rangle = (-ip_\nu)u^s(p)\partial^\nu e^{-ip\cdot x}|0\rangle = -p^2u^s(p)e^{-ip\cdot x}|0\rangle, \quad \langle\overbrace{e^-|\Box}\bar\psi = -p'^2\bar u^{s'}(p')e^{ip\cdot x}\langle 0| \tag{A.15}$$

IV then follows similarly to the other terms (not writing out the contractions, but contracting as above $\bar\psi$ with $\langle e^-|$, ψ with $|e^-\rangle$ and A' with $\langle A'|$)

$$\begin{aligned}IV =& -ig'_D\int d^4x\bar u^{s'}(p')\gamma^\mu u^s(p)\epsilon'_{r\mu}(\vec q)[-p^2 + 2(ip'_\nu)(-ip^\nu) - p'^2]e^{i(q+p'-p)\cdot x} - \\ & - \bar u^{s'}(p')\gamma^\nu u^s(p)\epsilon'_{r\mu}(\vec q)[(-ip^\mu)(-ip_\nu) + (ip'_\nu)(-ip^\mu) + (ip'^\mu)(-ip_\nu) + \\ & + (ip'^\mu)(ip'_\nu)]e^{i(q+p'-p)\cdot x} = \\ =& -ig'_D\Big[-\underbrace{(p^2 - 2p'_\nu p^\nu + p'^2)}_{(p-p')^2=q^2}\bar u^{s'}(p')\gamma^\mu u^s(p)\epsilon'_{r\mu}(\vec q) + \\ & + \underbrace{(p^\mu p_\nu - p'_\nu p^\mu - p'^\mu p_\nu + p'^\mu p'_\nu)}_{(p-p')^\mu(p-p')_\nu = q^\mu q_\nu}\bar u^{s'}(p')\gamma^\nu u^s(p)\epsilon'_{r\mu}(\vec q)\Big](2\pi)^4\delta^{(4)}(q+p'-p) = \\ =& -ig'_D\bar u^{s'}(p')[-q^2\gamma^\mu + q^\mu q_\nu\gamma^\nu]u^s(p)\epsilon'_{r\mu}(\vec q)(2\pi)^4\delta^{(4)}(q+p'-p) \\ \implies& (e^- \to e^- + A')_{IV} \sim ig'_D[q^2\gamma^\mu - q^\mu \not{q}].\end{aligned} \tag{A.16}$$

As with II and III one can get V from IV by seeing that the only difference is adding a γ^5 and a $-$ sign. This gives

$$(e^- \to e^- + A')_V \sim -ig'_D[q^2\gamma^\mu\gamma^5 - q^\mu \not{q}\gamma^5]. \tag{A.17}$$

The total Feynman rule is then given by the sum of these. To differentiate the interactions the form factors M, E, C, A that are treated as constants in this thesis

and included in the coupling constants g_D and g'_D are explicitly written out,

$$(e^- \to e^- + A')_{\text{Tot}} \sim \underbrace{ie\epsilon\gamma^\mu}_{\text{KM}} - g_D\sigma^{\mu\nu}q_\nu(\underbrace{M}_{\text{Magnetic}} + \underbrace{iE\gamma^5}_{\text{Electric}}) + ig'_D(q^2\gamma^\mu - q^\mu \not{q})(\underbrace{C}_{\text{Charge}} - \underbrace{A\gamma^5}_{\text{Anapole}}). \tag{A.18}$$

For constant form factors this can be seen to coincide with equation 2.2, which is in agreement with [4], and from this it is concluded that the position space Lagrangian used is the correct Lagrangian.

B

Derivation of Matrix Elements Assuming Complex Scalar DM

This section contains the derivation of the matrix elements for the different couplings between the electron and the DP, assuming scalar DM. The creation is through an s-channel. Shown in figure 2.2 but repeated below in figure B.1.

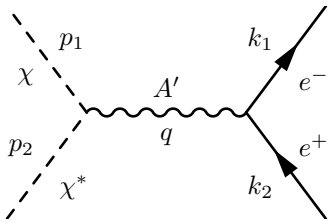

Figure B.1: The s-channel process for complex scalar DM annihilation into SM electrons through a DP mediator.

This means that the definition of the DP momentum in the Feynman rules is changed to $q = p_1 + p_2 = k_1 + k_2$, where p_1 and p_2 are the four momenta of the incoming DM and k_1 and k_2 the outgoing electron and positron four momenta. This changes the Feynman rules of the DM DP vertex, given in equation (A.1) and (A.8) to $\chi\chi^* \to A' \sim -ig_{DM}(p_1^\mu - p_2^\mu)$ since $p \to p_1$ due to χ being incoming and $p' \to -p_2$ due to χ^* being the incoming complex conjugate version instead of χ outgoing. The Feynman rules for the vertex between electrons and DP, given in (2.2) and (A.18) does not change but the definition of the DP momenta changes from $q = p - p'$ to $q = k_1 + k_2 (= p_1 + p_2)$. This can be seen as the outgoing electron four-momentum becomes $p' \to k_1$ and the incoming electron becomes an outgoing positron i.e. $p \to -k_2$, giving $q = -k_1 - k_2$, but the outgoing DP becomes an incoming DP $q \to -q$. In the calculations the propagator for a massive gauge boson mediator is used, with the inclusion of the decay rate $\Gamma_{A'}$ to deal with the resonances. This is given by [30, 39]

$$\frac{-i}{q^2 - m_{A'}^2 + i m_{A'} \Gamma_{A'}} \left(\eta_{\mu\nu} - \frac{q_\mu q_\nu}{m_{A'}^2} \right). \tag{B.1}$$

The trace calculations performed below have been crosschecked with the Mathemat-

ica package FeynCalc [27, 28].

B.1 Kinetic Mixing

The matrix element for the s-channel process is then given by using the Feynman rules as

$$i\mathcal{M} = [-ig_{DM}(p_1^\mu - p_2^\mu)] \left[\frac{-i}{q^2 - m_{A'}^2 + im_{A'}\Gamma_{A'}} \left(\eta_{\mu\nu} - \frac{q_\mu q_\nu}{m_{A'}^2}\right)\right] [\bar{u}^{s_1}(k_1) i\epsilon e \gamma^\mu v^{s_2}(k_2)] = \tag{B.2}$$

$$= \frac{-ig_{DM}\epsilon e}{q^2 - m_{A'}^2 + im_{A'}\Gamma_{A'}} \left[(p_1^\mu - p_2^\mu) \left(\eta_{\mu\nu} - \frac{q_\mu q_\nu}{m_{A'}^2}\right) \bar{u}^{s_1}(k_1)\gamma^\mu v^{s_2}(k_2)\right]. \tag{B.3}$$

The complex conjugate of which is, using $(\gamma^\mu)^\dagger = \gamma^0\gamma^\mu\gamma^0$,

$$(i\mathcal{M})^* = \frac{ig_{DM}\epsilon e}{q^2 - m_{A'}^2 - im_{A'}\Gamma_{A'}} \left[(p_1^\mu - p_2^\mu) \left(\eta_{\mu\nu} - \frac{q_\mu q_\nu}{m_{A'}^2}\right) \bar{v}^{s_2}(k_2)\gamma^\mu u^{s_1}(k_1)\right]. \tag{B.4}$$

We want to take the modulus square of this matrix element as well as average it over initial spins and sum over final spins, i.e. $\overline{|\mathcal{M}|^2} = \frac{1}{S_i}\sum_{s_1,s_2=1}^{2} |\mathcal{M}|^2 = \frac{1}{S_i}\sum_{s_1,s_2=1}^{2} i\mathcal{M}(i\mathcal{M})^*$. Since the incoming particles are scalar they have zero spin ($S_i = 1$). To evaluate the sum we have to use the following spin sum rules of u and v [30]

$$\begin{aligned} \sum_s u^s(p)\bar{u}^s(p) &= (\not{p} + m), \\ \sum_s v^s(p)\bar{v}^s(p) &= (\not{p} - m), \end{aligned} \tag{B.5}$$

where m is the mass of the fermion in question, in our case $m = m_e$. Proceeding the matrix element squared becomes, defining $d^\mu \equiv (p_1^\mu - p_2^\mu)$,

$$\overline{|\mathcal{M}|^2} = \underbrace{\frac{g_{DM}^2\epsilon^2 e^2}{(q^2 - m_{A'}^2)^2 + m_{A'}^2\Gamma_{A'}^2}}_{=C} \sum_{s_1,s_2=1}^{2} d^\mu \left(\eta_{\mu\nu} - \frac{q_\mu q_\nu}{m_{A'}^2}\right) d^\rho \left(\eta_{\rho\sigma} - \frac{q_\rho q_\sigma}{m_{A'}^2}\right) \times \tag{B.6}$$

$$\times [\bar{v}^{s_2}(k_2)\gamma^\sigma u^{s_1}(k_1)] [\bar{u}^{s_1}(k_1)\gamma^\nu v^{s_2}(k_2)] = \tag{B.7}$$

$$= C d^\mu \left(\eta_{\mu\nu} - \frac{q_\mu q_\nu}{m_{A'}^2}\right) d^\rho \left(\eta_{\rho\sigma} - \frac{q_\rho q_\sigma}{m_{A'}^2}\right) \sum_{s2} (\bar{v}^{s_2}(k_2)_a \gamma^\sigma_{ab} (\not{k}_1 + m_e)_{bc} \gamma^\nu_{cd} v^{s_2}(k_2)_d) \tag{B.8}$$

$$= C d^\mu \left(\eta_{\mu\nu} - \frac{q_\mu q_\nu}{m_{A'}^2}\right) d^\rho \left(\eta_{\rho\sigma} - \frac{q_\rho q_\sigma}{m_{A'}^2}\right) \sum_{s2} (v^{s_2}(k_2)_d \bar{v}^{s_2}(k_2)_a \gamma^\sigma_{ab} (\not{k}_1 + m_e)_{bc} \gamma^\nu_{cd}) = \tag{B.9}$$

$$= \{A_a B_{cd} C_{da} = Tr[ABC]\} = \tag{B.10}$$

$$= C d^\mu \left(\eta_{\mu\nu} - \frac{q_\mu q_\nu}{m_{A'}^2}\right) d^\rho \left(\eta_{\rho\sigma} - \frac{q_\rho q_\sigma}{m_{A'}^2}\right) Tr[(\not{k}_2 - m_e)\gamma^\sigma(\not{k}_1 + m_e)\gamma^\nu] \tag{B.11}$$

The indices $a, b, c, ...$ are the spin indices. This can be simplified by realising that $q_\mu d^\mu = (p_{1,\mu} + p_{2,\mu})(p_1^\mu - p_2^\mu) = 0$, which can be seen since this is a Lorentz invariant product and in the CM frame $(p_{1,\mu} + p_{2,\mu}) = (2E, \vec{0})$ and $(p_1^\mu - p_2^\mu) = (0, 2\vec{p})$. The matrix elements squared becomes

$$\overline{|\mathcal{M}|^2} = C d^\mu \eta_{\mu\nu} d^\rho \eta_{\rho\sigma} Tr[(\not{k}_2 - m_e)\gamma^\sigma(\not{k}_1 + m_e)\gamma^\nu]. \tag{B.12}$$

Now using the trace identity $Tr[\gamma^\mu\gamma^\nu\gamma^\rho\gamma^\sigma] = 4(\eta^{\mu\nu}\eta^{\rho\sigma} - \eta^{\mu\rho}\eta^{\nu\sigma} + \eta^{\mu\sigma}\eta^{\nu\rho})$ [30] this trace can be calculated. The final expression becomes

$$\overline{|\mathcal{M}|^2} = \frac{4g_{DM}^2\epsilon^2e^2}{(q^2 - m_{A'}^2)^2 + m_{A'}^2\Gamma_{A'}^2}\left[2(d\cdot k_1)(d\cdot k_2) - (k_1\cdot k_2)d^2 - m_e^2 d^2\right] \tag{B.13}$$

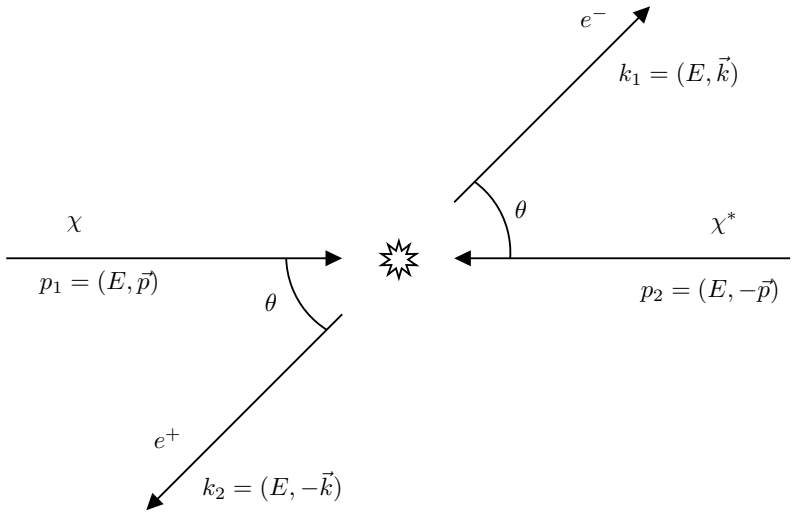

Figure B.2: Schematic picture of the annihilation process of DM into an electron and a positron shown in the CM frame of the interaction.

Next we go to the CM frame, see figure B.2, where the incoming particle momenta become $p_1^\mu = (E, \vec{p})$, $p_2^\mu = (E, -\vec{p})$ and the outgoing $k_1^\mu = (E, \vec{k})$ and $k_2^\mu = (E, -\vec{k})$. Here $E = \frac{E_{CM}}{2}$ and $\vec{p}, \vec{k}$ are three momenta of the respective particles. It has also been taken into consideration that the incoming (outgoing) particles have the same mass, m_χ (m_e). The angle θ is between $\vec{p}$ and $\vec{k}$. The above definitions leads to $d^\mu = (0, 2\vec{p})$ and $q^\mu = (2E, \vec{0})$. The matrix element then becomes

$$\overline{|\mathcal{M}|^2_{CM}} = \frac{16g_{DM}^2\epsilon^2e^2}{(q^2 - m_{A'}^2)^2 + m_{A'}^2\Gamma_{A'}^2}|\vec{p}|^2(E^2 + |\vec{k}|^2 - 2|\vec{k}|^2 cos^2\theta + m_e^2). \tag{B.14}$$

B.2 Magnetic Dipole Moment

When doing the same calculation for the magnetic dipole coupling the only difference comes from the $A'e^-e^+$ vertex and is given by $-g_D\sigma^{\mu\nu}q_\nu$, where $\sigma^{\mu\nu} = \frac{i}{2}[\gamma^\mu, \gamma^\nu]$.

Otherwise the matrix element can be derived in the same way using the Feynman rules, once again defining $d^\mu \equiv (p_1^\mu - p_2^\mu)$,

$$\begin{aligned} i\mathcal{M} &= [-ig_{DM}d^\mu]\left[\frac{-i}{q^2 - m_{A'}^2 + im_{A'}\Gamma_{A'}}\left(\eta_{\mu\nu} - \frac{q_\mu q_\nu}{m_{A'}^2}\right)\right][\bar{u}^{s_1}(k_1)(-g_D\sigma^{\nu\rho}q_\rho)v^{s_2}(k_2)] = \\ &= \{d^\mu q_\mu = 0\} = \\ &= \frac{g_{DM}g_D}{q^2 - m_{A'}^2 + im_{A'}\Gamma_{A'}} d^\mu \eta_{\mu\nu} q_\rho \left[\bar{u}^{s_1}(k_1)\sigma^{\nu\rho}v^{s_2}(k_2)\right], \end{aligned} \tag{B.15}$$

and the complex conjugate, using that $(\sigma^{\mu\nu})^\dagger = \gamma^0\sigma^{\mu\nu}\gamma^0$,

$$(i\mathcal{M})^* = \frac{g_{DM}g_D}{q^2 - m_{A'}^2 - im_{A'}\Gamma_{A'}} d^\mu \eta_{\mu\nu} q_\rho \left[\bar{v}^{s_2}(k_2)\sigma^{\nu\rho}u^{s_1}(k_1)\right]. \tag{B.16}$$

Squaring, summing over spins and averaging over initial spins one gets ($d^\mu\eta_{\mu\nu} = d_\nu$),

$$\begin{aligned} \overline{|\mathcal{M}|^2} =& \underbrace{\frac{g_{DM}^2 g_D^2}{(q^2 - m_{A'}^2)^2 + m_{A'}^2\Gamma_{A'}^2}}_{=D} d_\mu q_\nu d_\rho q_\sigma \sum_{s_1,s_2=1}^{2} [\bar{u}^{s_1}(k_1)\sigma^{\mu\nu}v^{s_2}(k_2)]\,[\bar{v}^{s_2}(k_2)\sigma^{\rho\sigma}u^{s_1}(k_1)] = \\ =& D d_\mu q_\nu d_\rho q_\sigma Tr[(\not{k}_1 + m_e)\sigma^{\mu\nu}(\not{k}_2 - m_e)\sigma^{\rho\sigma}]. \end{aligned} \tag{B.17}$$

To perform the trace calculation an identity for the trace of six γ matrices can be found from the properties of the trace, the fact that the γ matrices anticommute and the already stated identity for four γ matrices [30]. The identity becomes

$$\begin{aligned} Tr[\gamma^\kappa\gamma^\lambda\gamma^\mu\gamma^\nu\gamma^\rho\gamma^\sigma] =& \eta^{\kappa\lambda}Tr[\gamma^\mu\gamma^\nu\gamma^\rho\gamma^\sigma] - \eta^{\kappa\mu}Tr[\gamma^\lambda\gamma^\nu\gamma^\rho\gamma^\sigma] + \eta^{\kappa\nu}Tr[\gamma^\lambda\gamma^\mu\gamma^\rho\gamma^\sigma] - \\ &- \eta^{\kappa\rho}Tr[\gamma^\lambda\gamma^\mu\gamma^\nu\gamma^\sigma] + \eta^{\kappa\sigma}Tr[\gamma^\lambda\gamma^\mu\gamma^\nu\gamma^\rho]. \end{aligned} \tag{B.18}$$

The trace calculation combined with again utilising that $d^\mu q_\mu = 0$ one arrives at

$$\begin{aligned} \overline{|\mathcal{M}|^2} =& \frac{4g_{DM}^2 g_D^2}{(q^2 - m_{A'}^2)^2 + m_{A'}^2\Gamma_{A'}^2}\Big[-2d^2(k_1\cdot q)(k_2\cdot q) + d^2q^2(k_1\cdot k_2) - \\ &- 2q^2(d\cdot k_1)(d\cdot k_2) - m_e^2 d^2 q^2\Big]. \end{aligned} \tag{B.19}$$

Going to the CM-frame this becomes

$$\overline{|\mathcal{M}|^2_{CM}} = \frac{64g_{DM}^2 g_D^2}{(q^2 - m_{A'}^2)^2 + m_{A'}^2\Gamma_{A'}^2} E^2|\vec{p}|^2[E^2 - |\vec{k}|^2 + 2|\vec{k}|^2 cos^2\theta + m_e^2]. \tag{B.20}$$

B.3 Electric Dipole Moment

The derivation for the electric dipole moment is very similar, but here the vertex between electrons and DP as $-ig_D\sigma^{\mu\nu}\gamma^5 q_\nu$ and one has to utilise the fact that $\{\gamma^5,\gamma^\mu\}=0$ and $(\gamma^5)^\dagger=\gamma^5$. Doing this yields

$$\begin{aligned} i\mathcal{M} &= \frac{ig_{DM}g_D}{q^2-m_{A'}^2+im_{A'}\Gamma_{A'}}d^\mu\eta_{\mu\nu}q_\rho\left[\bar{u}^{s_1}(k_1)\sigma^{\nu\rho}\gamma^5 v^{s_2}(k_2)\right] \\ (i\mathcal{M})^* &= \frac{ig_{DM}g_D}{q^2-m_{A'}^2-im_{A'}\Gamma_{A'}}d^\mu\eta_{\mu\nu}q_\rho\left[\bar{v}^{s_2}(k_1)\gamma^5\sigma^{\nu\rho}u^{s_1}(k_2)\right]. \end{aligned} \tag{B.21}$$

This then gives

$$\begin{aligned} \overline{|\mathcal{M}|^2} =& -\underbrace{\frac{g_{DM}^2g_D^2}{(q^2-m_{A'}^2)^2+m_{A'}^2\Gamma_{A'}^2}}_{=D}d_\mu q_\nu d_\rho q_\sigma\sum_{s_1,s_2=1}^{2}\left[\bar{u}^{s_1}(k_1)\sigma^{\mu\nu}\gamma^5 v^{s_2}(k_2)\right]\times \\ &\times\left[\bar{v}^{s_2}(k_2)\gamma^5\sigma^{\rho\sigma}u^{s_1}(k_1)\right]= \\ =& -Dd_\mu q_\nu d_\rho q_\sigma Tr[(\not{k}_1+m_e)\sigma^{\mu\nu}\gamma^5(\not{k}_2-m_e)\gamma^5\sigma^{\rho\sigma}]= \\ =&\frac{4g_{DM}^2g_D^2}{(q^2-m_{A'}^2)^2+m_{A'}^2\Gamma_{A'}^2}[d^2q^2(k_1\cdot k_2)-2d^2(k_1\cdot k_q)(k_2\cdot q)- \\ &-2q^2(d\cdot k_1)(d\cdot k_2)+m_e^2d^2q^2] \end{aligned} \tag{B.22}$$

In the CM-frame this becomes

$$\overline{|\mathcal{M}|^2_{CM}} = \frac{128g_{DM}^2g_D^2}{(q^2-m_{A'}^2)^2+m_{A'}^2\Gamma_{A'}^2}E^2|\vec{p}|^2|\vec{k}|^2\cos^2\theta \tag{B.23}$$

B.4 Charge Moment

Once again the same calculation but for the Feynman rule of the charge interaction.

$$\begin{aligned} i\mathcal{M} &= [-ig_{DM}d^\mu]\left[\frac{-i}{q^2-m_{A'}^2+im_{A'}\Gamma_{A'}}\left(\eta_{\mu\nu}-\frac{q_\mu q_\nu}{m_{A'}^2}\right)\right]\times \\ &\times\left[\bar{u}^{s_1}(k_1)(ig'_D(q^2\gamma^\nu-q^\nu\not{q}))v^{s_2}(k_2)\right]= \\ &=\{d^\mu q_\mu=0\}= \\ &=\frac{-ig_{DM}g'_D}{q^2-m_{A'}^2+im_{A'}\Gamma_{A'}}d_\nu\left[\bar{u}^{s_1}(k_1)(q^2\gamma^\nu-q^\nu\not{q})v^{s_2}(k_2)\right]= \\ &=\{d_\nu q^\nu=0\}= \\ &=\frac{-ig_{DM}g'_D}{q^2-m_{A'}^2+im_{A'}\Gamma_{A'}}d_\nu q^2\left[\bar{u}^{s_1}(k_1)\gamma^\nu v^{s_2}(k_2)\right] \end{aligned} \tag{B.24}$$

$$(i\mathcal{M})^* = \frac{ig_{DM}g'_D}{q^2-m_{A'}^2-im_{A'}\Gamma_{A'}}d_\nu q^2\left[\bar{v}^{s_2}(k_2)\gamma^\nu u^{s_1}(k_1)\right]$$

$$\begin{aligned}\overline{|\mathcal{M}|^2} =& \underbrace{\frac{g_{DM}^2 g_D'^2}{(q^2-m_{A'}^2)^2+m_{A'}^2\Gamma_{A'}^2}}_{=D} d_\mu q^2 d_\nu q^2 \sum_{s_1,s_2=1}^{2} [\bar{u}^{s_1}(k_1)\gamma^\mu v^{s_2}(k_2)]\,[\bar{v}^{s_2}(k_2)\gamma^\nu u^{s_1}(k_1)] = \\ =& - D d_\mu q^2 d_\nu q^2 Tr[(\not{k}_1+m_e)\gamma^\mu(\not{k}_2-m_e)\gamma^\nu] = \\ =& \frac{4 g_{DM}^2 g_D'^2}{(q^2-m_{A'}^2)^2+m_{A'}^2\Gamma_{A'}^2} q^4 [2(d\cdot k_1)(d\cdot k_2) - d^2(k_1\cdot k_2) - m_e^2 d^2]\end{aligned} \tag{B.25}$$

$$\overline{|\mathcal{M}|^2_{CM}} = \frac{512 g_{DM}^2 g_D'^2}{(q^2-m_{A'}^2)^2+m_{A'}^2\Gamma_{A'}^2} E^4 |\vec{p}|^2 [E^2 - |\vec{k}|^2 \cos^2\theta] \tag{B.26}$$

B.5 Anapole Moment

Finally the anapole interaction.

$$\begin{aligned} i\mathcal{M} =& [-i g_{DM} d^\mu]\left[\frac{-i}{q^2-m_{A'}^2+i m_{A'}\Gamma_{A'}}\left(\eta_{\mu\nu}-\frac{q_\mu q_\nu}{m_{A'}^2}\right)\right]\times \\ & \times\left[\bar{u}^{s_1}(k_1)(-i g_D'(q^2\gamma^\nu - q^\nu \not{q})\gamma^5) v^{s_2}(k_2)\right] = \\ =& \frac{i g_{DM} g_D'}{q^2-m_{A'}^2+i m_{A'}\Gamma_{A'}} d_\nu q^2 \left[\bar{u}^{s_1}(k_1)\gamma^\nu\gamma^5 v^{s_2}(k_2)\right] \end{aligned} \tag{B.27}$$

$$(i\mathcal{M})^* = \frac{i g_{DM} g_D'}{q^2-m_{A'}^2-i m_{A'}\Gamma_{A'}} d_\nu q^2 \left[\bar{v}^{s_2}(k_2)\gamma^5\gamma^\nu u^{s_1}(k_1)\right]$$

$$\begin{aligned}\overline{|\mathcal{M}|^2} =& -\underbrace{\frac{g_{DM}^2 g_D'^2}{(q^2-m_{A'}^2)^2+m_{A'}^2\Gamma_{A'}^2}}_{=D} d_\mu q^2 d_\nu q^2 \sum_{s_1,s_2=1}^{2}\left[\bar{u}^{s_1}(k_1)\gamma^\mu\gamma^5 v^{s_2}(k_2)\right]\times \\ & \times\left[\bar{v}^{s_2}(k_2)\gamma^5\gamma^\nu u^{s_1}(k_1)\right] = \\ =& - D d_\mu q^2 d_\nu q^2 Tr[(\not{k}_1+m_e)\gamma^\mu\gamma^5(\not{k}_2-m_e)\gamma^5\gamma^\nu] = \\ =& \frac{4 g_{DM}^2 g_D'^2}{(q^2-m_{A'}^2)^2+m_{A'}^2\Gamma_{A'}^2} q^4 [2(d\cdot k_1)(d\cdot k_2) - d^2(k_1\cdot k_2) + m_e^2 d^2]\end{aligned} \tag{B.28}$$

$$\overline{|\mathcal{M}|^2_{CM}} = \frac{512 g_{DM}^2 g_D'^2}{(q^2-m_{A'}^2)^2+m_{A'}^2\Gamma_{A'}^2} E^4 |\vec{p}|^2 [|\vec{k}|^2 - |\vec{k}|^2 \cos^2\theta] \tag{B.29}$$

C

Matrix Elements for the Decay of the Dark Photon

Below follow the derivation of the matrix elements that contribute to the decay rate of the DP, A', with four-momentum q presented in 2.10. In the calculations the decay is to two particles with momentum p_1 and p_2, and the calculations are made in the rest frame of the DP. To be able to make the calculation one has to consider how to handle the sum over the polarisation vectors which becomes [31]

$$\sum_{\lambda} \epsilon_\mu(\vec{q},\lambda)\epsilon^*_\nu(\vec{q},\lambda) = -\eta_{\mu\nu} + \frac{q_\mu q_\nu}{m^2_{A'}}. \tag{C.1}$$

In the above sum λ runs over the polarisation states ± 1 and 0.

C.1 $A' \to \chi + \chi^*$

The Feynman rules give for the decay process

$$i\mathcal{M}_{A'\to\chi+\chi^*} = -ig_{DM}\epsilon_\mu(\vec{q},\lambda)(p_1^\mu - p_2^\mu) \tag{C.2}$$

Taking the modulus squared and averaging over the initial polarisation states and summing over final state spins gives

$$\begin{aligned}
\overline{\mathcal{M}}_{A'\to\chi+\chi^*} &= \frac{g^2_{DM}}{3}\sum_{\lambda}\epsilon_\mu(\vec{q},\lambda)\epsilon^*_\nu(\vec{q},\lambda)(p_1-p_2)^\mu(p_1-p_2)^\nu = \\
&= -\frac{g^2_{DM}}{3}\left(\eta_{\mu\nu} + \frac{q_\mu q_\nu}{m^2_{A'}}\right)(p_1-p_2)^\mu(p_1-p_2)^\nu = \\
&= \{q_\mu(p_1-p_2)^\mu = (p_1+p_2)_\mu(p_1-p_2)^\mu = 0\} = \\
&= -\frac{g^2_{DM}}{3}(p_1-p_2)^2.
\end{aligned} \tag{C.3}$$

Considering that it is in the rest frame of the A' this means that

$$\begin{aligned}
q^2 =& m^2_{A'} = (p_1+p_2)^2 = 2m^2_\chi + 2p_1\cdot p_2 \\
\implies & p_1\cdot p_2 = \frac{m^2_{A'}}{2} - m^2_\chi \\
\implies & (p_1-p_2)^2 = p_1^2 - 2p_1\cdot p_2 + p_2^2 = 4m^2_\chi - m^2_{A'}.
\end{aligned} \tag{C.4}$$

This yields the final matrix element squared

$$\overline{\mathcal{M}}_{A'\to\chi+\chi^*} = \frac{g_{DM}^2}{3}(m_{A'}^2 - 4m_\chi^2). \tag{C.5}$$

C.2 $A' \to e^- + e^+$

For the case of DP decay to electrons one does the same as for $\chi + \chi^*$, but using the Feynman rules for the vertex for each specific interaction between the electron and the DP. Also utilising the same tools for spin sums and traces as described in appendix B yields this matrix element squared averaged over the initial state polarisations and summed over the final state ones as stated in section 2.3. These calculations have been performed by hand for the KM and magnetic dipole case and the rest with FeynRules [23] since there was agreement between the by hand and the FeynRules ones. All have been crosschecked with FeynRules.

DEPARTMENT OF PHYSICS
CHALMERS UNIVERSITY OF TECHNOLOGY
Gothenburg, Sweden
www.chalmers.se

CHALMERS
UNIVERSITY OF TECHNOLOGY